Cancer Cell

Article

Whole-genome doubling drives immune evasion by silencing antigen presentation

Graphical abstract

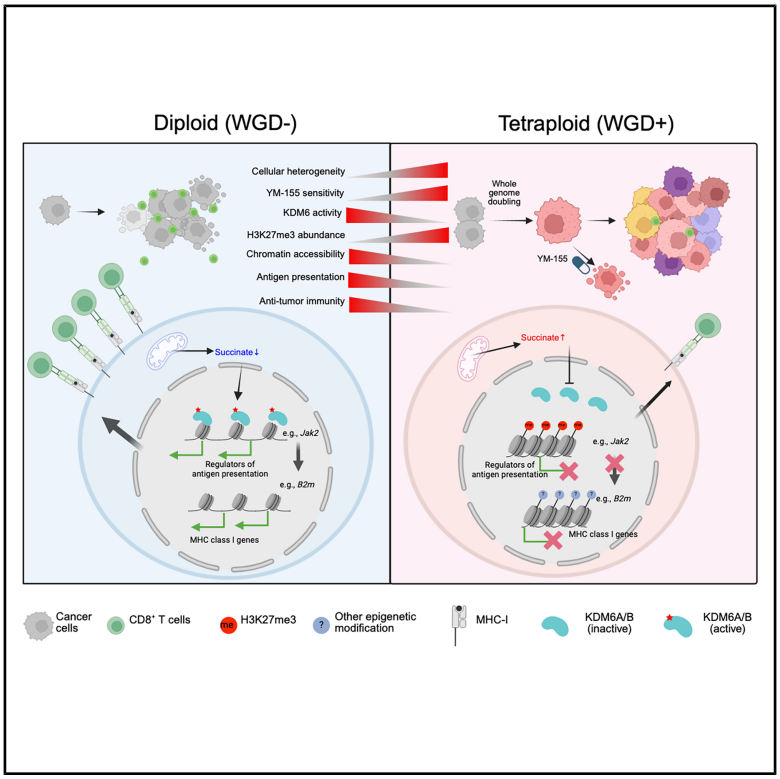

Highlights

- Whole-genome doubling (WGD) is a driver of immune escape in breast cancer
- Different mechanisms triggering WGD may lead to distinct tumor evolutionary paths
- WGD+ cancer cells have reduced antigen presentation and response to IFNγ stimuli
- WGD+ tumors have lower KDM6 activity causing higher H3K27me3 muting MHC regulators

Authors

Pierre Foidart, Zheqi Li, Xinran Cai, ..., Henry W. Long, Judith Agudo, Kornelia Polyak

Correspondence

kornelia_polyak@dfci.harvard.edu

In brief

Foidart et al. reveal that whole-genome doubling (WGD) promotes immune suppression in breast cancer. WGD+ tumors have diminished expression of antigen presentation and reduced IFNγ response. Metabolic alterations in WGD+ tumors lead to lower KDM6 activity, causing higher H3K27me3 that represses transcriptional regulators of antigen presentation genes.

Foidart et al., 2026, Cancer Cell *44*, 1–19
July 13, 2026
https://doi.org/10.1016/j.ccell.2026.04.007

CellPress

Cancer Cell

CellPress
OPEN ACCESS

Article

Whole-genome doubling drives immune evasion by silencing antigen presentation

Pierre Foidart,[1,2,3,14] Zheqi Li,[1,2,3,14] Xinran Cai,[1,2,3,14] Marco Seehawer,[1,2,3] Daniel D. Brown,[4] Amatullah Tawawalla,[1] Pilar Baldominos,[5,6] Salma Parvin,[1,2,3] Jun Nishida,[1,2,3] Ernesto Rojas-Jimenez,[1,2,3] Triet M. Bui,[1,2,3] Benedetto Diciaccio,[1,2,3] Rahul Kumar,[7,8] Brent T. Schlegel,[7,8] Marie-Anne Goyette,[1,2,3] TashJae Scales,[9] Pengze Yan,[1,2,3] Xintao Qiu,[9] Rong Li,[9] Yijia Jiang,[9] Yingtian Xie,[9] Mahmoud Aarabi,[10,11] Xiao-Yun Huang,[1] Laura E. Stevens,[1,2,3] Paloma Cejas,[9] Lise Mangiante,[12] Cristina Irene Sotomayor Vivas,[12] Kathleen E. Houlahan,[12] Christina Curtis,[12] Steffi Oesterreich,[7,8] Isaac S. Harris,[13] Anthony G. Letai,[1,2,3] Adrian V. Lee,[4,7,8] Henry W. Long,[9] Judith Agudo,[5,6] and Kornelia Polyak[1,2,3,15,*]

[1]Department of Medical Oncology, Dana-Farber Cancer Institute, Boston, MA 02215, USA
[2]Department of Medicine, Brigham and Women's Hospital, Boston, MA 02115, USA
[3]Department of Medicine, Harvard Medical School, Boston, MA 02115, USA
[4]Institute for Precision Medicine, University of Pittsburgh, Pittsburgh, PA 15260, USA
[5]Department of Cancer Immunology and Virology, Dana-Farber Cancer Institute, Boston, MA 02215, USA
[6]Department of Immunology, Harvard Medical School, Boston, MA 02115, USA
[7]Women's Cancer Research Center, UPMC Hillman Cancer Center, Magee-Women's Research Institute, Pittsburgh, PA 15260, USA
[8]Department of Pharmacology and Chemical Biology, University of Pittsburgh, Pittsburgh, PA 15260, USA
[9]Center for Functional Cancer Epigenetics, Dana-Farber Cancer Institute, Boston, MA 02215, USA
[10]Departments of Pathology, and Obstetrics, Gynecology, and Reproductive Sciences, University of Pittsburgh School of Medicine, Pittsburgh, PA 15261, USA
[11]UPMC Cytogenetics Laboratoires, UPMC Magee-Womens Hospital, Pittsburgh, PA 15213, USA
[12]Stanford Cancer Institute, Stanford University School of Medicine, Stanford, CA 94305, USA
[13]University of Rochester Medical Center, Rochester, NY 14642, USA
[14]These authors contributed equally
[15]Lead contact
*Correspondence: kornelia_polyak@dfci.harvard.edu
https://doi.org/10.1016/j.ccell.2026.04.007

SUMMARY

Whole-genome doubling (WGD) is a common yet poorly understood event associated with poor clinical outcomes. Here, we characterize mechanisms by which WGD drives tumor evolution, utilizing mouse mammary tumor models of WGD established through cell fusion. We find that WGD increases transcriptomic and epigenetic heterogeneity and identify the YM155 BIRC5 inhibitor as a compound specifically suppressing WGD+ tumors. WGD triggers immune evasion by escaping $CD8^+$ T cell responses, rendering WGD+ tumors more sensitive to anti-PD-L1. Through single-cell profiling, we discover that WGD+ cancer cells exhibit reduced antigen presentation and response to IFNγ, attributed to the epigenetic silencing of MHCI transcriptional regulators via elevated histone H3 lysine 27 trimethylation. Further investigations reveal decreased KDM6 activity and increased succinate levels in WGD+ tumors. PRC2 inhibition preferentially suppresses WGD+ tumor growth, enhances antigen presentation, and $CD8^+$ T cell infiltration. Our results underscore metabolic and epigenetic alterations as critical drivers of WGD-associated immune escape.

INTRODUCTION

Whole-genome doubling (WGD) is a common initiating event in tumorigenesis leading to aneuploidy, already detected in pre-invasive and premalignant lesions.[1–3] Multiple mechanisms can lead to WGD, including mitotic perturbations, endoreduplication, and cell-to-cell fusion.[4] Polyploid cells display genomic instability, which increases intratumor heterogeneity and accelerates cancer genome evolution.[5] Chromosomal instability and the presence of tetraploid and hyperdiploid cancer cells are associated with treatment resistance,[6–8] yet the underlying mechanisms are poorly understood.

Breast cancer is classified based on the expression of estrogen receptor (ER), progesterone receptor (PR), and human epidermal growth factor receptor 2 (HER2) into hormone receptor positive (HR+), HER2+, and triple-negative breast cancer (TNBC). While the availability of targeted therapies for HR+ and HER2+ tumors improved clinical outcomes, treatment of TNBC

Please cite this article in press as: Foidart et al., Whole-genome doubling drives immune evasion by silencing antigen presentation, Cancer Cell (2026), https://doi.org/10.1016/j.ccell.2026.04.007

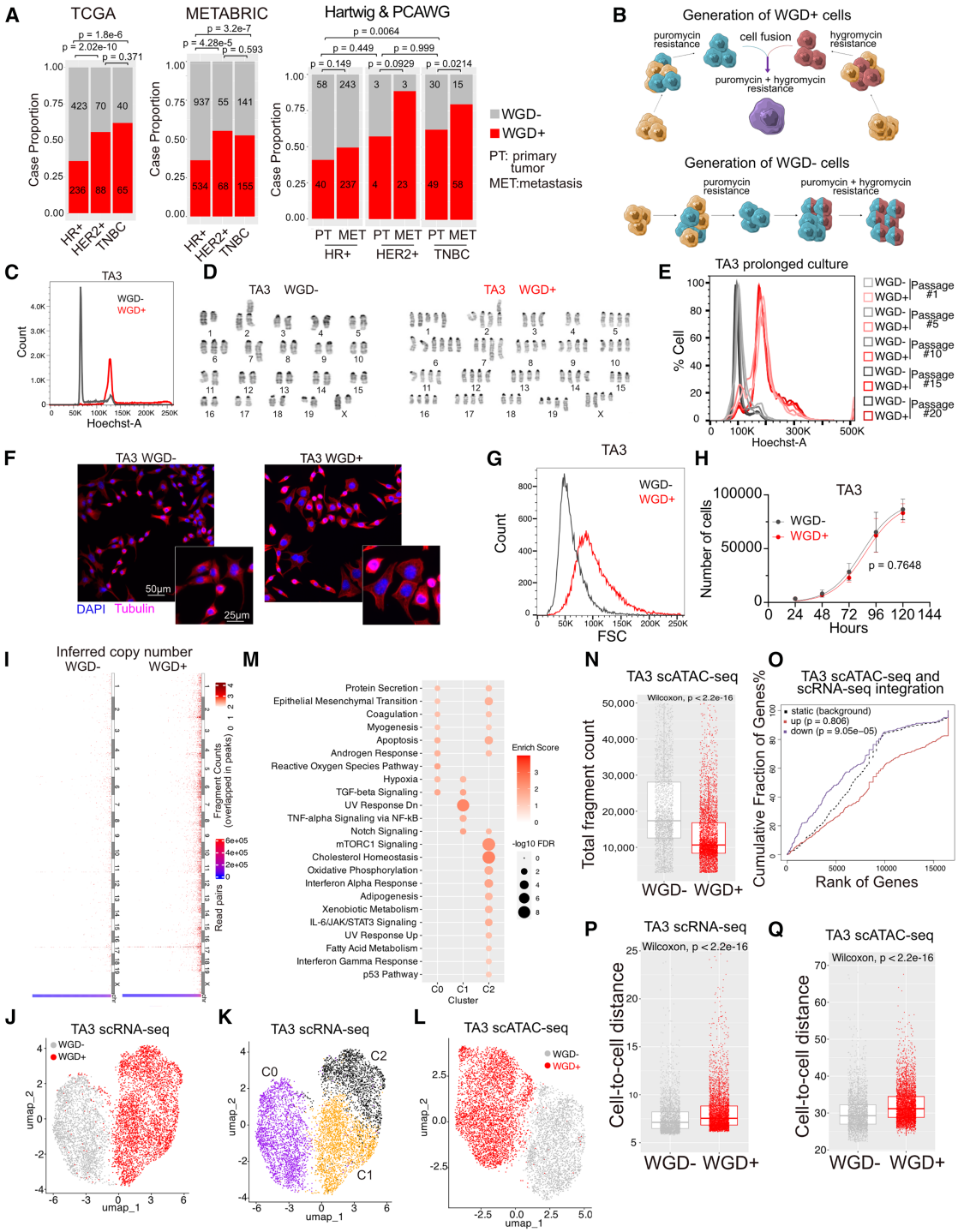

Figure 1. Clinical relevance of WGD and an experimental model of WGD

(A) Percentage of tumors identified as WGD- or WGD+. Fisher's exact test.

(B) Schematic of WGD- and WGD+ cell generation.

(C and D) Flow cytometry for DNA content (C) and karyotype (D) of TA3 model.

(E) Flow cytometry of Hoechst33258-stained TA3 fusion WGD- and WGD+ cells at different passages.

(F) Immunofluorescence for tubulin and DAPI. Scale bars are 50 µm and 25 µm.

(G) Flow cytometry for forward scatter of TA3 model.

(H) Viable cell numbers at the indicated time points. Data are represented as mean ± SD, *n* = 3 per group. Comparison of logistic growth curve. Error bars represent ±SD. Extra sum-of-squares F test.

(I) Heatmap of copy number estimation based on the scATAC-seq data of TA3 model.

(legend continued on next page)

Please cite this article in press as: Foidart et al., Whole-genome doubling drives immune evasion by silencing antigen presentation, Cancer Cell (2026), https://doi.org/10.1016/j.ccell.2026.04.007

remains limited.[9–11] We identified BET bromodomain inhibitors as candidate therapeutic agents in TNBC[12] in combination with paclitaxel, CDK4/6 inhibitors, and anti-PD-L1.[13,14] However, we observed rapid emergence of resistance, and that while all resistant cells were tetraploid, tetraploidy by itself did not confer resistance.[15]

Aneuploid cells in normal tissues elicit an immune response and are cleared by the immune system.[16–19] In cancer, however, aneuploidy is thought to cause immune evasion,[20,21] based on the correlation of aneuploidy with diminished immune infiltration in The Cancer Genome Atlas (TCGA).[20–22] Similarly, pan-cancer analysis of TCGA shows an inverse correlation between WGD and estimates of tumor-infiltrating leukocytes.[23] However, reports also suggest that tetraploidization and polyploidy lead to increased immunogenicity[24] and aneuploidy-associated senescence sensitizes to NK cell-mediated killing.[17,25] Thus, the mechanisms by which WGD promotes tumor evolution, including immune escape, remain poorly defined. To investigate this, we generated mouse mammary tumor cell line models of WGD and discovered a metabolic-epigenetic mechanism of WGD-associated immune evasion.

RESULTS

WGD in breast tumors and models of WGD

We investigated WGD in breast cancer by WGD calling[26,27] or reanalyzing public genome sequencing data with known WGD status.[22,28,29] WGD is more common in HER2+ tumors and TNBC than HR+ tumors and is further increased in distant metastases (Figure 1A and S1A). WGD is more enriched in *TP53*-mutant compared to wild-type (WT) primary breast cancers across all subtypes (Figure S1B), but was associated with worse prognosis in *TP53* WT cases (Figure S1C). Key fusogenic ligands *ERVW1* and *SLC1A5* had significantly higher expression in WGD+ tumors with WT but not mutant *TP53* (Figure S1D), implying cell fusion as a route of WGD.

To dissect how WGD drives breast tumor evolution, we generated experimental models of WGD using mouse mammary tumor cell lines by somatic cell fusion (Figure 1B). Cell fusion and ploidy were confirmed by flow cytometry for DNA content (Figures 1C and S1E). Karyotyping showed nearly perfect doubling of the genome in the WGD+ cells in TA3 and 168fARN models (Figures 1D and S1F; Table S1) and confirmed nearly diploid parental TA3 karyotype (Figure 1D; Table S1), hypotetraploidy, and high aneuploidy of 168fARN and 67NR lines (Figures S1E and S1F; Table S1). The high baseline ploidy of 67NR cells may explain the limited shift in DNA content in the fusions, as a significant increase is likely not tolerated. Therefore, we primarily used the TA3 model, as it best reflects the euploid (2n, WGD-) and tetraploid (4n, WGD+) states. We confirmed the stability of WGD- and WGD+ by flow cytometry for DNA content during prolonged culture of the TA3 model (Figure 1E). Exome sequencing of parental TA3, 168fARN, and 67NR cells and their WGD+ derivatives revealed that most variants in WGD-cells were shared with their matched WGD+ counterparts (Figures S1G and S1H; Table S1). The limited number of unique variants in WGD- cells suggests that WGD+ derivatives are not likely to be a minor subclone of the WGD-population. All three cell lines are *TP53* WT, and functional p53 was confirmed in TA3 and 168FARN WGD- and WGD+ derivatives based on the robust induction of p21 by doxorubicin (Figure S1I). WGD+ TA3 and 168fARN cells were larger than their corresponding WGD- counterparts and had a single nucleus (Figures 1F, 1G, and S1J). The proliferation of WGD- and WGD+ cells was not significantly different in cell culture (Figures 1H and S1K).

To investigate the effect of WGD on cellular heterogeneity, we performed a duplexed single-cell RNA sequencing (scRNA-seq) and a single-cell assay for transposase-accessible chromatin (scATAC-seq) on the TA3 and 67NR WGD- and WGD+ lines. The estimation of chromosomal copy number based on overlapped fragment counts in ATAC peaks in the TA3 model confirmed the diploid and tetraploid state of each cell within WGD- and WGD+ cells populations, respectively (Figure 1I), while the 67NR copy number prediction was less confident, likely due to high heterogeneity and pre-existing aneuploidy (Figure S2A).

Uniform manifold approximation and projection (UMAP) indicated transcriptional and epigenetic differences between WGD- and WGD+ cells (Figures 1J-1L and S2B-S2C). Hallmark signature enrichment analysis of scRNA-seq clusters identified different activated pathways in WGD+ compared to WGD-cells, including inflammatory response and metabolism (Figures 1M and S2D; Table S2). Fragment count in scATAC-seq data was significantly lower in WGD+ cells, suggesting more compact inactive chromatin is less accessible to transposase (Figures 1N and S2E; Table S2).

Genomic distribution of the differential ATAC peaks showed that most peaks lost in WGD+ cells were in promoters, while gained peaks were more common in distant intergenic regions and introns (Figure S2F), implying that WGD might lead to transcriptional repression. Integration of scATAC-seq and scRNA-seq data demonstrated a significant positive correlation between mRNA and ATAC-based inferred gene activity in both models (Figure S2G). Binding and expression target analysis (BETA) of differential ATAC peaks showed that genes annotated to lost peaks in WGD+ cells were downregulated in both models, while WGD+ gained peaks' association with upregulated genes was only significant in 67NR cells (Figures 1O and S2H). Accordingly, the majority of lost ATAC peaks were common between the

(J and K) UMAP of scRNA-seq of TA3 model colored by genotype (J) and cell clusters (K).
(L) UMAP of scATAC-seq of TA3 model colored by genotype.
(M) Enrichment of hallmark pathways in marker genes of three subclusters in K.
(N) DNA fragment counts in the scATAC-seq data.
(O) BETA association of TA3 WGD+ lost ATAC peaks to DEGs. One-sided Kolmogorov-Smirnov test.
(P) Transcriptomic cell-to-cell Euclidean distance from PCA dimension reduction.
(Q) Epigenetic cell-to-cell Euclidean distance from ISI dimension reduction. Boxplots (N, P, and Q) represent the median (center line) and interquartile range (box, 25th-75th percentiles). Whiskers extend to 1.5× the interquartile range. Mann-Whitney U test (N, P, Q). See also Figures S1 and S2, Tables S1 and S2.

Please cite this article in press as: Foidart et al., Whole-genome doubling drives immune evasion by silencing antigen presentation, Cancer Cell (2026), https://doi.org/10.1016/j.ccell.2026.04.007

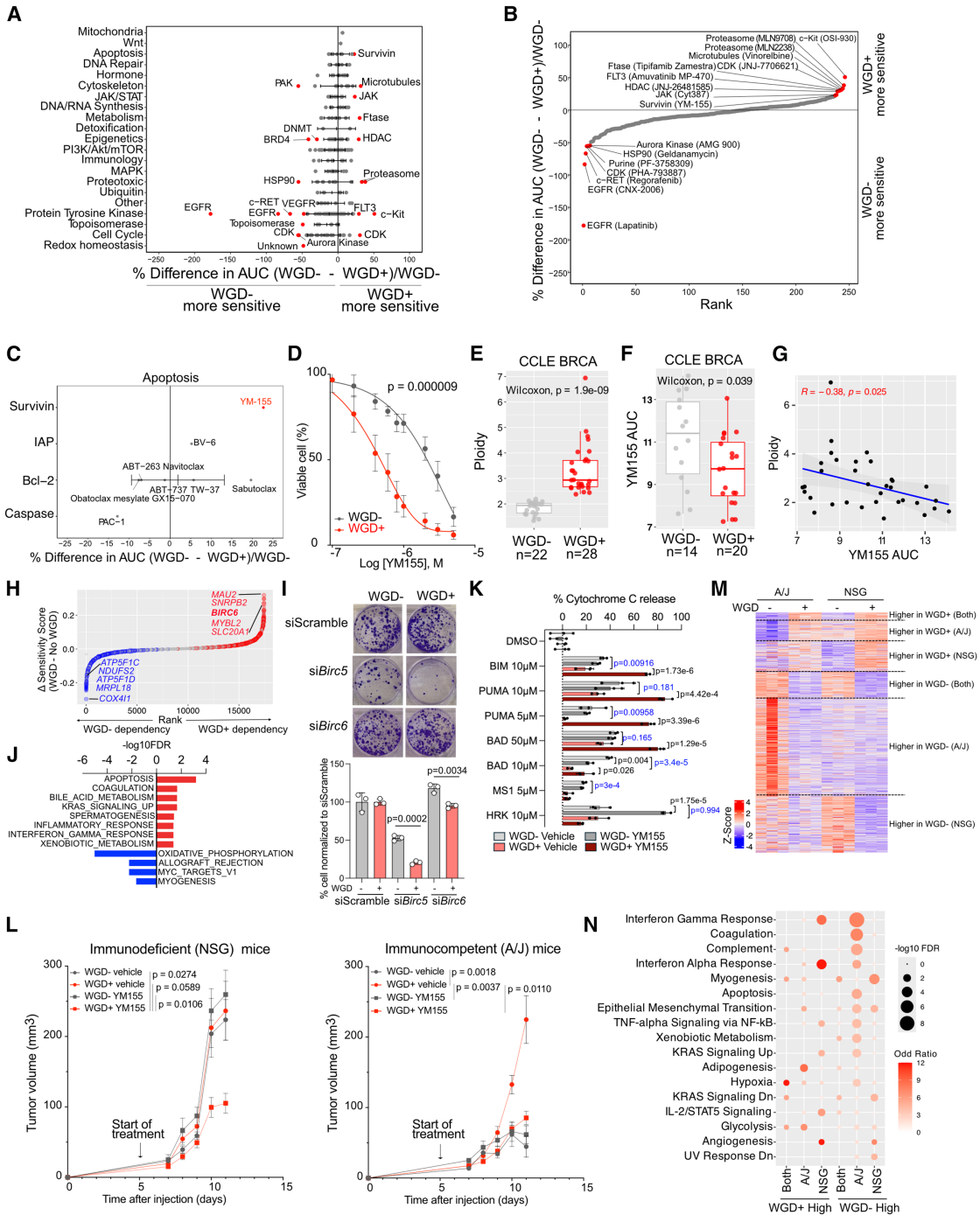

Figure 2. Small molecule screen and follow-up validation

(A and B) Differences in drug sensitivities between WGD- and WGD+ cells by pathways (A) and ordered by percent differences in AUC for target (B).

(C) Differences in sensitivities of apoptosis-targeting agents, grouped by target.

(D) Dose-response curves of YM155 in WGD- and WGD+ cells (n = 3 per group). Extra sum-of-squares F test.

(E) Estimated ploidy of breast cancer cell lines from CCLE.

(F) DepMap PRISM screen YM155 AUC in WGD- and WGD+ breast cancer cell lines.

(G) Scatterplot shows Pearson's correlation between ploidy and YM155 AUC.

(H) CRISPR screen hits ranked by differences in sensitivity scores between WGD- and WGD+ TNBC lines. Significantly different hits (FDR<0.05) are labeled in red and blue. Top 10 hits are indicated.

(I) Representative images of colony formation assay of TA3 WGD- and WGD+ cells expressing *Birc5* or *Birc6* siRNAs (Top). Quantification of colony growth (bottom), n = 3/condition. One-way ANOVA.

(legend continued on next page)

Please cite this article in press as: Foidart et al., Whole-genome doubling drives immune evasion by silencing antigen presentation, Cancer Cell (2026), https://doi.org/10.1016/j.ccell.2026.04.007

two models; gained peaks and differentially expressed genes (DEGs) showed limited overlap (Figure S2I). Genes commonly upregulated in WGD+ cells were enriched in apoptosis and interferon signaling pathways, while downregulated genes were MYC targets (Figure S2J). Consistently, LISA prediction of transcriptional regulators of DEGs identified MYC, STAT5, and RELA (Figure S2K; Table S2). Calculating cell-to-cell distance as a measure of heterogeneity revealed significantly higher heterogeneity at both transcriptomic and chromatin levels among the WGD+ cells in both TA3 and 67NR models (Figures 1P, 1Q, S2L, and S2M).

Small molecule inhibitor screen for WGD-targeting compounds

To assess the impact of WGD on therapeutic sensitivity, we performed a small molecule inhibitor (SMI) screen testing ~400 compounds using the TA3 model (Table S3). Sensitivity of WGD- and WGD+ cells was comparable to most compounds, with a few exceptions. WGD+ cells were more resistant to several kinase inhibitors (e.g., AURKA and CHK1) but displayed augmented sensitivity to YM155 (Figures 2A–2C and S3A). Follow-up validation of selected hits revealed the most significant and reproducible differences in response to YM155 (Figures 2D and S3B). We confirmed the heightened sensitivity of WGD+ breast cancer lines to YM155 using the PRISM database[30] and inferred WGD status from the Cancer Cell Line Encyclopedia (CCLE)[31] (Figures 2E–2G). YM155 represses a series of the inhibitor of apoptosis (IAP) family proteins, with BIRC5 (survivin) being its major target.[32] Immunoblot analysis showed lower BIRC5 in WGD+ compared to WGD-cells in the TA3 model (Figures S3C and S3D). *BIRC5* transcript levels were also lower in WGD+ tumors in the TCGA TNBC cohort, but not in three other cohorts and the CCLE breast cancer lines (Figure S3E). Reanalysis of the DepMap 22Q4 CRISPR screen data identified *BIRC6* as a top hit in WGD+ lines (Figure 2H; Table S3). We performed colony formation assays following the downregulation of *Birc5* or *Birc6* and observed more pronounced growth inhibition after *Birc5* knockdown in TA3 WGD+ than in WGD cells, while *Birc6* downregulation did not impair cell growth (Figures 2I and S3F). Accordingly, apoptosis was the top-enriched pathway in WGD+ cell line-specific CRISPR screen hits (Figure 2J). BH3 profiling[33] of TA3 WGD-/+ cells in the presence and absence of YM155 revealed that WGD+ cells were more primed to apoptosis following YM155 treatment, but baseline sensitivity was not significantly different (Figure 2K).

To test sensitivity to YM155 *in vivo,* we injected cells into immunocompetent (A/J) or immunodeficient (NSG) mice. YM155 inhibited the growth of WGD+ but not WGD-tumors in both A/J and NSG mice (Figure 2L). Gene expression profiling revealed the repression of metabolic pathways, including cholesterol and insulin biosynthesis, by YM155 in WGD+ tumors in both strains (Figures 2M and S3G). We also discovered that WGD+ tumors grew much faster than WGD- ones in immunocompetent but not in immunodeficient mice (Figure 2L). WGD- and WGD+ tumor RNA-seq profiles were more distinct in A/J than in NSG mice (Figure S3H). Pathway analysis of tumor transcriptomes revealed significant differences in immune-related pathways depending on mouse strain (Figure 2N; Table S3). Interferon signaling was enriched in WGD- high genes in A/J mice and in WGD+ tumors in NSG mice.

Immune environments of WGD- and WGD+ tumors

We repeated the *in vivo* experiment using A/J and NSG mice without treatment, which again showed faster growth of WGD+ tumors in A/J but not in NSG mice (Figures 3A and S4A). Microscopic examination of tumors identified high levels of necrosis in WGD- tumors in A/J mice, while no differences were noted in NSG mice (Figures S4B and S4C). Flow cytometry for lymphoid and myeloid markers revealed that WGD+ tumors had significantly fewer $CD45^+$ leukocytes and a pronounced decrease in $CD3^+$ and $CD8^+$ T cells compared to WGD- tumors, with a decreased $CD8^+$ T cell/Treg ratio (Figures 3B, S4D–S4F, and S5A). Relative frequencies of NK cells, macrophages, and dendritic cells were also lower in WGD+ tumors, while neutrophils showed the opposite pattern (Figure S5B). Immunofluorescence confirmed significantly fewer $CD3^+$ and $CD8^+$ T cells in WGD+ tumors (Figure 3C).

Repeat of these experiments in the 168fARN model showed similarly faster growth of WGD+ tumors (Figure S5C). Flow cytometry demonstrated reduced infiltration of $CD3^+$ and $CD8^+$ T cells in WGD+ tumors (Figure S5D). To investigate whether different ways of achieving WGD might affect this phenotype, we derived TA3 WGD+ cells by inducing cytokinesis failure (CF) with cytochalasin D (Figures S5E–S5H). Tumor growth assays in A/J mice showed much faster growth and greater heterogeneity compared to the TA3 fusion model and no significant difference between CF WGD- and WGD+ tumors (Figure S5I). Flow cytometry for DNA content revealed a shift to 2n ploidy in a few WGD+ tumors, implying less stable genotypes (Figure S5J). Total leukocyte content was significantly lower in CF WGD+ tumors, and while there were no differences in total $CD3^+$ and $CD8^+$ T cells, the $CD8^+$ T cell/Treg ratio was significantly lower in WGD+ tumors due to high Treg content (Figure S5K).

To explore if differences in immune infiltration are due to differences in the chemokines involved in leukocyte recruitment, we performed cytokine array analysis of TA3 tumor lysates from NSG and A/J mice. WGD+ tumors had lower levels of the CXCL9 and CXCL10 IFNγ-inducible chemokines that recruit

(J) Significantly enriched Hallmark pathways in WGD- and WGD+ sensitive hits in H.
(K) Percentage of cytochrome *c* release under the indicated treatments in WGD- and WGD+ TA3 cells -/+ YM155. One-way ANOVA was used among the four groups with technical triplicates.
(L) Volume of TA3 WGD- and WGD+ tumors in NSG and A/J mice by vehicle or YM155. n = 6–10/condition. *p*-values calculated with Two-Way ANOVA-Tukey's multiple comparisons test.
(M) Heatmap depicts the union of DEGs between WGD- and WGD+ tumors in NSG and A/J mice.
(N) Hallmark pathways were significantly enriched in at least one indicated DEG set. Boxplots (E, F) represent the median (center line) and interquartile range (box, 25th-75th percentiles). Whiskers extend to 1.5× the interquartile range. Error bars represent ±SEM (D, L) and ±SD (I, K). Mann-Whitney U test. (E, F) See also Figure S3; Table S3.

Please cite this article in press as: Foidart et al., Whole-genome doubling drives immune evasion by silencing antigen presentation, Cancer Cell (2026), https://doi.org/10.1016/j.ccell.2026.04.007

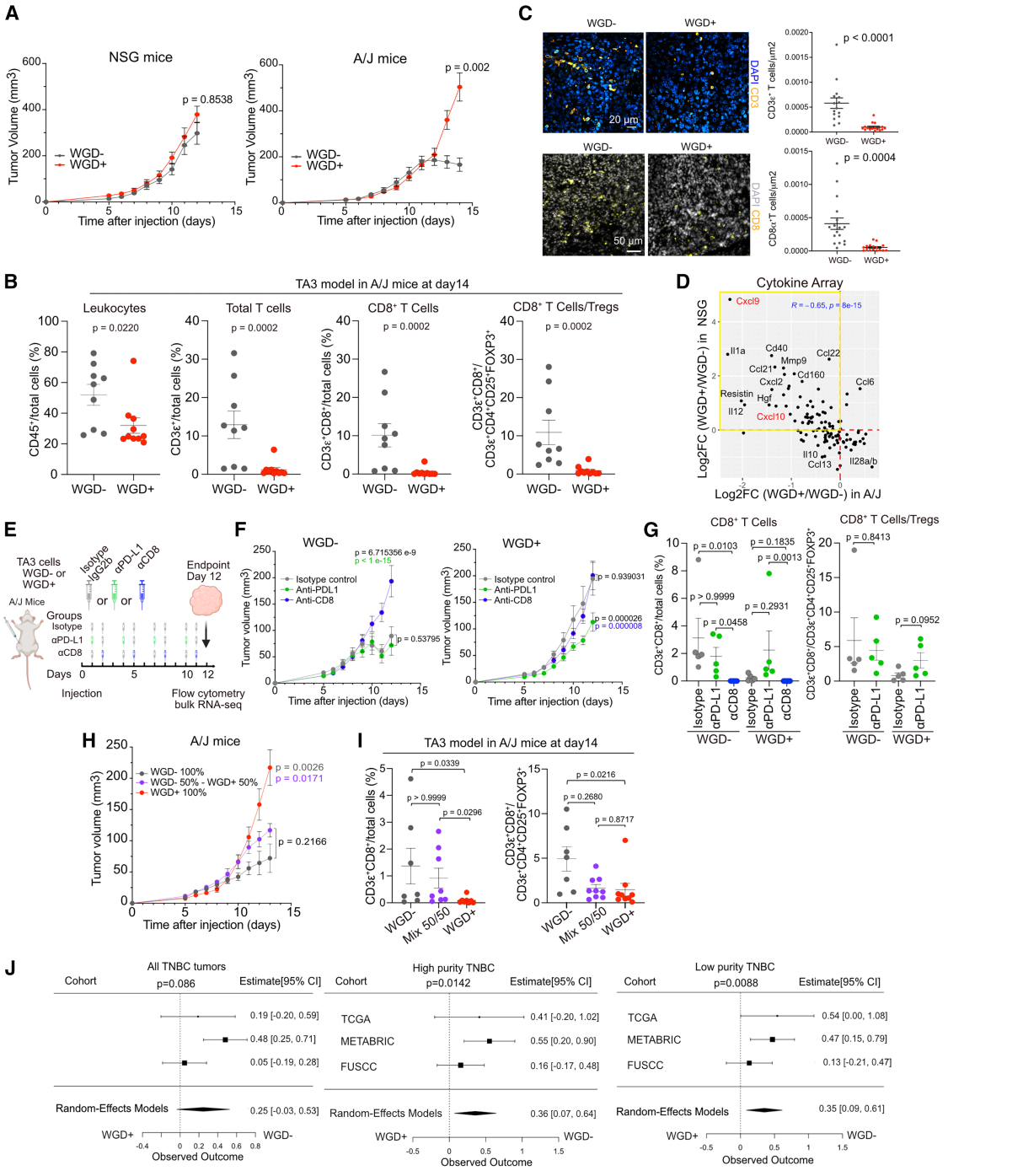

Figure 3. Growth of WGD- and WGD+ cells in immunodeficient and immunocompetent mice

(A) Growth of TA3 WGD- or WGD+ tumors in immunodeficient NSG and in immunocompetent A/J mice (n = 10/condition). two-Way ANOVA - Šídák's multiple comparisons test.

(B) Quantification of immune populations by flow cytometry (n = 9–10/condition).

(C) Representative immunofluorescence for CD3 and CD8 in tumors from A/J mice and quantification of immune cell density (n = 9–10/condition). Scale bars are 20 µm or 50 µm.

(D) Pearson's correlation of the difference in cytokine levels between WGD- and WGD+ tumors in NSG and A/J mice. Cytokines lower in WGD+ in A/J but higher in WGD+ in NSG are highlighted.

(E) Schematic of CD8$^+$ T cell depletion and anti-PD-L1 treatment.

(F) Tumor volumes in A/J mice treated with the indicated antibodies starting on day five after tumor cell injection (n = 15–16/condition). p-value color: comparison to vehicle (black), anti-CD8 (blue), and anti-PD-L1 (green).

(legend continued on next page)

Please cite this article in press as: Foidart et al., Whole-genome doubling drives immune evasion by silencing antigen presentation, Cancer Cell (2026), https://doi.org/10.1016/j.ccell.2026.04.007

$CD8^+$ T cells[34] in A/J but not in NSG mice (Figure 3D). To test the role of $CD8^+$ T cells in tumor growth, we repeated the experiment with the TA3 model and treated the mice with anti-CD8 or anti-PD-L1 antibodies or isotype controls (Figure 3E). The depletion of $CD8^+$ T cells significantly accelerated WGD-tumor growth but did not affect WGD+ tumors (Figures 3F and S6A). In contrast, anti-PD-L1 decreased WGD+ tumor growth but had minimal effect on WGD-ones (Figure 3F). Flow cytometry confirmed $CD8^+$ T cell depletion by anti-CD8 and demonstrated an increasing trend in $CD8^+$ T cells in WGD+ tumors from anti-PD-L1-treated mice (Figures 3G and S6B). Anti-CD8 depletion in the 168fARN model gave the same results (Figures S6C and S6D).

Next, we analyzed gene expression profiles of TA3 tumors from each treatment group by bulk RNA-seq. Clustering of samples based on mRNA levels of DEGs or GSVA enrichment scores showed pronounced differences at baseline, and CD8 depletion reshaped WGD- tumors to a WGD+-like immune-cold status (highlighted different shifts of imm Figures S6E and S6F). The correlation of the Hallmark signature enrichment score alterations induced by anti-CD8 or anti-PD-L1 highlighted different shifts in immune-related pathways: Anti-CD8 uniquely repressed immune pathways in WGD-tumors (Figure S6G) whereas anti-PDL1 exclusively activated them in WGD+ tumors (Figure S6H). Similarly, immune scores calculated from RNA-seq data showed a decreasing trend after anti-CD8 in WGD-tumors to levels comparable to WGD+ tumors at baseline (Figure S6I).

Human WGD+ cancers are not made of 100% tetraploid tumor cells, especially not when WGD occurs. To mimic this clinical scenario, we derived tumors from 1:1 mixture of WGD+/− cells. Mixed tumors had an intermediary phenotype for growth rate, fraction of $CD8^+$ T cells, and $CD8^+$ T cell/Treg ratio (Figures 3H and 3I). Higher DNA content was maintained in $EpCAM^+CD45^-$ cells; thus, the incomplete immunosuppressive phenotype was not due to loss of WGD+ cell tetraploidy (Figure S6J).

To assess clinical relevance, we analyzed associations between WGD and immune scores in the TCGA[22] and METABRIC[28] cohorts. We also retrieved WGD from the FUSCC TNBC cohort based on ploidy>2.7[35] (Figure S6K). In the METABRIC cohort, immune scores were significantly lower in WGD+ tumors across all three subtypes, with a similar trend in the TCGA and no difference in the FUSCC TNBC cohorts (Figure S6L). Lower immune scores in WGD+ tumors in the METABRIC cohort were observed regardless of *TP53* status (Figure S6M). To minimize confounding factors that influence immune infiltration, we stratified each cohort into high and low purity (i.e., tumor cell content) groups. Consistent differences were observed in both high and low purity subgroups within the METABRIC cohort, whereas in the TCGA cohort, the difference was significant only in the low purity group (Figure S6N). A similar trend was also observed in the FUSCC high-purity tumor subset. Recognizing the substantial inter-patient and inter-cohort heterogeneity, we performed a random-effects meta-analysis by integrating effect sizes across the cohorts. This pooled analysis demonstrated that WGD+ tumors exhibit significantly lower overall immune infiltration scores, particularly when stratified by tumor purity (Figure 3J). Accordingly, leukocyte content was significantly lower in WGD+ tumors in each subtype in the TCGA low-purity tumors and the $CD8^+$ T cell/total cell ratio in low-purity TNBC in the METABRIC dataset (Figures S6O).

Diminished antigen presentation in WGD+ tumors

To investigate cellular and molecular differences, we performed scRNA-seq on TA3 WGD- and WGD+ tumors collected on day 14 from NSG and A/J mice (n = 3 per group) (Figures 4A–4D and S7A–S7D). WGD+ tumors in A/J mice had more cancer cells, fibroblasts, and neutrophils, and fewer macrophages/monocytes and T cells (Figure 4D). WGD+ tumors had more myeloid cells and fibroblasts but fewer cancer cells in NSG mice (Figure S7D). scATAC-seq on WGD+ tumors confirmed homogenously tetraploid cancer cells (Figure 4E). Because growth differences and immune escape were only observed in A/J mice, we analyzed scRNA-seq from these tumors. Milo neighborhood analysis of all cells identified cancer cells as the most WGD+ tumor-enriched neighborhood (Figures 4F and 4G).

Subclustering of each major cell type did not detect significant differences in fibroblasts (Figures S7E–S7H). Among myeloid populations, there was an increased fraction of M2-like macrophages and neutrophils in WGD+ tumors, accompanied by a reduction in monocytes (Figures S7I–S7L). We also detected elevated module scores for a myeloid-derived suppressor cell (MDSC) signature[36] (Figure S7M). Among T cells, there were significantly fewer cytotoxic $CD8^+$ and more regulatory T cells in WGD+ tumors (Figures S7N–S7P). UMAP plot by Louvain clustering of cancer cells demonstrated three major subclusters distinguished by the expression of proliferation, immune, and cell adhesion-related genes (Figures 4H and S7Q–S7S). Global gene set enrichment analysis (GSEA) of cancer cell expression profiles indicated enrichment for epithelial-mesenchymal transition in WGD+ tumors, whereas immune-related pathways (e.g., IFN signaling) were significantly enriched in WGD- tumors (Figure 4I). The top 10 DEGs with higher levels in WGD- cancer cells were related to antigen processing (e.g., *Psmb9*) and major complex of histocompatibility I (MHC-I) (e.g., *B2m*, *H2-Q2*, and *H2-K1*) (Figure 4J; Table S4).

Combined analysis of cancer cells from A/J and NSG mice revealed that the lower expression of antigen presentation genes in WGD+ cells was only observed in A/J mice and that these genes overall had higher expression in A/J mice (Figures 4K, 4L, and S7T). WGD+ cells in culture had slightly

(G) Relative fraction of $CD8^+$ T cells and $CD8^+$/Treg ratio quantified by flow cytometry (n = 4–5/condition).
(H) Tumor growth derived from 10^5 TA3 WGD- or WGD+ cells or a 1:1 mixture of WGD- and WGD+ cells in A/J mice (n = 10/condition). p-value color: comparison to 100% WGD- (black) and mixed (purple) tumors.
(I) Relative fraction of $CD8^+$ T cells and $CD8^+$/Treg ratio quantified by flow cytometry (n = 7–9/condition).
(J) Forest plot of observed outcome of immune score shifts in WGD- and WGD+ TNBC in the indicated cohorts and tumor purity. Two-sided Wald-type test on the pooled effect size. Error bars represent ±SEM (A, B, C, F, G, H, I) or 95% Confidence Interval (J). Mann-Whitney U test (B, C). Kruskal-Wallis test (G, I). Two-ways ANOVA analysis-Tukey's multiple comparisons test (F, H). See also Figures S4–S6.

Please cite this article in press as: Foidart et al., Whole-genome doubling drives immune evasion by silencing antigen presentation, Cancer Cell (2026), https://doi.org/10.1016/j.ccell.2026.04.007

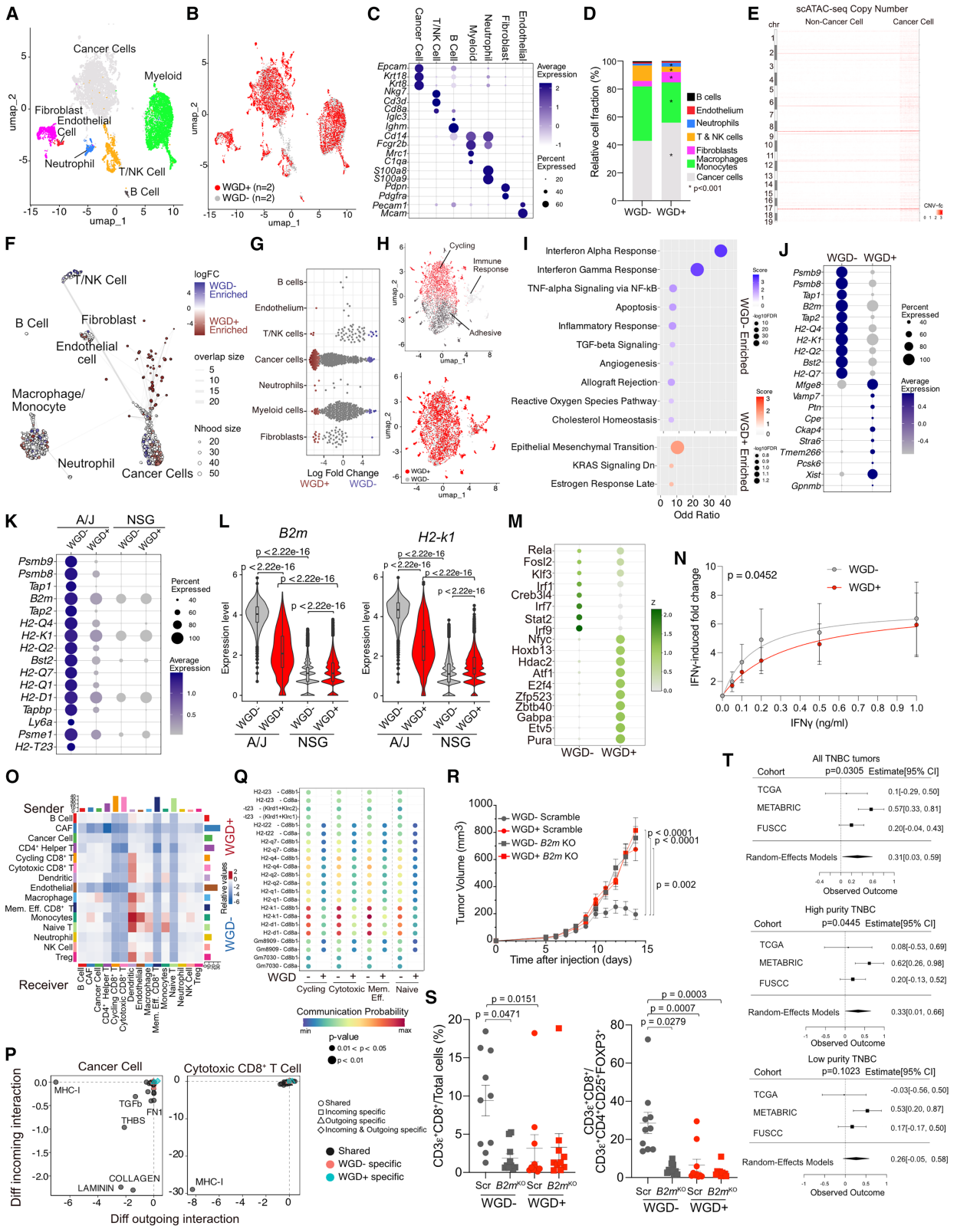

Figure 4. Impact of WGD on the immune environment

(A and B) UMAP of WGD- and WGD+ tumor scRNA-seq data colored by cell cluster (A) and genotype (B) in A/J mice.

(C) Marker genes enrichment in the indicated cell subtypes in A.

(legend continued on next page)

Please cite this article in press as: Foidart et al., Whole-genome doubling drives immune evasion by silencing antigen presentation, Cancer Cell (2026), https://doi.org/10.1016/j.ccell.2026.04.007

higher expression of *B2m*, *H2-D1,* and *H2-K1* (Figure S7U). The estimation of transcriptional regulators using SCENIC on cancer cell scRNA-seq data predicted Irf9, Irf7, and Stat2 as top regulators of WGD- cells (Figure 4M), indicative of activated interferon response. Assessing IFNγ stimulation *in vitro* using cell surface B2M expression by flow cytometry as readout revealed diminished response in WGD+ cells (Figure 4N), suggesting that lower expression of antigen presentation genes in A/J mice might be due to diminished response to tumor microenvironmental cues.

Assessing interactions among cells within tumors by CellChat[37] showed enrichment of dendritic cells and, to a lesser degree, endothelial cell and macrophage interactions in WGD+ tumors, while $CD8^+$ T cell interactions dominated in WGD- tumors (Figure 4O). All communication of cancer cells with leukocytes and cancer-associated fibroblasts was more pronounced in WGD- tumors (Figure 4O). Analysis of MHC-I ligand receptor pairs between cancer cells and $CD8^+$ T cells showed diminished interactions in WGD+ tumors (Figures 4P and 4Q).

To test if differences in tumor growth are due to differences in antigen presentation, we deleted *B2m*, a major component of the MHC-I complex, in both WGD- and WGD+ cells (Figure S7V). Loss of B2M accelerated WGD- tumor growth compared to scramble control, while no effect was seen in WGD+ tumors (Figure 4R). The deletion of *B2m* also diminished $CD8^+$ T cell infiltration and reduced $CD8^+$ T cell to Treg ratio in WGD- tumors (Figure 4S).

The analysis of tumor epithelial cell antigen presentation across our additional WGD models by flow cytometry of $EpCAM^+CD45^-$ cells revealed significantly lower H2-Dd expression in 168fARN WGD+ tumors and no difference in B2M, while TA3 CF WGD+ tumors exhibited higher B2M and H2-Dd (Figure S8A).

The analysis of antigen presentation and MHC-related gene signatures in TNBC patient cohorts revealed significantly lower antigen presentation scores in the METABRIC and a downward trend in the FUSCC cohort (Figure S8B). When tumors were further stratified by purity, reduction in antigen presentation became more consistent across the three cohorts, with the exception of low-purity tumors in TCGA (Figure S8B). Random-effects meta-analysis integrating the three datasets demonstrated significantly lower antigen presentation scores in WGD+ tumors across all TNBC, and specifically in high-purity TNBC tumors (Figure 4T). Reduced antigen presentation signatures in WGD+ TNBC were consistent in both *TP53* WT and mutant cases in the METABRIC cohort (Figure S8C). Further analysis of individual MHC-I and MHC-II gene expression in the METABRIC TNBC cohort revealed selectively reduced expression of certain MHC-I genes (e.g., *HLA-E* and *B2M*) in WGD+ tumors, while MHC-II genes were broadly and consistently downregulated (Figure S8D).

To further validate these findings, we analyzed two intra-patient paired breast cancer bone metastases from our prior study,[38] with one WGD- lesion and one WGD+ (Figure S8E). ScRNA-seq showed that the WGD+ tumor had reduced T cell infiltration (Figures S8F–S8G) and lower expression of multiple HLA genes and *B2M* in cancer cells (Figure S8H). Lastly, we examined the induction of HLA and B2M expression following IFNγ treatment in eight breast cancer patient-derived organoid (PDO) models, including four WGD- and four WGD+, classified by Hoechst staining for DNA content (Figure S8I), FACETS ploidy prediction, and karyotyping of metaphase spread in three models (Figure S8J). WGD+ PDOs exhibited a trend toward reduced HLA and B2M induction (Figures S8K and S8L).

Time course of WGD-associated immune escape

To determine if the immunosuppressive environment of WGD+ tumors is selected during tumor growth, we performed a time course experiment and analyzed tumors at early (day 8) and late (day 14) time points (Figures 5A and 5B). Flow cytometry revealed significantly more $CD45^+$ leukocytes and T cells in WGD+ on day 8, with differences disappearing ($CD45^+$ cells) or even showing an opposite pattern (T cells) by day 14 (Figure 5C). The relative fraction of $CD8^+$ T cells and $CD8^+$ T cell/Treg ratio were low in all tumors on day 8 and remained

(D) Percentage of each cell subtype normalized to total cells in WGD- and WGD+ tumors. Fisher's exact test.
(E) Heatmap shows estimated copy number of all cells using scATCA-seq from a WGD+ tumor.
(F) Milo neighborhood clustering of all cells based on scRNA-seq. Differentially enriched neighborhoods (FDR<0.05) are color coded.
(G) Plot quantifying log2 fold change of all identified milo neighborhoods in F separated by cell types.
(H) UMAP shows clustering of tumor epithelial cells from A/J mice colored by cluster marker-gene function (top) and genotype (bottom).
(I) Significantly (FDR<0.05) enriched Hallmark pathways in DEGs (FDR<0.05).
(J) Top 10 differentially expressed genes.
(K) Top differentially expressed antigen presentation genes in cancer cells from the indicated tumors.
(L) *B2m* and *H2-k1* expression in cancer cells. Boxplots represent the median (center line) and interquartile range (box, 25th-75th percentiles). Whiskers extend to 1.5× the interquartile range. Mann-Whitney U test.
(M) Enrichment *Z* score of top predicted regulators in WGD- and WGD+ cancer cells by SCENIC.
(N) Relative expression of B2M normalized to vehicle control after IFNγ stimulation for 16 h (merged from three independent experiments). Extra sum-of-squares F test.
(O) Heatmap illustrating alterations of cell-to-cell communication strength between each of the indicated cell types. Enhanced (red) and attenuated (blue) cell chat in WGD+ tumor.
(P) Alterations of outgoing and incoming signals in cancer cells and cytotoxic $CD8^+$ T cells.
(Q) Communication probabilities and significances of all the curated MHC-I ligand-receptor pairs from cancer cells (sender) to each type of $CD8^+$ T cells (receiver).
(R) Volume of scramble control (Scr) and *B2m* KO WGD- or WGD+ tumors in A/J mice (n = 16/condition). Two-Way ANOVA-Tukey's multiple comparisons test.
(S) Relative fraction of $CD8^+$ T cells and $CD8^+$ T cell/Treg ratio quantified by flow cytometry in scramble control (Scr) and *B2m* KO tumors in A/J mice (n = 9–10/condition). Kruskal-Wallis test.
(T) Forest plot shows observed outcome of KEGG antigen presentation enrichment score shift in WGD- and WGD+ TNBC from the indicated cohorts and tumor purity. Two-sided Wald-type test was used on the pooled effect size. Dot size represents -log10(FDR) and color indicates enrichment scores (I, K). Error bars represent ±SD (N), ±SEM (R, S), or 95% confidence interval (T). See also Figures S7 and S8; Table S4.

Please cite this article in press as: Foidart et al., Whole-genome doubling drives immune evasion by silencing antigen presentation, Cancer Cell (2026), https://doi.org/10.1016/j.ccell.2026.04.007

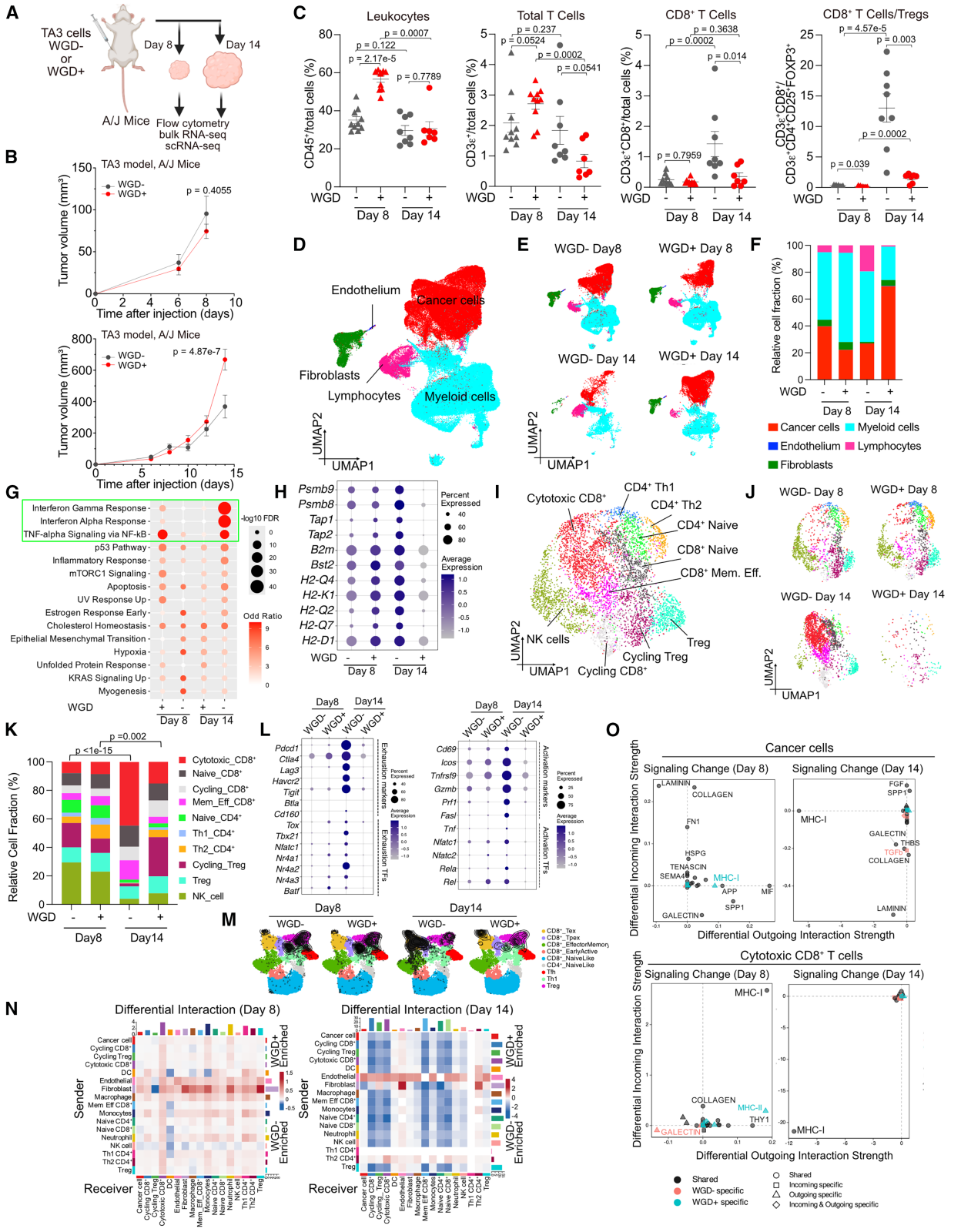

Figure 5. Time course of immune environmental changes

(A) Schematic of time course experiment.

(B) Growth of tumors derived from TA3 WGD- or WGD+ cells in A/J mice collected on day 8 (top) and day 14 (bottom), n = 7–10/condition. Two-ways ANOVA.

(legend continued on next page)

Please cite this article in press as: Foidart et al., Whole-genome doubling drives immune evasion by silencing antigen presentation, Cancer Cell (2026), https://doi.org/10.1016/j.ccell.2026.04.007

low in WGD+ tumors but increased in WGD- (Figure 5C). RNA-seq profiling of bulk tumors showed higher expression of IFN-induced genes and a trend of higher immune scores in WGD+ tumors on day 8, but the reverse on day 14, and the stromal score also decreased in WGD+ tumors by day 14 (Figures S9A and S9B). The analysis of DEGs between WGD-/+ tumors at different time points revealed a prominent overlap between genes that were WGD+ high on day 8 but became WGD- high by day 14, with limited to no overlap between any other groups (Figure S9C). Comparison of pathway enrichment gave similar results, with IFN signaling-related pathways being more enriched in WGD+ tumors on day 8 and the opposite seen on day 14 (Figures S9D and S9E).

To explore differences in more depth, we performed scRNA-seq on selected tumors from both time points ($n = 2$ per group). UMAP of all cells depicted notable shifts in the relative fraction of major cell types between day 8 and 14 in both WGD- and WGD+ tumors. Myeloid and cancer cells dominated WGD+ tumors on day 8 and 14, respectively, while the most pronounced change in WGD- tumors was the increase in lymphocytes from day 8–14 (Figures 5D–5F and S9F). We further subclustered each cell type for in-depth analysis. We detected three cancer cell subclusters defined based on epithelial-mesenchymal features with no differences in their relative ratios depending on time and WGD status (Figures S9G–S9J). However, pathways differentially enriched between WGD- and WGD+ tumors showed prominent time-dependent changes, with IFN and TNFα signaling being more enriched in WGD+ tumors on day 8, which were reversed on day 14 (Figure 5G). Genes involved in antigen presentation showed the same time-dependent changes, although differences between WGD+ and WGD-tumors on day 8 were less pronounced (Figure 5H; Table S4). $CD8^+$ T cells showed the most striking differences with a large increase in WGD-tumors from day 8–14 (Figures 5I–5K and S9K). T cells showed a marked increase in both activation and exhaustion markers from day 8 to day 14 in WGD-tumors (Figure 5L). Integrative functional analysis using ProjecTILs[39] further confirmed that T cells in WGD-tumors were largely in progenitor exhausted and effector-like state by day 14. In contrast, T cells in WGD+ tumors progressively shifted toward a Treg-like state (Figure 5M). In myeloid cells, we observed a substantial increase in neutrophils and decrease of *Folr2* high macrophages in WGD-tumors from day 8 to day 14, while their frequencies in WGD+ tumors remained similar (Figures S9L–S9O). The analysis of cellular interactions using CellChat revealed more interactions in WGD+ than in WGD-tumors on day 8 with dendritic cells, fibroblasts, and macrophages being the most interactive, but this pattern flipped by day 14 (Figure 5N). MHC-I signaling in cancer cells and $CD8^+$ T cells also showed similar differences and changes with time (Figure 5O).

To define changes between days 8–14, we collected tumors at additional time points (day 8, 10, 12, and 14). Growth of WGD+ tumors accelerated at day 10, with further rapid growth observed at days 12 and 14 (Figure S9P). Flow cytometry demonstrated inverse dynamics of antigen presentation and immune infiltration. The expression of B2M, H2Kk, and H2Dd on $EpCAM^+CD45^-$ cancer cells showed significantly lower levels in WGD+ tumors, with the difference between WGD+ and WGD- tumors remaining significant at day 14 (Figure S9Q). In WGD- tumors, total T cells and $CD8^+$ T cells began to infiltrate at day 12 and increased markedly by day 14, while T cell numbers remained low in WGD+ tumors (Figure S9R). WGD+ tumors had significantly fewer total $CD45^+$ cells at day 14 (Figure S9R). Immunohistochemistry for pSTAT1 showed higher levels in WGD+ tumors at day 8 that further increased by day 10, followed by a decline (Figure S9S). Cytokine array analysis of pooled tumor lysates revealed that IFNγ production was reduced in WGD+ tumors beginning at day 12, with further decline by day 14, consistent with the pattern of T cell infiltration. Conversely, several inflammatory and immunosuppressive cytokines were elevated at later time points in WGD+ tumors (Figure S9T).

Molecular mechanisms underlying WGD-associated decrease in antigen presentation

We investigated potential mechanisms underlying diminished antigen presentation in WGD+ tumor cells *in vivo*. By integrating scRNA-seq and scATAC-seq to identify gene expression changes associated with chromatin alterations using BETA,[40] we found that ATAC-seq peaks lost in WGD+ cancer cells were associated with downregulated genes (Figures 6A, S10A, and S10B; Table S4). GSEA on these downregulated genes showed that the top pathways are immune-related, including IFN signaling (Figure 6B). Genomic tracks of selected antigen presentation genes (e.g., *H2-d1* and *H2-k1*) also showed a decrease in ATAC peak signal in WGD+ cells (Figures 6C and S10C). TCGA scATAC-seq data[41] revealed consistently more closed chromatin in cancer cells in WGD+ basal tumors and

(C) Immune cell populations quantified by flow cytometry in WGD- and WGD+ tumors on day 8 and day 14 in A/J mice (n = 7–10). Kruskal-Wallis test.
(D and E) UMAPs of WGD- and WGD+ tumor scRNA-seq data colored by cell type, all samples combined (D) and separated by groups (E).
(F) Percentage of each cell type normalized to total cells in the indicated groups.
(G) Significantly (FDR<0.05) enriched Hallmark pathways in DEGs (top 300 up- or down-regulated genes with FDR<0.05) in WGD- and WGD+ cancer cells. Dot size represents log10FDR, and color indicates enrichment odd ratios. Green rectangle highlights pathways showing inverse pattern between the different time points.
(H) Expression of differentially expressed antigen presentation genes in WGD- and WGD+ cancer cells.
(I and J) UMAPs of lymphocyte subclustering by cell type, all samples combined (I) or separated into the indicated groups (J).
(K) Percentage of lymphocyte subtypes normalized to total T cells. Fisher's exact test was used to compare $CD8^+$ T cell fractions.
(L) T cell activation and exhaustion marker genes enrichment in lymphocyte subtypes.
(M) UMAP shows lymphocyte state projection on the mouse lymphocyte reference atlas based on the ProjecTILs package.
(N) Heatmaps illustrate alterations of cell-to-cell communication strength between each of the indicated cell types between WGD- and WGD+ tumors on days 8 and 14. Enhanced (red) and attenuated (blue) cell chat in WGD+ tumors.
(O) Alterations of outgoing and incoming signal terms in cancer cells (top) and cytotoxic $CD8^+$ T cells (bottom) between WGD- and WGD+ tumors on day 8 and day 14. Error bars represent ±SEM (B, C). See also Figure S9; Table S4.

Please cite this article in press as: Foidart et al., Whole-genome doubling drives immune evasion by silencing antigen presentation, Cancer Cell (2026), https://doi.org/10.1016/j.ccell.2026.04.007

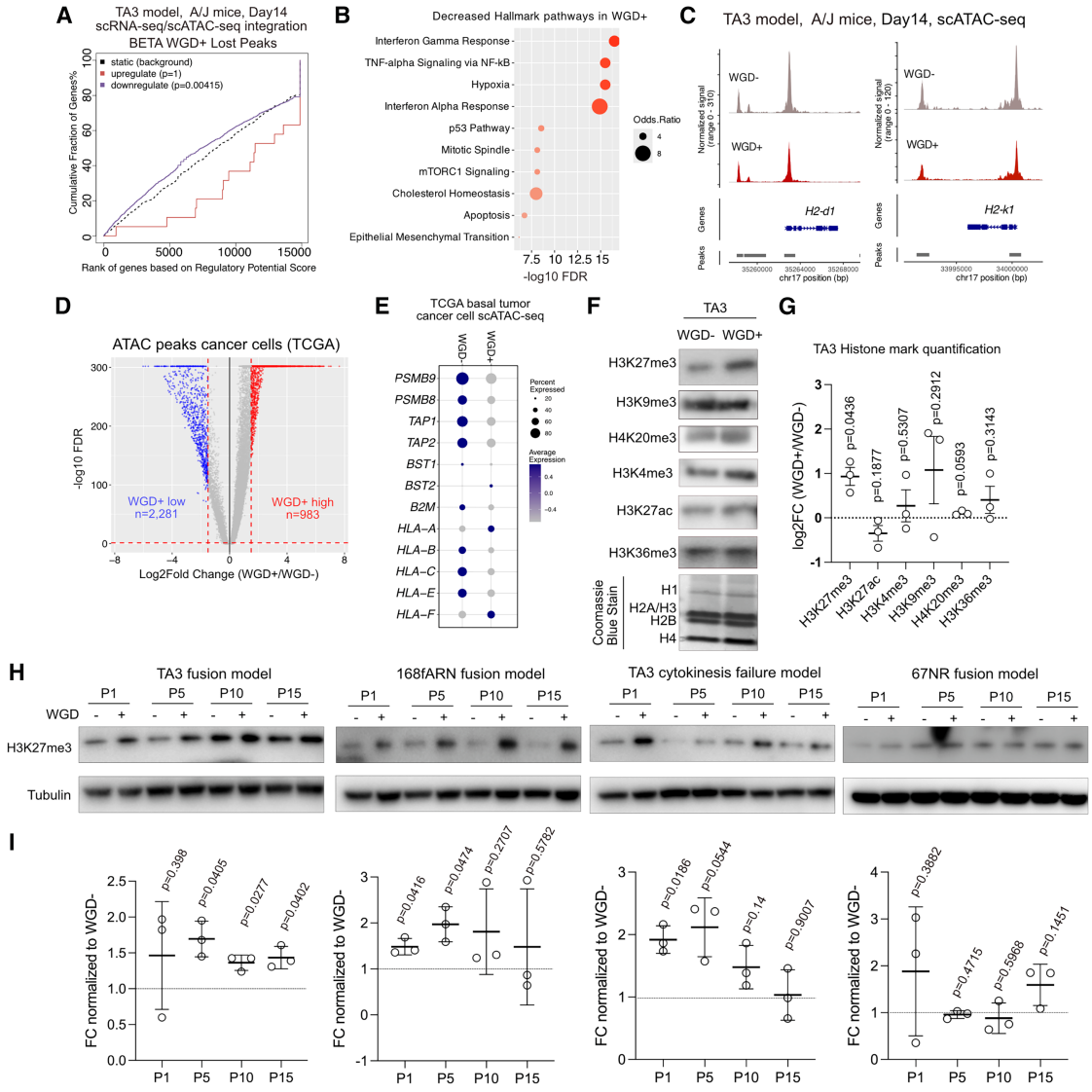

Figure 6. Epigenetic regulation of antigen presentation

(A) BETA association of WGD+ cancer cells lost ATAC peaks with DEGs from scRNA-seq. One-sided Kolmogorov-Smirnov test.

(B) Significantly (FDR<0.05) enriched Hallmark pathways in genes with significantly (FDR<0.05) lower expression in WGD+ TA3 cancer cells associated with significantly lost ATAC peaks. Dots were ranked by levels of significance (-log10FDR) and dot size represents odds ratio of each pathway.

(C) Genomic track view of average ATAC-seq signal at *H2-d1* and *H2-k1* genomic loci in WGD- and WGD+ TA3 cancer cells. Signal intensity was adjusted using the same scale for each group.

(D) Differential ATAC peaks (FDR<0.05, |log2FC|>1.5) between cancer cells extracted from TCGA basal breast tumors (WGD-*n* = 2; WGD+ *n* = 4).

(E) Expression of MHC-I and genes regulating antigen presentation in cancer cells from TCGA basal breast tumors.

(F) Immunoblot for the indicated histone marks in TA3 WGD- and WGD+ cells. Coomassie blue staining was used as a loading control.

(G) log2 fold change of the indicated histone modification in TA3 WGD+ cells normalized to WGD-cells, merged from 3 independent repeats. One-sample *t* test was used to compare to 0.

(H) Immunoblot for H3K27me3 in four different WGD models at four different passages. Tubulin was used as a loading control. Quantification of H3K27me3 ratio fold difference between WGD+ and WGD-cells at each passage is indicated.

(I) Fold change of H3K27me3 at the indicated time point of collection in TA3 WGD+ cells, normalized to WGD-cells, merged from 3 independent repeats. One-sample *t* test was used to compare to 1. Error bars represent ±SEM (G) or ±SD (I). See also Figure S10; Table S4.

decreased chromatin accessibility of antigen presentation-related genes (Figures 6D and 6E).

To explore potential differences in histone marks associated with active (H3K4me3, H3K27ac, and H3K36me3) and repressive (H3K27me3, H3K9me3, and H4K20me3) chromatin, we performed immunoblot analyses of TA3 WGD- and WGD+ cell lysates. Higher levels of the H3K27me3 with a declining trend of H3K27ac were observed in WGD+ cells (Figures 6F and 6G). Elevated H3K27me3 in WGD+ cells was also present in 168fARN fusion and TA3 CF WGD+ models but not in 67NR

Please cite this article in press as: Foidart et al., Whole-genome doubling drives immune evasion by silencing antigen presentation, Cancer Cell (2026), https://doi.org/10.1016/j.ccell.2026.04.007

CellPress
OPEN ACCESS

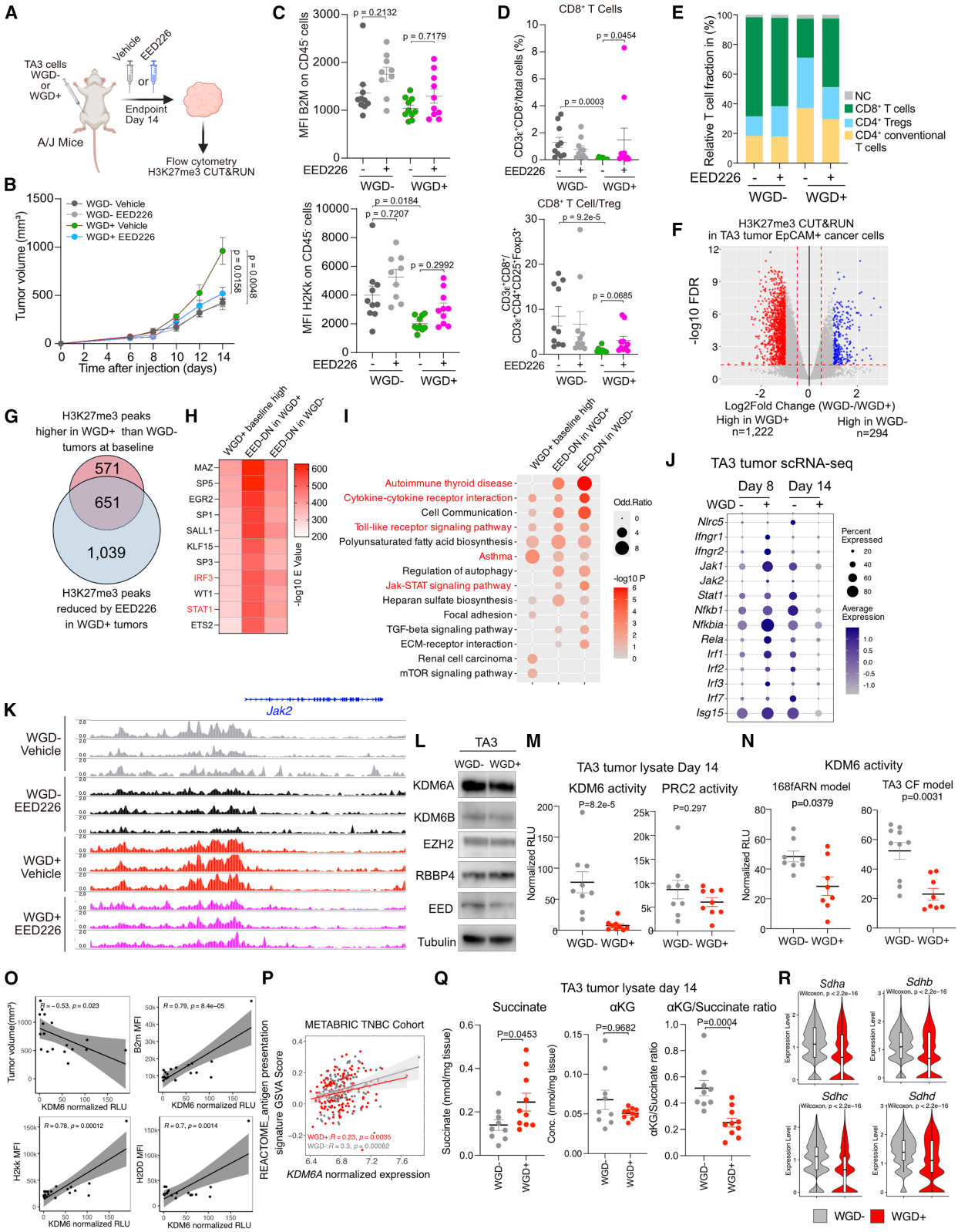

Figure 7. Epigenetic regulation of antigen presentation

(A) Schematic of the EED226 treatment experiment.

B) Tumor volume of TA3 WGD- or WGD+ cells in A/J mice treated with vehicle or EED226 (n = 10/condition). Two-ways ANOVA analysis was used in each pair of comparison.

(legend continued on next page)

Please cite this article in press as: Foidart et al., Whole-genome doubling drives immune evasion by silencing antigen presentation, Cancer Cell (2026), https://doi.org/10.1016/j.ccell.2026.04.007

WGD+ cells, and was stably maintained over 15 passages (Figures 6H and 6I). Higher H3K27me3 was also detected in TA3 WGD+ tumors throughout day 8 to day 14 (Figures S10D and S10E).

To test if decreasing H3K27me3 would abolish WGD-associated immune evasion, we injected TA3 WGD- and WGD+ cells into A/J mice and treated them with vehicle or EED226, a potent inhibitor of H3K27me3 methyltransferase PRC2 complex[42] (Figure 7A). EED226 treatment significantly decreased WGD+ but not WGD- tumor growth (Figure 7B). This decrease was associated with a trend of increased levels of B2M and H2KK on CD45$^-$ cells (Figure 7C). We also observed significantly increased CD8$^+$ T cells and an increasing trend of CD8$^+$ T cell to Treg ratio in WGD+ tumors upon EED226 treatment (Figures 7D and 7E), and CD8$^+$ T cell abundances positively correlated with both B2M and H2-Kk levels on CD45$^-$ cells (Figure S10F). There was no noticeable change in overall T cell frequencies and composition in WGD- tumors upon EED226 treatment despite increased antigen presentation on CD45$^-$ cells. In the 168fARN model, EED226 treatment did not affect growth, antigen presentation, and immune environment of either WGD- nor WGD+ tumors (Figures S10G and S10H).

To determine if antigen presentation is directly silenced by H3K27me3 in WGD+ tumor cells and if this is alleviated by EED226 treatment, we performed H3K27me3 CUT&Run on EpCAM$^+$ cancer cells isolated by FACS from WGD- and WGD+ tumors from vehicle and EED226-treated mice. We detected more H3K27me3 peaks in WGD+ than in WGD- cells (Figure 7F; Table S4). EED226 treatment decreased the number of H3K27me3 peaks in both WGD- and WGD+ cells, with a more pronounced decrease in WGD+ cells (Figure 7G and S10I; Table S4). However, we did not detect differences in H3K27me3 signal at the promoter regions of *H2k1* and *B2m* between WGD- and WGD+ cells, neither at baseline nor after EED226 treatment (Figure S10J). This suggests that the decreased expression of MHC-I in WGD+ cells is not due to direct suppression by H3K27me3 but rather a consequence of potential differences in transcriptional regulators. We performed motif enrichment analysis on the union of H3K27me3 peaks that were either higher in WGD+ cells at baseline or decreased by EED226 treatment in WGD- or WGD+ cells and identified IRF3 and STAT1, key regulators of IFN-induced gene expression, as being among the top 10 consistently enriched transcriptional factors (TFs) (Figure 7H), suggesting that limited chromatin accessibility for these TFs in WGD+ cells might explain their diminished IFN responsiveness. Pathway enrichment analysis of genes proximal to the union of these differential H3K27me3 peaks also identified several immune-related pathways, including JAK-STAT signaling and cytokine-cytokine receptor interaction (Figure 7I). We found lower baseline expression of many IFN response genes, including *Jak2* and *Stat1*, and the master regulator of antigen presentation, *Nlrc5*, in WGD+ cells on day 14, but showing the opposite pattern on day 8 (Figure 7J). The promoter region of *Jak2* showed a higher baseline H3K27me3 signal in WGD+ tumors that was decreased by EED226 treatment (Figure 7K).

The analysis of GSVA scores for IL6-JAK2-STAT3 signaling and IFNγ response pathways and expression of individual pathway components in deconvoluted tumor cell components from TNBC in the METABRIC cohort revealed significantly lower scores for both pathways and lower expression of *IRF1*, *IRF3, IRF7, STAT1*, and *NFKB1* in WGD+ tumors (Figures S10K and S10L).

To explore potential mechanisms of increased H3K27me3 in WGD+ tumor cells, we assessed protein levels and enzymatic activities of H3K27me3 demethylases (KDM6A/KDM6B) and methyltransferases (PRC2 complex) in tumor lysates. We observed no significant differences in protein levels (Figure 7L) but detected markedly lower KDM6 activity in WGD+ tumors, whereas PRC2 activity was essentially the same (Figure 7M). Lower KDM6 activity in WGD+ tumors was also observed in the 168fARN fusion and TA3 CF models (Figure 7N).

KDM6 activity showed a significant positive correlation with the expression of all three MHC-I in tumor cells and a negative correlation with tumor volumes in our model (Figure 7O). We also observed a positive correlation between antigen presentation

(C) B2M and H-2KK mean expression quantified by flow cytometry in CD45$^-$ cells of each tumor from the indicated groups (n = 9–10 tumors/condition).
(D) Frequency of CD3$^+$CD8$^+$ cells quantified by flow cytometry in each tumor and treatment group (*n* = 10 tumors/condition).
(E) Stacked bar plot shows percentages of CD8$^+$ T cells, CD4$^+$ Tregs, CD4$^+$ conventional T cells and uncharacterized T cells normalized to the total T cell population in each indicated group.
(F) Differential H3K27me3 peaks (FDR<0.05, |log2FC|>1) derived from CUT&RUN between cancer cells sorted from WGD- and WGD+ tumors (*n* = 3 in each group).
(G) Overlap between gained H3K27me3 peaks in WGD+ compared to WGD-tumors and H3K27me3 peaks reduced by EED226 treatment in WGD+ tumors.
(H) Heatmap shows union of top 10 enriched motifs in the three indicated H3K27me3 peak sets.
(I) Union of significantly enriched KEGG pathways in the three indicated H3K27me3 regions.
(J) Expression of genes encoding interferon response regulators in WGD- or WGD+ cancer cells from the time course experiment.
(K) Genomic track view of H3K27me3 signal at *Jak2* genomic loci. Signal intensity was adjusted using the same scale for each group.
(L) Immunoblot for regulators of H3K27me3 levels in TA3 WGD- and WGD+ cells with tubulin as loading control.
(M and N) Tissue weight normalized RLU for KDM6 and PRC2 activity in lysates of WGD- and WGD+ tumors of TA3 (M) and 168fARN (N) fusion models and TA3 CF model (N), *n* = 10 or 8.
(O) Pearson's correlation of KDM6 activity with tumor volumes or MHC-I expression on EpCAM$^+$CD45$^-$ cancer cells from tumors collected at day 14 from the experiment in Figure S10.
(P) Pearson's correlation of KDM6A expression and REACTOME MHC-I mediated antigen presentation signature enrichment score in METABRIC TNBC cohort classified by WGD status.
(Q) Levels of succinate, alpha ketoglutarate (αKG), and their ratios in tumor lysate of TA3 tumors collected at day 14 (n = 9–10/group).
(R) Expression of genes encoding succinate dehydrogenase subunits in tumor epithelial cells in TA3 tumors collected at day 14. Boxplots represent the median (center line) and interquartile range (box, 25th-75th percentiles). Whiskers extend to 1.5× the interquartile range. Error bar represents ±SEM (B, C, D, M, N, Q). Kruskal-Wallis test (C, D). Mann-Whitney U test (M, N, Q). See also Figure S10; Table S4.

Please cite this article in press as: Foidart et al., Whole-genome doubling drives immune evasion by silencing antigen presentation, Cancer Cell (2026), https://doi.org/10.1016/j.ccell.2026.04.007

and *KDM6A* expression in the METABRIC TNBC cohort (Figure 7P). KDM6A/B are α-ketoglutarate (αKG)-dependent histone demethylases, and their activities are tightly regulated by TCA cycle metabolites, activated by αKG and inhibited by succinate.[43] We assessed αKG and succinate levels in TA3 tumors and found significantly higher succinate and αKG/succinate ratio in WGD+ tumors (Figure 7Q). Higher succinate levels were also observed in WGD+ tumors from the TA3 CF model, and a similar trend was seen in 168fARN WGD+ tumors, while no differences were observed in αKG and αKG/succinate ratios (Figure S10M). The analysis of the expression of key enzymes involved in αKG to succinate conversion in the TA3 fusion model scRNA-seq data revealed significantly lower expression of all succinate dehydrogenase subunits in WGD+ cancer cells (Figure 7R).

DISCUSSION

WGD is one of the most common genetic alterations in human cancers, generally associated with metastatic disease and resistance to treatment.[26,44] Considering that whole-genome sequencing studies have a limited ability to detect subclonal WGD, the frequency of WGD is likely to be higher than current estimates, and subclonal and clonal WGD may have different effects. For example, subclonal WGD in lung cancer was associated with poor clinical outcome, while truncal WGD was not.[45] Due to the association of WGD with poor prognosis and the attractive hypothesis of targeting WGD+ cells while sparing normal diploid cells, several genome-wide screens have been conducted to find tetraploid cell-specific therapeutic targets.[23,46] Among others, KIF18A was identified as a WGD+ cell line-specific dependency via Project Achilles,[23] and KIF18 inhibitors have entered phase I clinical trials.[47] More recently, comprehensive profiling of diploid and tetraploid derivatives of RPE1-hTERT cells revealed preferential sensitivity of tetraploid cells to proteasome inhibitors,[48] which were also WGD+ cell-specific hits in our SMI screen.

In our experimental model of WGD, the most dramatic differences were observed in immunocompetent mice due to WGD-associated immune evasion. WGD+ cells have diminished antigen presentation due to muted IFNγ response, and this is at least in part due to the epigenetic silencing of transcriptional regulators of MHC-I expression. WGD+ cells have less accessible chromatin and higher H3K27me3 due to decreased KDM6 activity associated with elevated succinate. Adaptation to WGD might perturb the nuclear-mitochondrial balance, leading to perturbed mitochondrial function, a hypothesis that warrants further investigation. Both decreased and increased levels of PRC2 activity/H3K27me3 levels have been associated with tumorigenesis and genomic instability,[49] leading to the approval of EZH2 inhibitors for cancer treatment.[50] EZH2 inhibition also potentiates the efficacy of targeted and immunotherapies.[50] Accordingly, EED226 treatment on our WGD model increased B2M expression in both WGD- and WGD+ tumor cells, but a phenotypic consequence of this was only observed in WGD+ tumors in the TA3 model where EED226 decreased tumor growth and increased T cell infiltration. Other mechanisms such as elevated neutrophil-derived MDSC signatures and chronic-inflammatory cytokines (e.g., TNFα, GM-CSF, and angiopoietin-2) might also contribute to the WGD-associated immunosuppressive phenotype. The precise mechanisms linking this sustained inflammation to immune suppression in WGD+ tumors warrant further investigation. A recent report also described a similar immunosuppressive phenotype in WGD+ ovarian cancer, associated with repressed cGas-STING signaling.[51] Thus, immune evasion in WGD+ tumors is likely driven by diverse mechanisms.

Aneuploidy has been associated with immune suppression, and a recent study described that WGD+ bladder cancers have a higher fraction of neutrophils and PD-1$^+$ cells,[52] consistent with our finding of higher anti-PD-L1 sensitivity in WGD+ tumors. However, human tumors are rarely composed of pure populations of WGD+ cells, especially when WGD is acquired. Our finding that the phenotype of mixed tumors was between that of pure WGD- and WGD+ tumors suggests that WGD-triggered immune evasion is cell autonomous, at least in the model we tested. The immune suppressive phenotype of WGD+ tumors was observed at later time points, and initially, WGD+ tumors were more immunogenic, implying potential immune editing or selection for cancer cells with muted antigen presentation that then create a cold immune microenvironment.[53]

In summary, our results in a preclinical model of WGD have advanced our understanding of mechanisms by which WGD drives tumor evolution, and they serve as a basis for the design of future clinical trials improving treatment efficacy in WGD+ TNBC.

Limitations of this study

We used mouse mammary tumor cell lines, which were necessary to study WGD in an immunocompetent host. Predominantly used the TA3 model due to TA3 being the only nearly diploid tumorigenic mammary tumor cell line. However, several key experiments in the 168fARN fusion model yielded similar results. More importantly, we validated our findings in clinical cohorts, intra-patient metastatic lesions, and PDOs. However, special caution is warranted in interpreting transcriptomic analyses performed on bulk tumor samples where signals may be confounded by non-tumor components. In addition, substantial inter-cohort variation was observed, although the overall trend remained consistent, particularly after stratification by tumor purity. Experimental validation is needed in future studies to directly assess cancer cell MHC-I protein levels in clinical samples with WGD status.

We generated WGD+ by somatic cell fusion due to its lower likelihood of triggering DNA damage response, replication stress, and chromosomal abnormalities compared to other methods of tetraploid cell generation. We also created a TA3 CF model of WGD and found similarities but also differences compared to the fusion model, suggesting that the way WGD is achieved might impact tumor evolution. The mouse cell lines used were WT for *Trp53*, which might decrease the probability of genomic instability, making it more likely that the observed differences between WGD- and WGD+ tumors are truly ploidy related.

RESOURCE AVAILABILITY

Lead contact

Further information and requests for resources and reagents should be directed to and will be fulfilled by the Lead Contact Kornelia Polyak,

Dana-Farber Cancer Institute, 450 Brookline Ave., SM1070B, Boston, MA 02215, USA. E-mail: kornelia_polyak@dfci.harvard.edu.

Materials availability

Materials and reagents can be requested from the lead contact. This paper did not generate unique reagents.

Data and code availability

Raw and processed data generated were deposited to GEO super series GSE273087, bulk RNA-seq (GSE273031), H3K27me3 CUT&Run (GSE273085), scRNA-seq (GSE274140), scATAC-seq (GSE274160), and scMultiomic-seq (GSE274224). For the reanalysis of publicly available datasets, please check the relevant section in the STAR Methods and the key resources table. This study did not generate custom code. Any additional information required to reanalyze the data reported in this paper is available from the lead contact upon request.

ACKNOWLEDGMENTS

We thank members of our laboratories for their critical reading of this manuscript and useful discussions. We thank the Dana-Farber Cancer Institute Translational Immunogenomics Lab and Molecular Biology Core Facility for their outstanding service and the staff of the UPMC Cytogenetics Laboratories for their assistance in ploidy assessments. The authors acknowledge Haley Szewczuga, a Science Writer/Editor at the Dana-Farber Cancer Institute, for her support in the preparation of this manuscript. This research was supported by the National Cancer Institute CA197623 (K.P.), CA250959 (K.P., H.W.L.), CA297044-01 (Z.L.), CA047904 (University of Pittsburgh Organoid Research Core Facility, RRID:SCR_025698 and the UPMC Hillman Cancer Center Cytometry Facility (RRID:SCR_025361), the Canadian Institutes of Health Research (M-A.G.), the Ludwig Center at Harvard (A.G.L, J.A., K.P.), Charles A. King Foundation (Z.L.), Susan G. Komen Foundation SAB220213 (A.V.L.), Belgian American Educational Foundation (P.F.), Wallonie-Bruxelles International (P.F.) and Télévie Foundation (P.F.), FE (P.F.). This project used the UPMC Hillman Cancer Center and Tissue and Research Pathology/Pitt Biospecimen Core shared resource, which is also supported in part by P30CA047904. We would like to dedicate this manuscript to the memory of Angelika Amon, with whom we had many stimulating discussions in the planning phase of this project.

AUTHOR CONTRIBUTIONS

K.P. and P.F. conceived the project and designed experiments. P.F., Z.L., X.C., M.S., D.D.B., A.T., P.B., S.P., and P.Y. performed the experiments. Z.L. performed bioinformatic analysis of scRNA-seq, scATAC-seq and public gene expression data. E.R-J., J.N., T.B., P.Y., M.A.G., X-Y. H., and L.E.S. helped with tissue collection and analyses. X.Q., R.L., Y.J., Y.X., and Y.X. assisted with scATAC-seq data pre-processing. R.K. and B.T.S. performed WGD calling of human PDOs. M.A. performed karyotyping of PDOs. L.M., C.I.S.V., K.E.H., and T. S. analyzed WGD in public expression data. B.D., TJ.S., and I.H. analyzed SMI screen data. P.F., Z.L., and K.P. wrote the manuscript with input from all authors. K.P., A.G.L., P.C., H.W.L., S.O., A.L., C.C., and J.A. supervised the work.

DECLARATION OF INTERESTS

K.P. serves on the Scientific Advisory Board of Ideaya Biosciences and is an adviser to Curie.Bio, holds equity in Antares Therapeutics and stock options in Ideaya Biosciences, receives funding from Novartis, and received honoraria from Astra-Zeneca and Novartis, and payment from Eli Lilly for the purchase of Scorpion Biosciences. T.M.B. is a shareholder of Merck, Eli Lilly, Novo Nordisk, AbbVie, and Johnson&Johnson. **L.E.S.** and **S.P.** are current employees of AstraZeneca. B.D. and **T.J.S.** is current employee of L.E.K. Consulting and ThermoFisher, respectively. P.F. received honoraria from Novartis, conference support from Gilead Oncology and Eli Lilly, and sponsor fees for events organization from Astra-Zeneca, Gilead Oncology, Eli Lilly, Menarini Stemline, Novartis, Pfizer. A.G.L. is the current Director of the National Cancer Institute, USA.

STAR★METHODS

Detailed methods are provided in the online version of this paper and include the following:

- KEY RESOURCES TABLE
- EXPERIMENTAL MODEL AND STUDY PARTICIPANT DETAILS
  - Animals
  - Cell lines
  - Patient-derived organoid culture
- METHOD DETAILS
  - Generation of WGD cell line models
  - Karyotyping
  - Small molecule inhibitor screen
  - Cell growth assay
  - Mouse tumorigenesis assays
  - High Throughput BH3 profiling
  - Immunoblot analyses
  - Immunofluorescence and immunohistochemistry staining
  - Flow cytometry
  - Cytokine array
  - KDM6 and PRC2 enzymatic activity assay
  - Alpha-ketoglutarate and succinate measurement
  - FACETS-based estimation of tumor purity and ploidy from whole-exome sequencing
  - Patient-derived organoid flow cytometry
  - Generation and analyses of scRNA-seq data
  - Generation and analyses of scATAC-seq data
  - RNA-seq data generation and analyses
  - Analyses of public gene expression data
  - H3K27me3 CUT&Run
  - Whole exome sequencing
- QUANTIFICATION AND STATISTICAL ANALYSIS
  - Statistical analyses

SUPPLEMENTAL INFORMATION

Supplemental information can be found online at https://doi.org/10.1016/j.ccell.2026.04.007.

Received: February 10, 2025
Revised: October 26, 2025
Accepted: April 15, 2026

REFERENCES

1. Holland, A.J., and Cleveland, D.W. (2009). Boveri revisited: chromosomal instability, aneuploidy and tumorigenesis. Nat. Rev. Mol. Cell Biol. *10*, 478–487. https://doi.org/10.1038/nrm2718.
2. Gordon, D.J., Resio, B., and Pellman, D. (2012). Causes and consequences of aneuploidy in cancer. Nat. Rev. Genet. *13*, 189–203. https://doi.org/10.1038/nrg3123.
3. Sansregret, L., and Swanton, C. (2017). The Role of Aneuploidy in Cancer Evolution. Cold Spring Harb. Perspect. Med. *7*, a028373. https://doi.org/10.1101/cshperspect.a028373.
4. Kirsch-Volders, M., Mišík, M., and Fenech, M. (2025). Tetraploidy in normal tissues and diseases: mechanisms and consequences. Chromosoma *134*, 3. https://doi.org/10.1007/s00412-025-00829-1.
5. Dewhurst, S.M., McGranahan, N., Burrell, R.A., Rowan, A.J., Grönroos, E., Endesfelder, D., Joshi, T., Mouradov, D., Gibbs, P., Ward, R.L., et al. (2014). Tolerance of whole- genome doubling propagates chromosomal instability and accelerates cancer genome evolution. Cancer Discov. *4*, 175–185. https://doi.org/10.1158/2159-8290.CD-13-0285.
6. Ippolito, M.R., Martis, V., Martin, S., Tijhuis, A.E., Hong, C., Wardenaar, R., Dumont, M., Zerbib, J., Spierings, D.C.J., Fachinetti, D., et al. (2021). Gene copy-number changes and chromosomal instability induced by

aneuploidy confer resistance to chemotherapy. Dev. Cell *56*, 2440–2454.e6. https://doi.org/10.1016/j.devcel.2021.07.006.

7. Vendramin, R., Litchfield, K., and Swanton, C. (2021). Cancer evolution: Darwin and beyond. EMBO J. *40*, e108389. https://doi.org/10.15252/embj.2021108389.
8. Sdeor, E., Okada, H., Saad, R., Ben-Yishay, T., and Ben-David, U. (2024). Aneuploidy as a driver of human cancer. Nat. Genet. *56*, 2014–2026. https://doi.org/10.1038/s41588-024-01916-2.
9. Garrido-Castro, A.C., Lin, N.U., and Polyak, K. (2019). Insights into Molecular Classifications of Triple-Negative Breast Cancer: Improving Patient Selection for Treatment. Cancer Discov. *9*, 176–198. https://doi.org/10.1158/2159-8290.CD-18-1177.
10. Cortes, J., Rugo, H.S., Cescon, D.W., Im, S.A., Yusof, M.M., Gallardo, C., Lipatov, O., Barrios, C.H., Perez-Garcia, J., Iwata, H., et al. (2022). Pembrolizumab plus Chemotherapy in Advanced Triple-Negative Breast Cancer. N. Engl. J. Med. *387*, 217–226. https://doi.org/10.1056/NEJMoa2202809.
11. Bardia, A., Hurvitz, S.A., Tolaney, S.M., Loirat, D., Punie, K., Oliveira, M., Brufsky, A., Sardesai, S.D., Kalinsky, K., Zelnak, A.B., et al. (2021). Sacituzumab Govitecan in Metastatic Triple-Negative Breast Cancer. N. Engl. J. Med. *384*, 1529–1541. https://doi.org/10.1056/NEJMoa2028485.
12. Shu, S., Lin, C.Y., He, H.H., Witwicki, R.M., Tabassum, D.P., Roberts, J.M., Janiszewska, M., Huh, S.J., Liang, Y., Ryan, J., et al. (2016). Response and resistance to BET bromodomain inhibitors in triple-negative breast cancer. Nature *529*, 413–417. https://doi.org/10.1038/nature16508.
13. Alečković, M., Li, Z., Zhou, N., Qiu, X., Lulseged, B., Foidart, P., Huang, X.Y., Garza, K., Shu, S., Kesten, N., et al. (2023). Combination Therapies to Improve the Efficacy of Immunotherapy in Triple-negative Breast Cancer. Mol. Cancer Therapeut. *22*, 1304–1318. https://doi.org/10.1158/1535-7163.MCT-23-0303.
14. Shu, S., Wu, H.J., Ge, J.Y., Zeid, R., Harris, I.S., Jovanović, B., Murphy, K., Wang, B., Qiu, X., Endress, J.E., et al. (2020). Synthetic Lethal and Resistance Interactions with BET Bromodomain Inhibitors in Triple-Negative Breast Cancer. Mol. Cell *78*, 1096–1113.e8. https://doi.org/10.1016/j.molcel.2020.04.027.
15. Ge, J.Y., Shu, S., Kwon, M., Jovanović, B., Murphy, K., Gulvady, A., Fassl, A., Trinh, A., Kuang, Y., Heavey, G.A., et al. (2020). Acquired resistance to combined BET and CDK4/6 inhibition in triple-negative breast cancer. Nat. Commun. *11*, 2350. https://doi.org/10.1038/s41467-020-16170-3.
16. Pfau, S.J., Silberman, R.E., Knouse, K.A., and Amon, A. (2016). Aneuploidy impairs hematopoietic stem cell fitness and is selected against in regenerating tissues in vivo. Genes Dev. *30*, 1395–1408. https://doi.org/10.1101/gad.278820.116.
17. Santaguida, S., Richardson, A., Iyer, D.R., M'Saad, O., Zasadil, L., Knouse, K.A., Wong, Y.L., Rhind, N., Desai, A., and Amon, A. (2017). Chromosome Mis-segregation Generates Cell-Cycle-Arrested Cells with Complex Karyotypes that Are Eliminated by the Immune System. Dev. Cell *41*, 638–651.e5. https://doi.org/10.1016/j.devcel.2017.05.022.
18. Bakhoum, S.F., and Cantley, L.C. (2018). The Multifaceted Role of Chromosomal Instability in Cancer and Its Microenvironment. Cell *174*, 1347–1360. https://doi.org/10.1016/j.cell.2018.08.027.
19. Mackenzie, K.J., Carroll, P., Martin, C.A., Murina, O., Fluteau, A., Simpson, D.J., Olova, N., Sutcliffe, H., Rainger, J.K., Leitch, A., et al. (2017). cGAS surveillance of micronuclei links genome instability to innate immunity. Nature *548*, 461–465. https://doi.org/10.1038/nature23449.
20. Taylor, A.M., Shih, J., Ha, G., Gao, G.F., Zhang, X., Berger, A.C., Schumacher, S.E., Wang, C., Hu, H., Liu, J., et al. (2018). Genomic and Functional Approaches to Understanding Cancer Aneuploidy. Cancer Cell *33*, 676–689.e3. https://doi.org/10.1016/j.ccell.2018.03.007.
21. Davoli, T., Uno, H., Wooten, E.C., and Elledge, S.J. (2017). Tumor aneuploidy correlates with markers of immune evasion and with reduced response to immunotherapy. Science *355*, eaaf8399. https://doi.org/10.1126/science.aaf8399.
22. Cancer Genome Atlas Network (2012). Comprehensive molecular portraits of human breast tumours. Nature *490*, 61–70. https://doi.org/10.1038/nature11412.
23. Quinton, R.J., DiDomizio, A., Vittoria, M.A., Kotýnková, K., Ticas, C.J., Patel, S., Koga, Y., Vakhshoorzadeh, J., Hermance, N., Kuroda, T.S., et al. (2021). Whole-genome doubling confers unique genetic vulnerabilities on tumour cells. Nature *590*, 492–497. https://doi.org/10.1038/s41586-020-03133-3.
24. Senovilla, L., Vitale, I., Martins, I., Tailler, M., Pailleret, C., Michaud, M., Galluzzi, L., Adjemian, S., Kepp, O., Niso-Santano, M., et al. (2012). An immunosurveillance mechanism controls cancer cell ploidy. Science *337*, 1678–1684. https://doi.org/10.1126/science.1224922.
25. Wang, R.W., Viganò, S., Ben-David, U., Amon, A., and Santaguida, S. (2021). Aneuploid senescent cells activate NF-kappaB to promote their immune clearance by NK cells. EMBO Rep. *22*, e52032. https://doi.org/10.15252/embr.202052032.
26. Bielski, C.M., Zehir, A., Penson, A.V., Donoghue, M.T.A., Chatila, W., Armenia, J., Chang, M.T., Schram, A.M., Jonsson, P., Bandlamudi, C., et al. (2018). Genome doubling shapes the evolution and prognosis of advanced cancers. Nat. Genet. *50*, 1189–1195. https://doi.org/10.1038/s41588-018-0165-1.
27. Carter, S.L., Cibulskis, K., Helman, E., McKenna, A., Shen, H., Zack, T., Laird, P.W., Onofrio, R.C., Winckler, W., Weir, B.A., et al. (2012). Absolute quantification of somatic DNA alterations in human cancer. Nat. Biotechnol. *30*, 413–421. https://doi.org/10.1038/nbt.2203.
28. Curtis, C., Shah, S.P., Chin, S.-F., Turashvili, G., Rueda, O.M., Dunning, M.J., Speed, D., Lynch, A.G., Samarajiwa, S., Yuan, Y., et al. (2012). The genomic and transcriptomic architecture of 2,000 breast tumours reveals novel subgroups. Nature *486*, 346–352.
29. Martínez-Jiménez, F., Movasati, A., Brunner, S.R., Nguyen, L., Priestley, P., Cuppen, E., and Van Hoeck, A. (2023). Pan-cancer whole-genome comparison of primary and metastatic solid tumours. Nature *618*, 333–341. https://doi.org/10.1038/s41586-023-06054-z.
30. Rees, M.G., Seashore-Ludlow, B., Cheah, J.H., Adams, D.J., Price, E.V., Gill, S., Javaid, S., Coletti, M.E., Jones, V.L., Bodycombe, N.E., et al. (2016). Correlating chemical sensitivity and basal gene expression reveals mechanism of action. Nat. Chem. Biol. *12*, 109–116. https://doi.org/10.1038/nchembio.1986.
31. Barretina, J., Caponigro, G., Stransky, N., Venkatesan, K., Margolin, A.A., Kim, S., Wilson, C.J., Lehár, J., Kryukov, G.V., Sonkin, D., et al. (2012). The Cancer Cell Line Encyclopedia enables predictive modelling of anticancer drug sensitivity. Nature *483*, 603–607. https://doi.org/10.1038/nature11003.
32. Nakahara, T., Kita, A., Yamanaka, K., Mori, M., Amino, N., Takeuchi, M., Tominaga, F., Hatakeyama, S., Kinoyama, I., Matsuhisa, A., et al. (2007). YM155, a novel small-molecule survivin suppressant, induces regression of established human hormone-refractory prostate tumor xenografts. Cancer Res. *67*, 8014–8021. https://doi.org/10.1158/0008-5472.CAN-07-1343.
33. Ryan, J., and Letai, A. (2013). BH3 profiling in whole cells by fluorimeter or FACS. Methods *61*, 156–164. https://doi.org/10.1016/j.ymeth.2013.04.006.
34. Reschke, R., and Gajewski, T.F. (2022). CXCL9 and CXCL10 bring the heat to tumors. Sci. Immunol. *7*, eabq6509. https://doi.org/10.1126/sciimmunol.abq6509.
35. Chen, Q., Liu, Y., Gao, Y., Zhang, R., Hou, W., Cao, Z., Jiang, Y.Z., Zheng, Y., Shi, L., Ma, D., et al. (2022). A comprehensive genomic and transcriptomic dataset of triple-negative breast cancers. Sci. Data *9*, 587. https://doi.org/10.1038/s41597-022-01681-z.
36. Alshetaiwi, H., Pervolarakis, N., McIntyre, L.L., Ma, D., Nguyen, Q., Rath, J.A., Nee, K., Hernandez, G., Evans, K., Torosian, L., et al. (2020). Defining the emergence of myeloid-derived suppressor cells in breast cancer using single-cell transcriptomics. Sci. Immunol. *5*, eaay6017. https://doi.org/10.1126/sciimmunol.aay6017.

37. Jin, S., Guerrero-Juarez, C.F., Zhang, L., Chang, I., Ramos, R., Kuan, C.H., Myung, P., Plikus, M.V., and Nie, Q. (2021). Inference and analysis of cell-cell communication using CellChat. Nat. Commun. *12*, 1088. https://doi.org/10.1038/s41467-021-21246-9.

38. Ding, K., Chen, F., Priedigkeit, N., Brown, D.D., Weiss, K., Watters, R., Levine, K.M., Heim, T., Li, W., Hooda, J., et al. (2022). Single cell heterogeneity and evolution of breast cancer bone metastasis and organoids reveals therapeutic targets for precision medicine. Ann. Oncol. *33*, 1085–1088. https://doi.org/10.1016/j.annonc.2022.06.005.

39. Andreatta, M., Corria-Osorio, J., Müller, S., Cubas, R., Coukos, G., and Carmona, S.J. (2021). Interpretation of T cell states from single-cell transcriptomics data using reference atlases. Nat. Commun. *12*, 2965. https://doi.org/10.1038/s41467-021-23324-4.

40. Wang, S., Sun, H., Ma, J., Zang, C., Wang, C., Wang, J., Tang, Q., Meyer, C.A., Zhang, Y., and Liu, X.S. (2013). Target analysis by integration of transcriptome and ChIP-seq data with BETA. Nat. Protoc. *8*, 2502–2515. https://doi.org/10.1038/nprot.2013.150.

41. Sundaram, L., Kumar, A., Zatzman, M., Salcedo, A., Ravindra, N., Shams, S., Louie, B.H., Bagdatli, S.T., Myers, M.A., Sarmashghi, S., et al. (2024). Single-cell chromatin accessibility reveals malignant regulatory programs in primary human cancers. Science *385*, eadk9217. https://doi.org/10.1126/science.adk9217.

42. Qi, W., Zhao, K., Gu, J., Huang, Y., Wang, Y., Zhang, H., Zhang, M., Zhang, J., Yu, Z., Li, L., et al. (2017). An allosteric PRC2 inhibitor targeting the H3K27me3 binding pocket of EED. Nat. Chem. Biol. *13*, 381–388. https://doi.org/10.1038/nchembio.2304.

43. Baksh, S.C., and Finley, L.W.S. (2021). Metabolic Coordination of Cell Fate by alpha-Ketoglutarate-Dependent Dioxygenases. Trends Cell Biol. *31*, 24–36. https://doi.org/10.1016/j.tcb.2020.09.010.

44. Vittoria, M.A., Quinton, R.J., and Ganem, N.J. (2023). Whole-genome doubling in tissues and tumors. Trends Genet. *39*, 954–967. https://doi.org/10.1016/j.tig.2023.08.004.

45. Frankell, A.M., Dietzen, M., Al Bakir, M., Lim, E.L., Karasaki, T., Ward, S., Veeriah, S., Colliver, E., Huebner, A., Bunkum, A., et al. (2023). The evolution of lung cancer and impact of subclonal selection in TRACERx. Nature *616*, 525–533. https://doi.org/10.1038/s41586-023-05783-5.

46. Storchová, Z., Breneman, A., Cande, J., Dunn, J., Burbank, K., O'Toole, E., and Pellman, D. (2006). Genome-wide genetic analysis of polyploidy in yeast. Nature *443*, 541–547. https://doi.org/10.1038/nature05178.

47. Govindan, R., Townsend, A.R., Miller, K.D., Mehmi, I., Kuboki, Y., Dumbrava, E.E., Hamilton, E.P., Vuu, I., Rasmussen, E., Mileshkin, L.R., et al. (2021). Trial in progress: A phase 1, multicenter, open-label, dose-exploration and dose-expansion study evaluating the safety, tolerability, pharmacokinetics, and efficacy of AMG650 in subjects with advanced solid tumors. J. Clin. Oncol. *39*, TPS5600. https://doi.org/10.1200/JCO.2021.39.15_suppl.TPS5600.

48. Ippolito, M.R., Zerbib, J., Eliezer, Y., Reuveni, E., Viganò, S., De Feudis, G., Shulman, E.D., Savir Kadmon, A., Slutsky, R., Chang, T., et al. (2024). Increased RNA and Protein Degradation Is Required for Counteracting Transcriptional Burden and Proteotoxic Stress in Human Aneuploid Cells. Cancer Discov. *14*, 2532–2553. https://doi.org/10.1158/2159-8290.CD-23-0309.

49. Veneti, Z., Gkouskou, K.K., and Eliopoulos, A.G. (2017). Polycomb Repressor Complex 2 in Genomic Instability and Cancer. Int. J. Mol. Sci. *18*, 1657. https://doi.org/10.3390/ijms18081657.

50. Tang, M., Gong, M., Liu, X., Zhang, T., Liu, Z., and Song, D. (2025). Recent update on the development of EZH2 inhibitors and degraders for cancer therapy. Eur. J. Med. Chem. *299*, 118106. https://doi.org/10.1016/j.ejmech.2025.118106.

51. McPherson, A., Vázquez-García, I., Myers, M.A., Al-Rawi, D.H., Zatzman, M., Weiner, A.C., Freeman, S., Mohibullah, N., Satas, G., Williams, M.J., et al. (2025). Ongoing genome doubling shapes evolvability and immunity in ovarian cancer. Nature *644*, 1078–1087. https://doi.org/10.1038/s41586-025-09240-3.

52. Prip, F., Lamy, P., Lindskrog, S.V., Strandgaard, T., Nordentoft, I., Birkenkamp-Demtröder, K., Birkbak, N.J., Kristjánsdóttir, N., Kjær, A., Andreasen, T.G., et al. (2025). Comprehensive genomic characterization of early-stage bladder cancer. Nat. Genet. *57*, 115–125. https://doi.org/10.1038/s41588-024-02030-z.

53. Schreiber, R.D., Old, L.J., and Smyth, M.J. (2011). Cancer immunoediting: integrating immunity's roles in cancer suppression and promotion. Science *331*, 1565–1570. https://doi.org/10.1126/science.1203486.

54. Jiang, Y.Z., Ma, D., Suo, C., Shi, J., Xue, M., Hu, X., Xiao, Y., Yu, K.D., Liu, Y.R., Yu, Y., et al. (2019). Genomic and Transcriptomic Landscape of Triple-Negative Breast Cancers: Subtypes and Treatment Strategies. Cancer Cell *35*, 428–440.e5. https://doi.org/10.1016/j.ccell.2019.02.001.

55. Tsherniak, A., Vazquez, F., Montgomery, P.G., Weir, B.A., Kryukov, G., Cowley, G.S., Gill, S., Harrington, W.F., Pantel, S., Krill-Burger, J.M., et al. (2017). Defining a Cancer Dependency Map. Cell *170*, 564–576.e16. https://doi.org/10.1016/j.cell.2017.06.010.

56. Bankhead, P., Loughrey, M.B., Fernández, J.A., Dombrowski, Y., McArt, D.G., Dunne, P.D., McQuaid, S., Gray, R.T., Murray, L.J., Coleman, H.G., et al. (2017). QuPath: Open source software for digital pathology image analysis. Sci. Rep. *7*, 16878. https://doi.org/10.1038/s41598-017-17204-5.

57. Hao, Y., Hao, S., Andersen-Nissen, E., Mauck, W.M., 3rd, Zheng, S., Butler, A., Lee, M.J., Wilk, A.J., Darby, C., Zager, M., et al. (2021). Integrated analysis of multimodal single-cell data. Cell *184*, 3573–3587.e29. https://doi.org/10.1016/j.cell.2021.04.048.

58. Villanueva, R.A.M., and Chen, Z.J. (2019). ggplot2: Elegant Graphics for Data Analysis. Measurement: Interdisciplinary Research and Perspectives *17*, 160–167. https://doi.org/10.1080/15366367.2019.1565254.

59. Aibar, S., González-Blas, C.B., Moerman, T., Huynh-Thu, V.A., Imrichova, H., Hulselmans, G., Rambow, F., Marine, J.C., Geurts, P., Aerts, J., et al. (2017). SCENIC: single-cell regulatory network inference and clustering. Nat. Methods *14*, 1083–1086. https://doi.org/10.1038/nmeth.4463.

60. Stuart, T., Srivastava, A., Madad, S., Lareau, C.A., and Satija, R. (2021). Single-cell chromatin state analysis with Signac. Nat. Methods *18*, 1333–1341. https://doi.org/10.1038/s41592-021-01282-5.

61. Love, M.I., Huber, W., and Anders, S. (2014). Moderated estimation of fold change and dispersion for RNA-seq data with DESeq2. Genome Biol. *15*, 550. https://doi.org/10.1186/s13059-014-0550-8.

62. Gu, Z., Eils, R., and Schlesner, M. (2016). Complex heatmaps reveal patterns and correlations in multidimensional genomic data. Bioinformatics *32*, 2847–2849. https://doi.org/10.1093/bioinformatics/btw313.

63. Hänzelmann, S., Castelo, R., and Guinney, J. (2013). GSVA: gene set variation analysis for microarray and RNA-seq data. BMC Bioinf. *14*, 7. https://doi.org/10.1186/1471-2105-14-7.

64. Dann, E., Henderson, N.C., Teichmann, S.A., Morgan, M.D., and Marioni, J.C. (2022). Differential abundance testing on single-cell data using k-nearest neighbor graphs. Nat. Biotechnol. *40*, 245–253. https://doi.org/10.1038/s41587-021-01033-z.

65. Cornwell, M., Vangala, M., Taing, L., Herbert, Z., Köster, J., Li, B., Sun, H., Li, T., Zhang, J., Qiu, X., et al. (2018). VIPER: Visualization Pipeline for RNA-seq, a Snakemake workflow for efficient and complete RNA-seq analysis. BMC Bioinformatics *19*, 135. https://doi.org/10.1186/s12859-018-2139-9.

66. Robinson, M.D., McCarthy, D.J., and Smyth, G.K. (2010). edgeR: a Bioconductor package for differential expression analysis of digital gene expression data. Bioinformatics *26*, 139–140. https://doi.org/10.1093/bioinformatics/btp616.

67. Yu, G., Wang, L.G., and He, Q.Y. (2015). ChIPseeker: an R/Bioconductor package for ChIP peak annotation, comparison and visualization. Bioinformatics *31*, 2382–2383. https://doi.org/10.1093/bioinformatics/btv145.

68. Welch, R.P., Lee, C., Imbriano, P.M., Patil, S., Weymouth, T.E., Smith, R.A., Scott, L.J., and Sartor, M.A. (2014). ChIP-Enrich: gene set

enrichment testing for ChIP-seq data. Nucleic Acids Res. *42*, e105. https://doi.org/10.1093/nar/gku463.

69. Ewels, P.A., Peltzer, A., Fillinger, S., Patel, H., Alneberg, J., Wilm, A., Garcia, M.U., Di Tommaso, P., and Nahnsen, S. (2020). The nf-core framework for community-curated bioinformatics pipelines. Nat. Biotechnol. *38*, 276–278. https://doi.org/10.1038/s41587-020-0439-x.
70. Bailey, T.L., Johnson, J., Grant, C.E., and Noble, W.S. (2015). The MEME Suite. Nucleic Acids Res. *43*, W39–W49. https://doi.org/10.1093/nar/gkv416.
71. McKenna, A., Hanna, M., Banks, E., Sivachenko, A., Cibulskis, K., Kernytsky, A., Garimella, K., Altshuler, D., Gabriel, S., Daly, M., and DePristo, M.A. (2010). The Genome Analysis Toolkit: a MapReduce framework for analyzing next-generation DNA sequencing data. Genome Res. *20*, 1297–1303. https://doi.org/10.1101/gr.107524.110.
72. Li, H., and Durbin, R. (2010). Fast and accurate long-read alignment with Burrows-Wheeler transform. Bioinformatics *26*, 589–595. https://doi.org/10.1093/bioinformatics/btp698.
73. Li, H., Handsaker, B., Wysoker, A., Fennell, T., Ruan, J., Homer, N., Marth, G., Abecasis, G., and Durbin, R.; 1000 Genome Project Data Processing Subgroup (2009). The Sequence Alignment/Map format and SAMtools. Bioinformatics *25*, 2078–2079. https://doi.org/10.1093/bioinformatics/btp352.
74. Shen, R., and Seshan, V.E. (2016). FACETS: allele-specific copy number and clonal heterogeneity analysis tool for high-throughput DNA sequencing. Nucleic Acids Res. *44*, e131. https://doi.org/10.1093/nar/gkw520.
75. McLaren, W., Gil, L., Hunt, S.E., Riat, H.S., Ritchie, G.R.S., Thormann, A., Flicek, P., and Cunningham, F. (2016). The Ensembl Variant Effect Predictor. Genome Biol. *17*, 122. https://doi.org/10.1186/s13059-016-0974-4.
76. Sachs, N., de Ligt, J., Kopper, O., Gogola, E., Bounova, G., Weeber, F., Balgobind, A.V., Wind, K., Gracanin, A., Begthel, H., et al. (2018). A Living Biobank of Breast Cancer Organoids Captures Disease Heterogeneity. Cell *172*, 373–386.e10. https://doi.org/10.1016/j.cell.2017.11.010.
77. Su, Y., Subedee, A., Bloushtain-Qimron, N., Savova, V., Krzystanek, M., Li, L., Marusyk, A., Tabassum, D.P., Zak, A., Flacker, M.J., et al. (2015). Somatic Cell Fusions Reveal Extensive Heterogeneity in Basal-like Breast Cancer. Cell Rep. *11*, 1549–1563. https://doi.org/10.1016/j.celrep.2015.05.011.
78. Ewels, P., Magnusson, M., Lundin, S., and Käller, M. (2016). MultiQC: summarize analysis results for multiple tools and samples in a single report. Bioinformatics *32*, 3047–3048. https://doi.org/10.1093/bioinformatics/btw354.
79. Cornwell, M., Vangala, M., Taing, L., Herbert, Z., Köster, J., Li, B., Sun, H., Li, T., Zhang, J., Qiu, X., et al. (2018). VIPER: Visualization Pipeline for RNA-seq, a Snakemake workflow for efficient and complete RNA-seq analysis. BMC Bioinf. *19*, 135. https://doi.org/10.1186/s12859-018-2139-9.
80. Pereira, B., Chin, S.F., Rueda, O.M., Vollan, H.K.M., Provenzano, E., Bardwell, H.A., Pugh, M., Jones, L., Russell, R., Sammut, S.J., et al. (2016). The somatic mutation profiles of 2,433 breast cancers refines their genomic and transcriptomic landscapes. Nat. Commun. *7*, 11479. https://doi.org/10.1038/ncomms11479.
81. Patro, R., Duggal, G., Love, M.I., Irizarry, R.A., and Kingsford, C. (2017). Salmon provides fast and bias-aware quantification of transcript expression. Nat. Methods *14*, 417–419. https://doi.org/10.1038/nmeth.4197.
82. Li, Z., McGinn, O., Wu, Y., Bahreini, A., Priedigkeit, N.M., Ding, K., Onkar, S., Lampenfeld, C., Sartorius, C.A., Miller, L., et al. (2022). ESR1 mutant breast cancers show elevated basal cytokeratins and immune activation. Nat. Commun. *13*, 2011. https://doi.org/10.1038/s41467-022-29498-9.
83. DePristo, M.A., Banks, E., Poplin, R., Garimella, K.V., Maguire, J.R., Hartl, C., Philippakis, A.A., del Angel, G., Rivas, M.A., Hanna, M., et al. (2011). A framework for variation discovery and genotyping using next-generation DNA sequencing data. Nat. Genet. *43*, 491–498. https://doi.org/10.1038/ng.806.

Please cite this article in press as: Foidart et al., Whole-genome doubling drives immune evasion by silencing antigen presentation, Cancer Cell (2026), https://doi.org/10.1016/j.ccell.2026.04.007

STAR★METHODS

KEY RESOURCES TABLE

REAGENT or RESOURCE	SOURCE	IDENTIFIER
Antibodies		
Rat monoclonal anti-mouse CD3	Abcam	Cat# ab11089, RRID: AB_2889189
Rabbit monoclonal anti-mouse CD4	Abcam	Cat# ab183685, RRID: AB_2686917
Rabbit monoclonal anti-mouse CD8	Cell Signaling Technology	Cat# 98941 S, RRID: AB_2756376
Invitrogen Goat anti-Rabbit IgG (H + L) Highly Cross-Adsorbed Secondary Antibody, Alexa Fluor™ 488	Thermo Fisher Scientific	Cat# A-11034, RRID: AB_2576217
Invitrogen Goat anti-Rat IgG (H + L) Cross-Adsorbed Secondary Antibody, Alexa Fluor™ 555	Thermo Fisher Scientific	Cat# A-21434, RRID: AB_141733
Invitrogen Goat anti-Rabbit IgG (H + L) Cross-Adsorbed Secondary Antibody, Alexa Fluor™ 647	Thermo Fisher Scientific	Cat# A-21244, RRID: AB_2535812
Invitrogen CD45 Monoclonal Antibody (30-F11), FITC, eBioscience™	Thermo Fisher Scientific	Cat# 11-0451-82, RRID: AB_465050
MHC Class II (I-A/I-E) Monoclonal Antibody (M5/114.15.2), eFluor 450, eBioscience™	Thermo Fisher Scientific	Cat# 48-5321-82, RRID: AB_1272204
PE anti-mouse CD3 Antibody	BioLegend	Cat# 100206, RRID: AB_312663
APC/Cyanine7 anti-mouse CD49b (pan-NK cells)	BioLegend	Cat# 108920, RRID: AB_2561458
Brilliant Violet 650™ anti-mouse CD19 Antibody	BioLegend	Cat# 115541, RRID: AB_11204087
APC/Cyanine7 anti-mouse NK-1.1 Antibody	BioLegend	Cat# 108724, RRID: AB_830871
Brilliant Violet 785™ anti-mouse/human CD45R/B220 Antibody	BioLegend	Cat# 103245, RRID: AB_11218795
Brilliant Violet 605™ anti-mouse CD4 Antibody	BioLegend	Cat# 100547, RRID: AB_11125962
Brilliant Violet 711™ anti-mouse CD8a Antibody	BioLegend	Cat# 100747, RRID: AB_11219594
PerCP/Cyanine5.5 anti-mouse TCR γ/δ Antibody	BioLegend	Cat# 118118, RRID: AB_10612756
PE/Cyanine7 anti-mouse CD69 Antibody	BioLegend	Cat# 104512, RRID: AB_493564
Alexa Fluor® 700 anti-mouse CD25 Antibody	BioLegend	Cat# 102024, RRID: AB_493709
Invitrogen FOXP3 Monoclonal Antibody (FJK-16s), APC, eBioscience™	Thermo Fisher Scientific	Cat# 17-5773-82, RRID: AB_469457
Brilliant Violet 711™ anti-mouse/human CD11b Antibody	BioLegend	Cat# 101241, RRID: AB_11218791
Brilliant Violet 605™ anti-mouse CD11c Antibody	BioLegend	Cat# 117333, RRID: AB_11204262
APC anti-mouse F4/80 Antibody	BioLegend	Cat# 123116, RRID: AB_893481
PerCP/Cyanine5.5 anti-mouse Ly-6C Antibody	BioLegend	Cat# 128012, RRID: AB_1659241
APC/Cyanine7 anti-mouse Ly-6G Antibody	BioLegend	Cat# 127624, RRID: AB_10640819
PE/Cyanine7 anti-mouse CD103 Antibody	Biolegend	Cat# 121426, RRID: AB_2563691
Invitrogen CD317 (BST2, PDCA-1) Monoclonal Antibody (eBio927), PE, eBioscience™	Thermo Fisher Scientific	Cat# 12-3172-81, RRID: AB_763421

(*Continued on next page*)

Please cite this article in press as: Foidart et al., Whole-genome doubling drives immune evasion by silencing antigen presentation, Cancer Cell (2026), https://doi.org/10.1016/j.ccell.2026.04.007

CellPress
OPEN ACCESS

Continued

REAGENT or RESOURCE	SOURCE	IDENTIFIER
Brilliant Violet 650™ anti-mouse CD80 Antibody	BioLegend	Cat# 104731, RRID: AB_11147759
Alexa Fluor® 700 anti-mouse CD86 Antibody	BioLegend	Cat# 105024, RRID: AB_493721
PE anti-mouse β2-microglobulin Antibody	BioLegend	Cat# 154504, RRID: AB_2721340
APC anti-mouse CD326 (Ep-CAM) Antibody	BioLegend	Cat# 118214, RRID: AB_1134102
Brilliant Violet 421™ anti-mouse CD326 (Ep-CAM) Antibody	BioLegend	Cat#118225, RRID: AB_2563983
BD OptiBuild™ RB705 Mouse Anti-Mouse H-2Dd	BD Biosciences	Cat#757005, RRID: AB_3689170
H-2Kk Antibody, anti-mouse, APC	Miltenyi Biotec	Cat# 130-102-346,RRID: AB_2659836
APC anti-human HLA-A/B/C	BioLegend	Cat#311410; RRID: AB_314879
FITC anti-human β2-microglobulin	BioLegend	Cat#316304; RRID: AB_492837
Histone H3K27me3 antibody (pAb)	Active Motif	Cat# 39155, RRID: AB_2561020
Anti-Histone H3 (tri methyl K9) antibody	Abcam	Cat#ab8898, RRID: AB_306848
Anti-Histone H4 (tri methyl K20) antibody	Abcam	Cat#ab9053, RRID: AB_306969
Tri-Methyl-Histone H3 (Lys4) (C42D8)	Cell Signaling Technology	CAT#9751 S, RRID: AB_2616028
Anti-Histone H3 (acetyl K27) antibody - ChIP Grade (ab4729)	Abcam	CAT#4729, RRID: AB_2118291
Tri-Methyl-Histone H3 (Lys27) (C36B11) Rabbit mAb	Cell Signaling Technology	CAT#9733 T, RRID: AB_2616029
Anti-Histone H3 (tri methyl K36) antibody	Abcam	CAT#ab9050, RRID:AB_306966
Anti-BIRC6/APOLLON antibody	Abcam	Cat# ab19609, RRID: AB_ 445012
Anti-KDM6B/JMJD3 antibody	Abcam	Cat# ab38113, RRID:AB_943898
Survivin (71G4B7) Rabbit mAb	Cell Signaling Technology	Cat#2808 S, RRID: AB_2063948
p53 (1C12) Mouse mAb	Cell Signaling Technology	Cat# 2524 T, RRID: AB_331743
Waf1/Cip1/CDKN1A p21 Antibody	Santa Cruz	Cat#sc-6246, RRID: AB_628073
Ezh2 (D2C9) XP® Rabbit mAb	Cell Signaling Technology	Cat#5246, RRID: AB_10694683
UTX/KDM6A (D3Q1I) Rabbit mAb	Cell Signaling Technology	Cat#33510, RRID: AB_2721244
RBAP46 (V415) Antibody	Cell Signaling Technology	Cat#6882, RRID: AB_10830730
Anti-EED Antibody	Millipore Sigma	Cat#09–774, RRID: AB_1587000
Phospho-Stat1 (Tyr701) (58D6) Rabbit mAb	Cell Signaling Technology	Cat#9167 T, RRID: AB_561284
InVivoPlus anti-mouse CD8α Clone YTS 169.4	Bio X Cell	Cat# BP0117, RRID: AB_10950145
InVivoMAb anti-mouse PD-L1 (B7-H1) Clone 10 F.9G2	Bio X Cell	Cat# BE0101, RRID: AB_2927520
Chemicals, peptides, and recombinant proteins		
Delanzomib	Selleckchem	Cat# S1157, CAS# 847499-27-8
ENMD-2076	Selleckchem	Cat# S1181, CAS# 934353-76-1
Ixazomib (MLN2238)	Selleckchem	Cat# S2180, CAS# 1072833-77-2
Prexasertib HCl (LY2606368)	Selleckchem	Cat# S7178, CAS# 1234015-54-3
Rabusertib (LY2603618)	Selleckchem	Cat# S2626, CAS# 911222-45-2
YM155 (Sepantronium Bromide)	Selleckchem	Cat# S1130, CAS# 781661-94-7
EED226	MedChem Express	Cat# HY-101117, CAS# 2083627-02-3
JQ1	Jun Qi (DFCI)	NA
ZEN-3694	Zenith Epigenetics	NA
Selleck Anti-Cancer Compound Library	Selleck Chemicals LLC	Cat# L3000
Advanced DMEM/F-12	Life Technologies	Cat# 12634028
Corning™ Minimum Essential Medium Eagle (Mod.) 1× (MEM) with Glutamine	Thermo Fisher Scientific	Cat# MT10010CV

(*Continued on next page*)

Please cite this article in press as: Foidart et al., Whole-genome doubling drives immune evasion by silencing antigen presentation, Cancer Cell (2026), https://doi.org/10.1016/j.ccell.2026.04.007

Continued

REAGENT or RESOURCE	SOURCE	IDENTIFIER
Corning™ MEM Nonessential Amino Acid Solution	Thermo Fisher Scientific	Cat# MT25025CI
Penicillin-Streptomycin (10,000 U/mL)	Thermo Fisher Scientific	Cat# 15140163
FBS 500ML fetal bovine serum USA origin sterile	Sigma-Aldrich	Cat# 6365/F2442
Gibco™ L-Glutamine (200 mM)	Thermo Fisher Scientific	Cat# 25030164
Amphotericin B	Gibco	Cat# 15290026, CAS# 1397-89-3
DMEM high glucose	Corning	Cat# 10-013-CV
Corning™ Matrigel™ Matrix Basement Membrane	Thermo Fisher Scientific	Cat# 40234 Lot#
Phosphate Buffered Saline (PBS), pH 7,4	VWR	Cat# 392–0442 P
Collagenase type IV	Worthington Biochemical Corporation	Cat# LS004189 CAS# 9001-12-1
Hyaluronidase	Sigma-Aldrich	Cat# H3506 CAS# 37326-33-3
Percoll	Sigma-Aldrich	Cat# P4937
Recombinant human interferon gamma	Sigma-Aldrich	Cat#I17001
Recombinant Mouse IFN-γ (carrier-free)	Biolegend	Cat# 575306
doxorubicin	Sigma-Aldrich	Cta#D1515-10MG
Cytochalasin D	Sigma	Cat#C2618-200UL
Hoechst 33342	Life Technologies	Cat#H3570
Critical commercial assays		
RNeasy Micro Kit	QIAGEN	Cat# 74106
LIVE/DEAD™ Fixable Aqua Dead Cell Stain Kit, for 405 nm excitation	Thermo Fisher Scientific	Cat# L34957
Invitrogen™ eBioscience™ Intracellular Fixation & Permeabilization Buffer Set	Thermo Fisher Scientific	Cat# 88-8824-00
Target Retrieval Solution, Citrate pH 6	Agilent	Cat# S236984-2
Proteome Profiler Mouse XL Cytokine Array	R&D systems	Cat# ARY028
α-Ketoglutarate Assay Kit	Sigma-Aldrich	Cat# MAK054
Succinate Colorimetric Assay Kit	Sigma-Aldrich	Cat# MAK184
α-Ketoglutarate Assay Kit	Abcam	Cat# Ab83431
Succinate Assay Kit	Abcam	Cat# Ab204718
SF Cell Line 4D-Nucleofector X Kit S	Lonza	Cat# V4XC-1032
Chromium Next GEM Single Cell 5′ HT Kit v2	10× Genomics	PN: 1000356
Chromium Next GEM Single Cell ATAC Kit v2	10× Genomics	PN: 1000406
KDM6A/KDM6B Activity Quantification Assay Kit (Colorimetric) (48 tests)	Abcam	Cat# ab156910
EZH2 Chemiluminescent Assay Kit	BPS BioScience	Cat#52009L
VECTASTAIN Elite ABC Kit	Vector Laboratories	Cat#PK-6101
ImmPACT DAB substrate kit	Vector Laboratories	Cat#SK-4105
Deposited data		
scRNA-seq	This study	GSE274140
scATAC-seq	This study	GSE274160
bulk-RNA-seq	This study	GSE273031
H3K27me3 CUT&RUN data	This study	GSE273085
scMultiomic-seq	This study	GSE274224
TCGA scATAC-seq and bulk RNA-seq	dbGaP[41]	phs000178.v11.p8
METABRIC microarray	Synapse[28]	Syn1688369
FUSCC bulk RNA-seq	Jiang et al.[54]	NODE: OEP000155

(*Continued on next page*)

Please cite this article in press as: Foidart et al., Whole-genome doubling drives immune evasion by silencing antigen presentation, Cancer Cell (2026), https://doi.org/10.1016/j.ccell.2026.04.007

Continued

REAGENT or RESOURCE	SOURCE	IDENTIFIER
Paired bone metastases scRNA-seq	Ding et al.[38]	GSE190772
Breast cancer cell line CRISPR screen (22Q4)	DepMap[55]	https://depmap.org/portal/data_page/?tab=allData
Breast cancer cell line YM-155 PRISM screen	DepMap[30]	https://depmap.org/portal/data_page/?tab=allData
Experimental models: Cell lines		
TA3 Hauschka	Sigma-Aldrich	cat# 85061102-1VL, RRID:CVCL_4321
67NR	Karmanos Institute	RRID:CVCL_9723
168FARN	Karmanos Institute	RRID:CVCL_0I86
Patient-derived organoid LIO-046 R	U. Pittsburgh Organoid Research Core Facility	RRID:SCR_025698
Patient-derived organoid IPM-BO-056	U. Pittsburgh Organoid Research Core Facility	RRID:SCR_025698
Patient-derived organoid LIO-083 R	U. Pittsburgh Organoid Research Core Facility	RRID:SCR_025698
Patient-derived organoid LIO-083 L	U. Pittsburgh Organoid Research Core Facility	RRID:SCR_025698
Patient-derived organoid IPM-BO-108	U. Pittsburgh Organoid Research Core Facility	RRID:SCR_025698
Patient-derived organoid IPM-BO-111	U. Pittsburgh Organoid Research Core Facility	RRID:SCR_025698
Patient-derived organoid IPM-BO-153	U. Pittsburgh Organoid Research Core Facility	RRID:SCR_025698
Patient-derived organoid IPM-BO-194	U. Pittsburgh Organoid Research Core Facility	RRID:SCR_025698
Patient-derived organoid IPM-BO-197	U. Pittsburgh Organoid Research Core Facility	RRID:SCR_025698
Patient-derived organoid IPM-BO-230	U. Pittsburgh Organoid Research Core Facility	RRID:SCR_025698
Experimental models: Organisms/strains		
NOD.Cg-Prkdc^{scid}Il2rg^{tm1Wjl}Tg(CMV-IL3.CSF2.KITLG)1Eav/MloySzJ mice	Jackson Laboratory	RRID:IMSR_JAX:013062
A/J strain mice	Jackson Laboratory	RRID:IMSR_JAX:000646
NOD/MrkBomTac-Prkdc^{scid} mice	Taconic	RRID:IMSR_TAC:NODSC
BALB/cJ strain mice	Jackson Laboratory	RRID:IMSR_JAX: 000651
Oligonucleotides		
guide RNA for scramble	GCTTAGTTACGCGTGGACGA	
guide RNA for B2m	TGAGTATACTTGAATTTGAG	
ON-TARGETplus Non-targeting control siRNA (5nmol)	Horizon Discovery	D-001810-10-05
ON-TARGETplus Mouse Trp53 siRNA (5nmol)	Horizon Discovery	L-040642-00-0005
ON-TARGETplus Mouse Birc5 siRNA (5nmol)	Horizon Discovery	L-043690-00-0005
ON-TARGETplus Mouse Birc6 siRNA (5nmol)	Horizon Discovery	L-043121-00-0005
Recombinant DNA		
EF1a_mcherry_P2A_Hygro	Addgene	Cat#135003, RRID: addgene 135003
pLV[Exp]-Puro-CMV>TagBFP	Vector Builder	Cat# VB190326-1269umq, custom order
Software and algorithms		
QuPath (version: 0.4.0)	Bankhead et al.[56]	https://qupath.readthedocs.io/en/0.4/index.html

(*Continued on next page*)

Please cite this article in press as: Foidart et al., Whole-genome doubling drives immune evasion by silencing antigen presentation, Cancer Cell (2026), https://doi.org/10.1016/j.ccell.2026.04.007

Continued

REAGENT or RESOURCE	SOURCE	IDENTIFIER
GraphPadPrism (version: 10.0.3)	GraphPad Software Inc.	https://www.graphpad.com/updates/prism-900-release-notes
FlowJo (version: 10.8.2)	FlowJo, LLC	https://www.flowjo.com/
Cell Ranger (version: 7.0.1)	10× Genomics	https://support.10xgenomics.com/single-cell-gene-expression/software/pipelines/latest/what-is-cell-ranger
Cell Ranger-ATAC (version 2.0.0)	10× Genomics	https://software.10xgenomics.com/single-cell-atac/software/pipelines/2.0/what-is-cell-ranger-atac
Cell Ranger ARC (version 2.0.0)	10× Genomics	https://www.10xgenomics.com/support/software/cell-ranger-arc
Seurat (version: 5.0.2)	Hao et al.[57]	https://satijalab.org/seurat/
ggplot2 (version: 3.5.0)	Randle Aaron et al.[58]	https://ggplot2.tidyverse.org
SCENIC (version: 1.3.1)	Aibar et al.[59]	https://scenic.aertslab.org
Signac (version: 1.13.0)	Stuart et al.[60]	https://stuartlab.org/signac/index.html
CellChat (version 1.6.1)	Jin et al.[37]	https://github.com/sqjin/CellChat
DESeq2 (version 1.42.1)	Love et al.[61]	http://www.bioconductor.org/packages/release/bioc/html/DESeq2.html
QuickATAC	Unpublished	https://github.com/AllenWLynch/QuickATAC
ComplexHeatmap (version 2.18.0)	Gu et al.[62]	https://bioconductor.org/packages/release/bioc/html/ComplexHeatmap.html
GSVA (version 1.50.1)	Hänzelmann et al.[63]	https://www.bioconductor.org/packages/release/bioc/html/GSVA.html
miloR (version 1.10.0)	Dann et al.[64]	https://github.com/MarioniLab/miloR
scCustomize (version 2.1.2)	NA	https://samuel-marsh.github.io/scCustomize/
VIPER	Cornwell et al.[65]	https://bitbucket.org/cfce/viper/src/master/
edgeR (version 4.0.16)	Robinson et al.[66]	https://bioconductor.org/packages/release/bioc/html/edgeR.html
Chipseeker (version 1.38.0)	Yu et al.[67]	https://www.bioconductor.org/packages/release/bioc/html/ChIPseeker.html
chipenrich (vesion 3.20)	Welch et al.[68]	https://www.bioconductor.org/packages/release/bioc/html/chipenrich.html
cutandrun (version 3.2.2)	Ewels et al.[69]	https://github.com/nf-core/cutandrun
MEME Suite (version 5.5.7)	Bailey et al.[70]	https://meme-suite.org/meme/
The Genome Analysis Toolkit (version 4)	McKenna et al.[71]	https://gatk.broadinstitute.org/hc/en-us/sections/360007226651-Best-Practices-Workflows
BETA	Wang et al.[40]	http://cistrome.org/BETA/
FastQC (version 0.11.7)	NA	https://github.com/s-andrews/FastQC
Trim Galore (version 0.6.10)	NA	https://github.com/FelixKrueger/TrimGalore
Burrows–Wheeler Aligner (version 0.7.17)	Li et al.[72]	https://github.com/lh3/bwa
SAMtools (version 1.9)	Li et al.[73]	https://github.com/samtools/samtools
FACETS (version 0.6.2)	Shen et al.[74]	https://github.com/mskcc/facets
Ensembl Variant Effect Predictor (version 115.2)	McLaren et al.[75]	https://github.com/Ensembl/ensembl-vep
ProjeTILs (version 3.5.0)	Andreatta et al.[39]	https://github.com/carmonalab/ProjecTILs

Please cite this article in press as: Foidart et al., Whole-genome doubling drives immune evasion by silencing antigen presentation, Cancer Cell (2026), https://doi.org/10.1016/j.ccell.2026.04.007

CellPress
OPEN ACCESS

EXPERIMENTAL MODEL AND STUDY PARTICIPANT DETAILS

Animals

All animal experiments were performed following protocol #11–023 approved by DFCI IACUC. Exponentially growing cells were resuspended in ice-cold DMEM/F12 and 50% Matrigel (BD Biosciences) and bilaterally and orthotopically injected into the inguinal mammary fat pads of 6-week-old female NOD.Cg-Prkdc^{scid}Il2rg^{tm1Wjl}Tg(CMV-IL3.CSF2.KITLG)1Eav/MloySzJ (Jackson Laboratory, RRID:IMSR_JAX:013062), NOD/MrkBomTac-Prkdc^{scid} (Taconic, RRID:IMSR_TAC:NODSC), A/J (Jackson Laboratory, RRID:IMSR_JAX:000646), or Balbc Jackson Laboratory, RRID:IMSR_JAX:000651) mice.

Cell lines

The TA3 Hauschka cell line was purchased from Sigma (cat# 85061102-1VL, RRID:CVCL_4321), while 67NR (RRID:CVCL_9723) and 168FARN (RRID:CVCL_0I86) cell lines were provided by Karmanos Cancer Institute. Cells were maintained in media recommended by the provider as follow: TA3 cells were cultured in MEM medium including 2mM L-glutamine (Thermo Fisher), 10% FBS, 1% Non-essential Amino Acid (Thermo Fisher) and 1× Penicillin-Streptomycin (Thermo Fisher); 67NR and 168FARN cells were cultured in DMEM with 10% FBS, 2mM L-glutamine, 1% Non-essential Amino Acid (Thermo Fisher) and 1× Penicillin-Streptomycin (Thermo Fisher). All the cells have been tested for mycoplasma and rodent pathogens.

Patient-derived organoid culture

Patient-derived organoids (PDOs) were generated in the Institute for Precision Medicine from primary human breast cancer tissue from the Pitt Biospecimen Core consented and collected in accordance with Institutional Review Board protocol STUDY22030183 as previously described,[76] with the addition of β-estradiol to the medium. Briefly, tumors were digested with 2mg/mL collagenase (Sigma C9407) on a rotator, sheared, filtered, and embedded in Cultrex RGF Basement Membrane Extract (R&D Systems 353301002) in 24-well Nunc non-treated plates (Fisher 12-566-82). Media replaced every 2–3 days and PDOs passaged every 2–4 weeks.

METHOD DETAILS

Generation of WGD cell line models

To set up an experimental model of WGD, we first generated derivates of the cell lines resistant to puromycin or hygromycin by infecting them with lentiviral vectors accordingly. Puromycin resistant vector was synthesized by VectorBuilder (VB190326-1269umq) with pLV backbone and hygromycin resistant vector was obatined from Addgene (EF1a_mCherry_P2A_Hygro, #135003, RRID:Addgene_135003). Lentivirus were packaged in HEK293FT cells using the PAX2 packaging plasmid (Addgene plasmid, #35002, RRID:Addgene_35002), pMD2.G envelope plasmid (Addgene plasmid, #12259, RRID:Addgene_12259), and Lipofectamine 3000 transfection reagent (Life Technologies, #L3000015). The virus was collected 48 h after transfection and infect cells accordingly. Somatic cell fusions were generated using polyethylene glycol essentially as described.[77] Briefly, 4×10^6 cells from each of the drug-resistant derivate were mixed and incubated in 50% PEG-1450 (Sigma #P7181–5X5ML) DMEM mix for 1 min, followed by centrifugation and plating into 150 cm plates in fresh medium containing both puromycin and hygromycin to select for fusion cells.

To create a cytokinesis failure model of WGD, TA3 cells were treated with 0.2 μM cytochalasin D (CytoD) for 16 h and then allowed to recover in drug-free medium for 24 h. Cells were stained in the plate with 20 μg/mL Hoechst 33342 for 30 min at 37°C in the incubator, then detached with trypsin and sorted by DNA content on a BD FACSymphony S6 UV cell sorter. The 8 N fraction was collected and cultured for one week, followed by a second sort to re-enrich 8 N cells. After four rounds of 8 N enrichment, cells were infected with the same lentivirus used to generate TA3 fusion cells and subsequently subjected to four additional DNA-content–based FACS to enrich WGD+ cells. In parallel, WGD- TA3 cells were maintained *in vitro* and infected with the same lentivirus to ensure matched passage numbers.

To generate control and *B2m* knockout cells lines we used CRISPR/Cas9-mediated genome editing and Amaxa 4D-Nucleofector X Unit device (Lonza). Briefly, 2.5μL 200μM trRNA, 2.5μL 200μM gRNA and 5μL 20μM recombinant CAS9 (Integrated DNA Technologies) were mixed to make Cas9/gRNA ribonucleoprotein (RNP). The RNP was delivered into tumor cell lines using program A549 by SF Cell Line 4D-NucleofectorTM X Kit S (Lonza). 200,000 cells were used per reaction and recovered in 12-well plate for 4 days after nucleofection and then subjected to a 2nd round of the same process. Sequence of the gRNAs used: Scramble - GCTTAGTTACGCGTGGACGA, *B2m* - TGAGTATACTTGAATTTGAG.

Karyotyping

Karyotyping of parental and fusion cell lines was performed by the Molecular Cytogenetics Core, Memorial Sloan Kettering Cancer Center, New York, NY. Karyotyping of human PDOs was performed by the UPMC Cytogenetics Laboratories, Pittsburgh, PA.

Small molecule inhibitor screen

Multidrop combi dispenser was used and (Thermo Scientific, cat#05616) WGD+ or WGD- TA3 cells were seeded in 30 μL volume at a density of 150 cells/well in 384 well plates and left to adhere for 12 h.

Please cite this article in press as: Foidart et al., Whole-genome doubling drives immune evasion by silencing antigen presentation, Cancer Cell (2026), https://doi.org/10.1016/j.ccell.2026.04.007

A robotic platform (Sonic Compound Transfer Robot) was then used to conduct a pin transfer of 100 nL from 96-well compound storage plates from the Ludwig Selleck anti-cancer Library (Selleck Chemicals LLC) into the 384 well assay plates using stainless steel pin arrays (V&P Scientific). A total of 386 different drugs (Ludwig Anti-cancer panel) were pinned at 9 different concentrations (initial concentration in storage plate from 10 mM to 2 μM in DMSO) and compared to DMSO treatment put at same volume. The whole screen was performed on both WGD+ and WGD- TA3 cells in duplicate. Compound information is listed in Table S3. After the transfer of drugs, Cells were left for 72 h at 37°C with 5% CO2. Then, cells were stained with Hoechst 33342 and counted with confocal microscopy (ImageXpress Micro Confocal, RRID:SCR_020294). Data were then normalized to DMSO. The area under the viability curve for treatment response (AUC) was calculated for each drug.

Cell growth assay

Confirmation for the drug of interests revealed by the screen was performed in 96 well plates. YM155 (S1130), ENMD-2076 (S1181), Prexasertib (S7178), Rabusertib (S2626), Delanzomib (S1157) and Ixazomib (S2180) were from SelleckChem. WGD+ or WGD- TA3 cells were seeded in 100 μL volume at a density of 1000 cells/well and left to adhere for 12 h. Cells were cultured at 37°C with 5% CO2. Drugs or DMSO were then added at 9 different concentrations in triplicates in 100 μL. After the transfer of drugs, Cells were left for 72 h at 37°C with 5% CO2. Then, cells were stained with Hoechst 33342 and viables cells were counted with the Celigo system (Nexcelom, Celigo Image Cytometer, RRID:SCR_018808). Data were then normalized to DMSO, and drug-curve responses were calculated for each drug.

For colony formation assay, cells were seeded in 6-well plates at a density of 5,000 cells per well in biological triplicates. For siRNA-mediated knockdown experiments, reverse transfection was performed on day 0 using 0.0625 nmol siRNA per well with Lipofectamine RNAiMAX Reagent. A second transfection was carried out on day 6 to maintain knockdown efficiency. On day 12, cells were fixed in ice-cold methanol for 10 min and stained with 0.5% crystal violet solution at room temperature for 15 min. After three washes with double-distilled water (ddH_2O), plates were imaged. For quantification, the crystal violet stain was solubilized in 300 μL of 10% SDS per well, and 100 μL of the resulting solution was transferred to a 96-well plate for absorbance measurement at 450 nm using a microplate reader, with three technical replicates/condition.

Mouse tumorigenesis assays

For anti-CD8 and anti-PDL1 treatment, InVivoPlus anti-mouse CD8α (Clone: YTS 169.4, RRID:AB_10950145) and InVivoMAb anti-mouse PD-L1 (B7-H1, Clone: 10 F.9G2, RRID:AB_2927520) blocking antibodies were purchased from Bio X Cell and dissolved in inVivoPure pH 7.0 (anti-CD8) and 6.5 (anti-PDL1) Dilution Buffer respectively. Isotype and blocking antibodies were given to mice via intraperitoneal injection with 10mg/kg dose following the timeline schema shown in Figure 3E. For EED226 treatment, mice were treated twice daily with either vehicle (0.5% hydroxypropyl methylcellulose, 0.5% Tween 20 in saline) or EED226 (MedChem Express, HY-101117, 10mg/mL) per oral starting 2 days before MFP injection of tumor cells. Tumor cells were treated with vehicle (0.1% DMSO in water) or EED226 (2 μM) 2 days before injection. Tumor growths were monitored every two days and tumor volumes were calculated by shortest diameter X shortest diameter X longest diameter/2. In most of the experiments, endpoint tumor weights also measured as an independent measurement for tumor growth, since it may suggest additional information besides volumes such as necrosis and immune infiltration. Mice were euthanized upon reaching the humane endpoint and tumors were collected at designed time point (i.e., days 8 and 14) according to the specific experimental design.

High Throughput BH3 profiling

High Throughput BH3 profiling was conducted as previously described,[33] to determine the apoptotic priming and anti-apoptotic dependencies of TA3 WGD- and WGD+ cells under 330nM of YM-155 treatment for 24 h 330nM is the IC20 concentration of TA3 WGD+ cells. In brief, cell lines were seeded at a density of 500–2000 cells/well in 384 well plates and left to adhere for 24 h. Then cells were washed 3 times with PBS using the BioTek 406EL plate washer (BioTek). Consequently, different BH3 peptides and BH3 mimetics at different concentrations were added via pin transfer, and cells were incubated in BH3 profiling buffer containing 0.002% digitonin for 1 h. Cells were fixed in paraformaldehyde for 15 min. Afterward, the fixative was neutralized using a tris/glycine buffer. Cells were stained overnight with Hoechst33342 (Nuclei, Invitrogen) and anti-cytochrome c-Alexa Fluor 647 antibody (BioLegend). Prior to imaging, the stain solution was washed out using the BioTek 406EL plate washer. Fluorescent microscope images from the BH3 profiling plates were acquired using the IXM XLS high content widefield microscope (Molecular Devices) at the ICCB Longwood Screening Facility. The cytochrome *c* positive cells were quantified using the Multi-Wavelength Cell Scoring module in Metamorph software. Release of cytochrome *c* in response to the BIM and PUMA peptides indicate overall mitochondrial priming. In contrast, the release of cytochrome *c* in response to the BAD, HRK, MS1, FS1 peptides, and BH3 mimetics indicate specific anti-apoptotic dependencies. Combinations of BH3 mimetics were used to test co-dependencies. Release of cytochrome *c* in response to the BAD peptide and ABT-263 indicate BCL-2, BCL-XL, or Bcl-w dependency; to the HRK peptide, A-133, and A-115 indicate BCL-XL dependency; to ABT-199 indicates BCL-2 dependency; to the MS1 peptide and S63845 indicate MCL-1 dependency.

Immunoblot analyses

Proteins were isolated using isolation buffer (1 mM EGTA, 1 mM EDTA, 150 mM NaCl, 20 mM Tris and 1% Triton X-) for 30 min on ice. Histones were isolated using EpiQuik Total Histone Extraction Kit (Epigentek). Protein concentration was measured using Pierce 660nm Protein Assay Reagent (Thermo Fisher) and equal amounts were loaded onto 4–12% Bis-Tris gradient gel (for survivin) or

Please cite this article in press as: Foidart et al., Whole-genome doubling drives immune evasion by silencing antigen presentation, Cancer Cell (2026), https://doi.org/10.1016/j.ccell.2026.04.007

Tris- 10% Tricine (histone extracts) gels. Proteins were transferred onto PVDF membranes using wet blot devices and 1× transfer buffer containing 20% methanol for at 90 V for 2 h. Membranes were incubated with primary antibodies against Survivin (Cell Signaling Technology, 2808 1:1000, RRID:AB_2063948), beta-2 microglobolin (Life Technology, 701250, 1:1000, RRID:AB_2532441), tubulin (Millipore, T6199, 1:20000, RRID:AB_477583), H3K27me3 (Active Motif, 39155, 1:1000, RRID:AB_2561020), H3K27ac (abcam, ab4729, 1:1000, RRID:AB_2118291), H3K4me3 (Cell Signaling Technology, 9751, 1:1000, RRID:AB_2616028), H3K9me3 (abcam, ab8898, 1:1000, RRID:AB_306848) and H4K20me3 (abcam, ab9053, 1:1000, RRID:AB_306969) in 5% milk overnight and with secondary antibodies anti-ms HRP (Invitrogen, 62–6520, 1:10000, RRID:AB_2533947) or anti-rb HRP (Invitrogen, 65–6120, 1:10000, RRID:AB_88384) in TBST for 1 h. Signals were developed with Clarity Western ECL Solution (BioRad) on a Chemidoc MP (BioRad) device. For loading controls of histone, histone extracts were run on a 10% tricine gel and stained with InstantBlue Coomassie Protein Stain blue (abcam, ab119211) for 20 min.

Immunofluorescence and immunohistochemistry staining

Tissue FFPE sections were deparaffinized and antigen retrieval was performed using Target Retrieval Solution, pH 6 (Agilent) for 40 min with a steamer. Slides were then blocked using 5% NGS in TBST for one hour and incubated with primary antibodies against CD3 (Abcam, ab11089, 1:100, RRID:AB_2889189), CD4 (Abcam, ab183685, 1:100, RRID:AB_2686917), CD8 (Cell Signaling Technology, #98941, 1:100, RRID:AB_2756376) and H3K27me3 (Cell Signaling Technology, #9733, 1:100, RRID:AB_2616029) in 5% NGS in TBST overnight in 4° and secondary antibodies (goat anti rb Alexa Fluor 647 (Invitrogen, A-21245, RRID:AB_2535813) and goat anti rb Alexa Fluor 555 (Invitrogen, A-21428, RRID:AB_141784) in 5% NGS in TBST for 2 h in room temperature. Endogenous fluorescence was quenched using TrueVIEW Autofluorescence Quenching Kit (Vector Laboratories) for 5 min.

For immunohistochemistry staining, heat-induced antigen retrieval was carried out by placing sections in 10 mM sodium citrate buffer (pH 6.0) at 95°C for 20 min. Endogenous peroxidase activity was quenched by treating sections with 0.3% H2O2 for 30 min. Sections were then blocked for 30 min at room temperature using serum from the species in which the secondary antibody was raised, followed by overnight incubation with primary antibodies at 4°C. On the following day, sections were incubated with components from the VECTASTAIN Elite ABC Kit (Vector Laboratories, #PK-6101). The HRP signal was visualized by incubating sections with a DAB substrate.

For all the experiments, images were taken with a Nikon ECLIPSE Ti2-E fluorescence microscope and QuPath software (RRID:SCR_018257) was used for image analysis and target protein quantification. For H3K27me3 quantification, nuclei H3K27me3 signal intensity was normalized to the cytoplasmic signal for background correction in each cell.

Flow cytometry

Tumor tissues were smashed and digested for 60 min using digestion media (2% w/v collagenase IV, 2% w/v hyaluronidase and 2% w/v BSA in DMEM) at 37°C in shaker for 1 h. Cell suspensions were filtered through a 500 μm mesh, washed with PBS and frozen in 10% DMSO/FBS at −80°C. For flow cytometry analysis, digested cells were first stained with Live/dead cell staining kit (Life Technology, L34957) and fixed using eBioscience Intracellular Fixation & Permeabilization Buffer (Thermo Fisher, 88-8824-00). Cells were then stained by two antibody panels (1:200) against lymphocyte and myeloid cell markers separately. The lymphocyte panel is a mixture of the following antibodies: CD45-FITC (eBioscience, 11-0451-82, RRID:AB_465050), MHC-II-eFluor450 (eBioscience, 48-5321-82, RRID:AB_1272204), CD3e-PE (BioLegend, 100206, RRID:AB_312663), CD49b-APC-Cy7 (BioLegend, 108920, RRID:AB_2561458), CD19-BV650 (BioLegend, 115541, RRID:AB_11204087), NK1.1-APC-Cy7(BioLegend, 108724, RRID:AB_830871), CD4-BV605 (BioLegend, 100547, RRID:AB_11125962), CD8a-BV711 (BioLegend, 100747, RRID:AB_11219594), γδTCR-PerCP-Cy5.5 (BioLegend, 118118, RRID:AB_10612756), CD69-PE/Cyanine7 (BioLegend, 104512, RRID:AB_493564), CD25-Alexa Fluor 700 (BioLegend, 102024, RRID:AB_493709) and FoxP3-APC (eBioscience, 17-5773-82, RRID:AB_469457). The myeloid marker panel includes CD11b-BV711 (BioLegend, 101241, RRID:AB_11218791), CD11c-BV605 (BioLegend, 117333, RRID:AB_11204262), F4-80-APC (BioLegend, 123116, RRID:AB_893481), Ly6C-PerCP-Cy5.5 (BioLegend, 128012, RRID:AB_1659241), Ly6G-APC-Cy7 (BioLegend, 127624, RRID:AB_10640819), CD103-PE/Cyanine7 (BioLegend, 121426, RRID:AB_2563691), PDCA-1-PE (eBioscience, 12-3172-81, RRID:AB_763421), CD80-BV650 (BioLegend, 104731, RRID:AB_11147759), CD86-Alexa Fluor 700 (BioLegend, 105024, RRID:AB_493721) as well as the CD45-FITC and MHC-II-eFluor450 listed above. Flow cytometry was performed using LSRFortessa High-Parameter Flow Cytometer (BD, RRID:SCR_025285) after channel compensation. Gating strategies are shown in Figures S4D–S4F.

For *in vitro* IFNγ treatment experiments, cells were treated with different doses of murine IFNγ (0, 0.05, 0.1, 0.2, 0.5, or 1 ng/mL) for 16 h and stained with Live/dead cell staining kit (Life Technology, L34957) and PE anti-mouse β2-microglobulin (Biolegend, 154504, RRID:AB_2721340) and fixed with 2% PFA for 10 min. Flow cytometry for MHC makers was performed 24 h later.

Cytokine array

Snap-frozen tumor tissue was mechanically homogenized in 1% Triton X- in PBS with protease and phosphorate inhibitors and subject to one freeze-thaw cycles. Supernatant was collected after centrifuge. For each experimental condition protein concentration in supernatant from each individual tumor was determined using Pierce BCA Protein Assay Reagent (Thermo Fisher) and then 200μg protein evenly mixed from each sample from the sample group was used for cytokine quantification. Cytokine levels were determined with Proteome Profiler Mouse XL Cytokine Array (R&D Systems) on a Chemidoc MP (BioRad) device following manufacturer protocol. ImageJ was used for protein amount quantification.

Please cite this article in press as: Foidart et al., Whole-genome doubling drives immune evasion by silencing antigen presentation, Cancer Cell (2026), https://doi.org/10.1016/j.ccell.2026.04.007

KDM6 and PRC2 enzymatic activity assay

ELISA assays were conducted following the manufacture protocol using either KDM6A/B (Abcam, ab156910) or PRC2 (BPS BioScience, #52009) activity kits. Briefly, 10-20mg snap-frozen tumor tissue was mechanically homogenized in 150μL 1% Triton X- in PBS with protease and phosphorate inhibitors and subject to one freeze-thaw cycle. Supernatant was collected after centrifuge. 20 μL tumor lysates from were used for ELISA input and the OD450 values were normalized to input tumor weight as normalized RLU.

Alpha-ketoglutarate and succinate measurement

Snap frozen tumor tissues (10-20mg) were homogenized and lysed in 150μL PBS+1% Triton X-100 with protease inhibitors. After one freeze-thaw cycle, 20 μL tumor lysate was used for the relevant assays. For metabolites measurement in TA3 tumor of Figure 7Q, alpha ketoglutarate kit (Sigma-Aldrich MAK054) and succinate kit (Sigma-Aldrich MAK184) were used, and metabolite abundance were determined by fluorescent and colorimetric assays respectively. For metabolites measurement in 168fARN and TA3 cytokinesis failure models conducted later, alpha ketoglutarate kit (Abcam, ab83431) and succinate kit (Abcam 204718) were used due to the discontinuation of the Sigma-Aldrich kits, and metabolite abundance were determined by colorimetric assays following the manufactural protocol and raw readouts were further normalized to the initial tissue amount for each metabolite.

FACETS-based estimation of tumor purity and ploidy from whole-exome sequencing

Genomic DNA was extracted from patient-derived organoids (PDOs) and matched peripheral blood samples using DNeasy Blood & Tissue Kits by Qiagen. Samples were submitted to the UPMC Genome Center (UGC) for whole-exome sequencing (WES) library preparation and paired-end sequencing using the Roche KAPA HyperPlus Kit (Cat. #09075810001). For each sample, 500 ng of genomic DNA was enzymatically fragmented, followed by end repair, A-tailing, adapter ligation, and PCR amplification. Library quality was assessed using AATI Fragment Analyzer. Targeted exonic regions were captured using the IDT xGen Exome Research Panel v1.0 (Cat. #1056114) with xGen Universal Blockers (Cat. #1075474), following the Roche KAPA HyperCap Workflow v3.0, per the manufacturer's protocol. Prepared libraries, with an average insert size of approximately 400 bp, were quantified using the KAPA qPCR quantification kit (Roche) on a LightCycler 480 (Roche). Libraries were normalized and pooled according to Illumina guidelines. Sequencing was performed on the Illumina NovaSeq 6000 platform, generating 151 bp paired end reads. Raw base call (BCL) files generated on the NovaSeq 6000 were converted to sample-level FASTQ files using Illumina's bcl2fastq conversion software (v3.0.3–v0.11.9). Average sequencing depth ranged from 20× to 318× for PDO samples and from 51× to 97× for matched blood samples.

Bioinformatics analysis began with preprocessing of paired-end raw reads (*.fastq.gz) using FastQC (https://github.com/s-andrews/FastQC) (v0.11.7) for quality assessment, Trim Galore (https://github.com/FelixKrueger/TrimGalore) (v 0.6.10) for adapter and low-quality base trimming, and MultiQC (v1.19)[78] for summarizing quality control metrics. Reads with low quality score and adapter sequences were removed. High-quality reads were then aligned to the human reference genome (hg38) using the Burrows–Wheeler Aligner (BWA-MEM[72] v0.7.17). Aligned reads were sorted and indexed using SAMtools[73] (v1.9). The resulting sorted BAM files were used to generate snp_pileup.gz files via the snp-pileup-wrapper.R script (https://github.com/mskcc/facets-suite/tree/master). Tumor purity and ploidy estimation were performed using FACETS[74] (v0.6.2), with the segmentation critical value (cval) set to 150.

Patient-derived organoid flow cytometry

PDOs were plated in 40μL Cultrex domes and cultured until near-100% confluency. For ploidy analysis, PDOs were dissociated to single cells with TrypLE, fixed in 70%EtOH at 4°C for 1 h, washed with DPBS, and stained with 10 μg/mL Hoechst33342 (Life Technologies, #H3570) in 0.1% Triton X-100 PBS. Flow cytometry performed on BD LSR Fortessa II with the 355_379_28 filter.

For HLA analysis, PDOs were treated with 10ng/mL Interferon γ (Millipore Sigma I17001-100UG) or vehicle for 72 h. PDOs were dissociated to single cells with TrypLE, stained with APC anti-human HLA-A/B/C (BioLegend, #311410; RRID: AB_314879) and FITC anti-human β2-microglobulin (BioLegend, #316304; RRID: AB_492837), both at 5 μL/100μL, fixed with the eBioscience Foxp3/Transcription Factor Fixation/Permeabilization Concentrate and Diluent (Thermo Fisher Scientific, #00-5521-00) according to manufacturer, and ran on a BD LSR Fortessa I with the 488_515_30 and 628_670_30 filters. All flow cytometry was performed in the UPMC Hillman Cytometry Facility.

Generation and analyses of scRNA-seq data

Samples from tumor tissues were prepared as described for flow cytometry. To removed dead cells and debris Percoll (Sigma #P4937-500ML) purification was performed. Cell pellets after dead cell/debris removal were resuspended in 0.04% UltraPure BSA (Sigma-Aldrich) in PBS and immediately processed for library preps with DFCI Translational Immunogenomics Lab (TIGL). Gene expression library preparation was conducted using 10× Genomics ChromiumTM instrument (10× Genomics) according to the manufacturer's recommendations using Chromium Next GEM Single Cell 5' HT Kit v2 (10× Genomics). Quality controls for amplified cDNA libraries and final sequencing libraries were performed using Bioanalyzer High Sensitivity DNA Kit (Agilent). Equimolar ratios of libraries were sequenced on an Illumina NovaSeq 6000 (Illumina, RRID:SCR_016387) targeting 2000 reads per cell using 150bp read pairs per library at the Dana-Farber Cancer Institute Molecular Biology Core Facilities. Raw data was processed using CellRanger (RRID:SCR_023221) with bcltofastq function to obtain fastq files for each sample. Files were further processed using Cell Ranger Count 7.0.1 to obtain counts after aligning with mouse mm10 genome assembly. H5 files were then processed in R using Seurat package. Low quality reads were removed according to following criteria: nCount_RNA >1000 & nFeature_RNA <1000 &

Please cite this article in press as: Foidart et al., Whole-genome doubling drives immune evasion by silencing antigen presentation, Cancer Cell (2026), https://doi.org/10.1016/j.ccell.2026.04.007

percent.mt < 20. Percentage of ribosomal reads<40 and log10 genes per UMI>0.8. For scMultiomic analysis, cells were filtered by both criterions of scRNA-seq and scATAC-seq. Final evaluated cell numbers in each sample are summarized in Table S4. Normalization was performed using LogNormalize followed by SCTransform regressing ribosomal percentage, mitochondrial percentage, nCount_RNA and nFeature_RNA. Clustering and subclustering was performed using with the top 30 principal components. Next, cluster were manually annotated using gene.module.scores with specific marker genes. For further characterization cluster 'tumor cells' and 'non-tumor cells' were first subset. 'Non-tumor cells' were then subset into cluster: 'fibroblast', 'endothelial cells', 'T/NK cells', or 'myeloid cells'. Within each subset cells were again annotated using selected marker genes and gene.module.scores and scores were plotted according to each genotype. UMAP visualization was performed using 'scCustomize' package (RRID:SCR_024675). Neighborhood analysis was performed using the ''miloR'' package. Regulator analysis was carried out using the ''SCENIC'' package (RRID:SCR_017247) and cell-cell communication analysis were performed using the 'CellChat' package (RRID:SCR_021946). Interaction corsstalk strength was selected for downstream differential analysis in each cell type between WGD- and WGD+ tumors. The ProjecTILs package (RRID_ RRID:SCR_026854) was used to infer T cell states to a published mouse T cell atlas.[39] For evaluation of MDSC signature in neutrophils, module score function was used to calculate the enrichment level of a previous reported MDSC signature in breast tumors.[36] For integration of RNA-seq and ChIP-seq, BETA (RRID:SCR_005396) was performed as previously described.[40] Briefly, differentially expressed (DE) genes were first computed using DESeq2 (RRID:SCR_015687)[61] and used as one of the inputs. BETA basic modules were used to compute the statistical associations between DE genes and DB peaks using 100kb as the ranges to link gene TSS to each peak. *p* values were derived using one-tailed Kolmogorov-Smirnov test for up-regulated and down-regulated genes respectively.

Generation and analyses of scATAC-seq data

Dissociated viable tumor cells were used for 10× Chromium Single Cell ATAC library preparation. The libraries were sequenced separately on the NovaSeq 6000 (Illumina) system (NovaSeq Control Software v.1.7.0 and v.1.7.5). Single-cell ATAC-seq data were processed using the Cell Ranger ATAC 2.0 pipeline, which included sample demultiplexing, barcode processing, read alignment to the mm10 reference genome, and open chromatin peak quantifications. Single Cell Multiome ATAC + Gene Expression data were preprocessed using the Cell Ranger ARC pipeline ARC 2.0.0, which included sample demultiplexing, barcode processing, read alignment to the mm10 reference genome, gene expression and open chromatin peak quantifications. For downstream analysis of scATAC-seq, we followed the instruction of ''Signac'' package (RRID:SCR_021158). Cells were prefiltered by 3000< fragment counts<50000, FRiP score >0.1, fraction of blacklist region <0,1, nucleosome signal<4 and TSS enrichment score>2. For scMultiomic analysis, cells were filtered by both criterions of scRNA-seq and scATAC-seq. Final evaluated cell numbers in each sample are summarized in Table S4. For data normalization, term frequency–inverse document frequency (TF-IDF) normalization was applied to the filtered peak-by-cell matrix to account for sequencing depth and feature frequency. Dimensionality reduction was performed using singular value decomposition (SVD) to compute latent semantic indexing (LSI) components. Each cell were subjected to lsi dimension reduction from 2 to 30, and then intergrated using the FindIntegrationAnchors function to further reduce the batch effects. Gene activity score was inferred by scATAC-seq data using GeneActivity fucntion to examine marker gene expression and determine cell types of each cluster. The genomic track view of targeted gene loci was visualized using ''CoveragePlot'' function. For copy number inferrence, QuickATAC (Github link: https://github.com/AllenWLynch/QuickATAC) was used to compute a count matrix for peaks at a 1 bp resolution for each cell. The maximum number of overlapping fragments at the same base pair within each peak is used to determine the lower limit of the absolute copy number. Following this, k-means clustering is employed to group the cells based on these estimated lower limits. A heatmap is then generated to visualize the resulting clusters. Briefly, BAM files were filtered using ''mapping_quality $\geq$ 30 and template_length <1000,'' and barcodes were further filtered to include only those with FRiP(Fraction of Reads in Peaks) $\geq$ 0.4 and at least 10,000 fragments per barcode. Mapping_quality (MAPQ) is a score assigned by the aligner to indicate how confident it is that a read is correctly mapped to its location in the reference genome. MAPQ 30 → ∼1 in 1000 chance of being misaligned. Template_length (also known as insert size or TLEN field in SAM) is the length of the DNA fragment represented by a paired-end read— i.e., the distance between the start of the forward and reverse reads. Keep only read pairs where the inferred insert size is less than 1000 bp, excluding unusually long fragments that may indicate mapping artifacts, chimeric reads, or structural variants.

RNA-seq data generation and analyses

For bulk RNA-seq analysis from tumors, total RNA was extracted from snap frozen tumors using Qiagen RNeasy Mini kit. RNA-seq library preparation and sequencing were performed by Azenta RNA-seq service with 15–30 million reads per sample. RNA-seq data was analyzed using the VIPER pipeline.[79] Briefly, reads were aligned using STAR (RRID:SCR_004463) to mm10 mouse genome. Genes with 0 counts in all samples were excluded and remaining counts were normalized via log2 TMM transformation to counts per million (log2 (TMM-CPM +1)) from edgeR (RRID:SCR_012802)[66] for further processing. PCA plots were conducted using edgeR package, heatmaps were visualized using 'ComplexHeatmap' package (RRID:SCR_017270). For differential expression analyses DEseq2[61] was performed using different factor levels according to the experimental design. Enrichment scores of different pathways were calculated using 'gsva' package (RRID:SCR_021058). Immune and stromal scores were calculated using 'ESTIMATE' package.

Please cite this article in press as: Foidart et al., Whole-genome doubling drives immune evasion by silencing antigen presentation, Cancer Cell (2026), https://doi.org/10.1016/j.ccell.2026.04.007

Analyses of public gene expression data

Whole genome-doubling in TCGA (RRID:SCR_003193) and CCLE (RRID:SCR_013836) datasets were called using the 'absolute' package following instructions by Quinton et al.[23] WGD in METABRIC was called using the calculate_fraction_cna function from the facetsSuite R package (v2.0.8) with the ASCAT (RRID:SCR_016868) copy number profiles and ploidy from Pereira et al.[80] WGD calling in Hartwig and PCAWG cohorts were directly downloaded from prior publication.[29] TCGA RNA-seq reads were reprocessed using Salmon v0.14.1 (RRID:SCR_017036)[81] and Log2 (TPM+1) values were used. For the METABRIC dataset, normalized probe intensity values were obtained from Synapse (Syn1688369). For genes with multiple probes, probes with the highest interquartile range (IQR) were selected to represent the gene. For tumor subtype classification in both cohorts, clinical annotation files containing IHC results for ER, PR, and HER2 were used. Tumors were classified as HR^+ if they were positive for either ER or PR but negative for HER2. $HER2^+$ tumors were defined by positive HER2 status, regardless of ER or PR expression. TNBC tumors were defined as negative for all three markers (ER^-, PR^-, and $HER2^-$). 'ISOPure' package was used to deconvolute cancer cell portion transcriptomic data and 'gsva' package was further used to calculate the enrichment score of different antigen processing and presentation signatures. Immune infiltration scores were calculated using 'ESTIMATE' package. For cell line analysis, YM-155 sensitivity scores were downloaded from Depmap portal (RRID:SCR_017655) using the CTRP:417979 screen results, taking AUC (CTD ^2) as the measurement. CRISPR gene dependency scores were taken from the DepMap Public 22Q4 screen. TCGA scATAC-seq raw data were obtained from dbGaP phs000178.v11.p8 with legitimate approval of controlled access. Raw fastq files of 6 basal tumors were reprocessed using the Cell Ranger ATAC 2.0 pipeline, which included sample demultiplexing, barcode processing, read alignment to the hg19 reference genome, and open chromatin peak quantifications. Cancer cells were extracted based on epithelial marker expression for downstream analysis. For paired bone metastases scRNA-seq analysis, raw count matrix was downloaded from GEO: GSE190772. Data were processed using Seurat following the filter and cell type annotation from the original publication.[38,82] 4617 and 5439 cells from BoM1 and BoM2 were analyzed. For data analysis of the FUSCC TNBC cohort,[54] RNA-seq data were downloaded from https://www.biosino.org/node/project/detail/OEP000155. WGD status was classified using the cutoff of predicted ploidy of 2.7 as defined in the original publication. For random effect meta-analysis, we calculated the standardized effect size (Cohen's d) and its corresponding standard error (SE) based on the mean and standard deviation of the two groups in each cohort and their corresponding subsets. These cohort-specific effect sizes were then combined using a random-effects meta-analysis implemented in the metafor R package, with between-study variance estimated using the restricted maximum likelihood (REML) method.

H3K27me3 CUT&Run

Tumors were collected and digested as described before for flow cytometry. Single cell solutions were stained with Live/dead cell staining kit (Life Technology, L34957), anti-CD45-FITC (eBioscience, 11-0451-82, RRID:AB_465050) and anti-EpCAM (BioLegend 118214, RRID:AB_1134102) and sorted for live cells/$CD45^-$/$EpCAM^+$ cells. Approximately 100,000 cells were used to perform Cut&Run using CUTANA ChIC/CUT&RUN Kit Version 4 (Epicypher, 14–1048) according to manufacturer's protocol. Cell permeabilization was performed with 0.005% digitonin and anti-H3K27me3 antibody (Active Motif, 39155, RRID:AB_2561020) was used for targeted capture. Cut&Run libraries were prepared using IDT xGen DNA library prep reagents on a Beckman Coulter Biomek i7 liquid handling platform from approximately 1ng of DNA with 14 cycles of PCR amplification according to manufacturer's protocol. Finished sequencing libraries were quantified by Qubit fluorometer and Agilent TapeStation 2200. Library pooling and indexing was evaluated with shallow sequencing on an Illumina NovaSeq X Plus (RRID:SCR_024568). Subsequently, libraries were sequenced on an Illumina NovaSeq X Plus targeting 20 million 150bp read pairs by the Molecular Biology Core facilities of Dana-Farber Cancer Institute. Data analysis was performed using the nf-core/cutandrun pipeline version 3.2.2. Briefly, reads were aligned using Bowtie2 (RRID:SCR_016368) to mm10 and counts were normalized to CPM. Peak calling was done using SEACR in -stringent mode. Consensus peaks were generated by merging peaks from all samples and featureCounts was used to count reads within consensus peaks from each bam file using –countReadPairs -M -O mode. Count matrix was used for differential abundance calculation using limma with TMM normalization and peak annotation was done using Chipseeker (RRID:SCR_021322). Differential pathway analysis was performed with ChipEnrich in broadenrich 5kb mode. Motif enrichment analysis was performed using MEME Suite (RRID:SCR_001783) using Hocomoco mouse database V11 (RRID:SCR_005409).

Whole exome sequencing

Genomic DNA from cell lines were extracted using DNeasy Blood & Tissue Kits. gDNA was fragmented to 200bp on a Covaris R230 instrument according to manufacturer's protocol. Libraries were prepared using IDT xGEN 2 S Plus DNA reagents on a Beckman Coulter Biomek i7 liquid handling platform from approximately 200ng of DNA according to manufacturer's protocol with 14 cycles of PCR amplification. Finished libraries were quantified by Qubit fluorometer and fragment size distribution was evaluated by Agilent TapeStation 4200. Libraries were pooled together for target enrichment using Twist Mouse Exome Panel reagents and hybrid capture was performed with a 16-h hybridization incubation using a custom probe panel according to manufacturer's protocol. Post-capture library pools were quantified by Qubit fluorometer and Agilent TapeStation 4200. Library pools were further evaluated for quality and pool balance with shallow sequencing on an Illumina MiSeq. Subsequently, libraries were sequenced on an Illumina NovaSeq 6000 with paired-end 150bp reads by the Molecular Biology Core Facilities at Dana-Farber Cancer Institute.

Sequenced reads (FASTQ files) were aligned to mm10 version of human genome with BWA-MEM v.0.7.15 and preprocessed following GATK best practices.[83] The quality of alignment and potential sample contamination was evaluated with the following

software tools FastQC, Picard, and FastQ-Screen. Short nucleotide variants (point mutations and indels) were called using GATK Mutect2 using a ''panel of normals'' based on samples from the 1000 Genomes Project and provided in the Broad Institute's public data repository. Identified variants were annotated with Ensembl Variant Effect Predictor[75] (version 115.2) and transformed into MAF files with the vcf2maf script. The variant calls were further annotated with OncoKB using the oncokb-annotator python package.

QUANTIFICATION AND STATISTICAL ANALYSIS

Statistical analyses

Statistical test was conducted using GraphPad PRISM v9 (RRID:SCR_002798) or an embedded test in the ''ggpubr'' package (RRID:SCR_021139) in R v4.3.1 (RRID:SCR_001905). Normal distribution was first estimated using the Shapiro-Wilk test. Non-parametric tests were used, should data for matched comparisons did not pass the test. Non-paired, two-sided *t* test or Mann-Whitney U test was used for single comparisons. One-way ANOVA corrected for multiple comparisons or the Kruskal-Wallis test was used for multi-group comparisons. All tests were performed with a 95% confidence interval. *p*-values are indicated for each experiment.

Cancer Cell, Volume *44*

Supplemental information

Whole-genome doubling drives immune evasion by silencing antigen presentation

Pierre Foidart, Zheqi Li, Xinran Cai, Marco Seehawer, Daniel D. Brown, Amatullah Tawawalla, Pilar Baldominos, Salma Parvin, Jun Nishida, Ernesto Rojas-Jimenez, Triet M. Bui, Benedetto Diciaccio, Rahul Kumar, Brent T. Schlegel, Marie-Anne Goyette, TashJae Scales, Pengze Yan, Xintao Qiu, Rong Li, Yijia Jiang, Yingtian Xie, Mahmoud Aarabi, Xiao-Yun Huang, Laura E. Stevens, Paloma Cejas, Lise Mangiante, Cristina Irene Sotomayor Vivas, Kathleen E. Houlahan, Christina Curtis, Steffi Oesterreich, Isaac S. Harris, Anthony G. Letai, Adrian V. Lee, Henry W. Long, Judith Agudo, and Kornelia Polyak

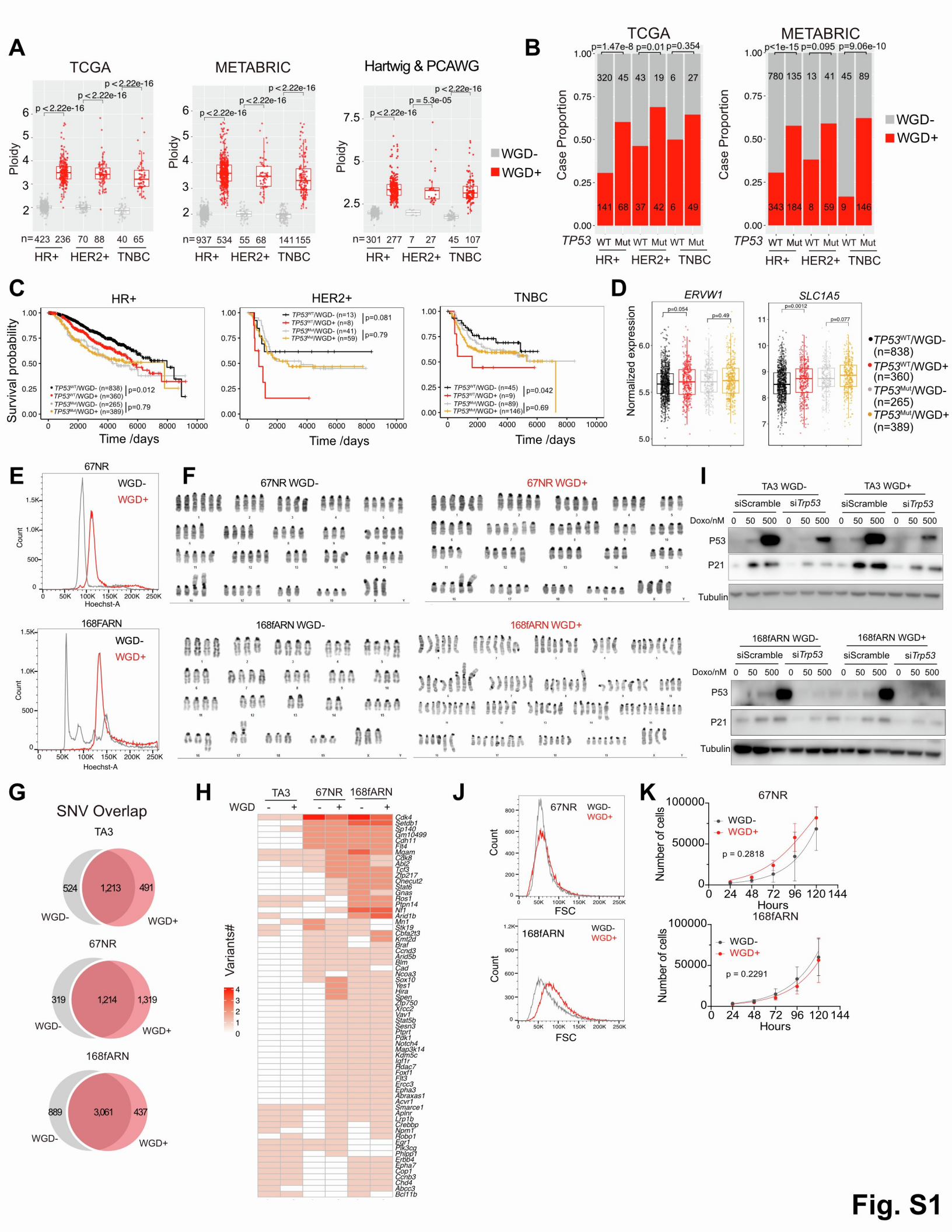
A
TCGA
METABRIC
Hartwig & PCAWG
Ploidy
p < 2.22e-16
p = 5.3e-05
WGD-
WGD+
n=423 236 70 88 40 65
n=937 534 55 68 141 155
n=301 277 7 27 45 107
HR+ HER2+ TNBC
B
TCGA
METABRIC
Case Proportion
p=1.47e-8 p=0.01 p=0.354
p<1e-15 p=0.095 p=9.06e-10
320 45 43 19 6 27
141 68 37 42 6 49
780 135 13 41 45 89
343 184 8 59 9 146
TP53 WT Mut WT Mut WT Mut
HR+ HER2+ TNBC
C
HR+
HER2+
TNBC
Survival probability
Time /days
TP53WT/WGD- (n=838)
TP53WT/WGD+ (n=360)
TP53Mut/WGD- (n=265)
TP53Mut/WGD+ (n=389)
p=0.012
p=0.79
TP53WT/WGD- (n=13)
TP53WT/WGD+ (n=8)
TP53Mut/WGD- (n=41)
TP53Mut/WGD+ (n=59)
p=0.081
p=0.79
TP53WT/WGD- (n=45)
TP53WT/WGD+ (n=9)
TP53Mut/WGD- (n=89)
TP53Mut/WGD+ (n=146)
p=0.042
p=0.69
D
ERVW1
SLC1A5
Normalized expression
p=0.054
p=0.49
p=0.0012
p=0.077
TP53WT/WGD- (n=838)
TP53WT/WGD+ (n=360)
TP53Mut/WGD- (n=265)
TP53Mut/WGD+ (n=389)
E
67NR
168FARN
WGD-
WGD+
Count
Hoechst-A
F
67NR WGD-
67NR WGD+
168fARN WGD-
168fARN WGD+
I
TA3 WGD-
TA3 WGD+
siScramble
siTrp53
Doxo/nM 0 50 500 0 50 500 0 50 500 0 50 500
P53
P21
Tubulin
168fARN WGD-
168fARN WGD+
G
SNV Overlap
TA3
524 1,213 491
67NR
319 1,214 1,319
168fARN
889 3,061 437
WGD-
WGD+
H
TA3
67NR
168fARN
WGD
Variants#
Cdk4
Setdb1
Sp140
Gm10499
Cdh11
Flt4
Mgam
Cdk8
Abl2
Tcf3
Zfp217
Chnecut2
Stat6
Gnas
Ros1
Ptpn14
Nf1
Arid1b
Mn1
Stk19
Cbfa2t3
Kmt2d
Braf
Ccnd3
Arid5b
Blm
Cad
Ncoa3
Sox10
Yes1
Hira
Spen
Zfp750
Xrcc2
Vav1
Stat5b
Sesn3
Ptprt
Pdk1
Notch4
Map3k14
Kdm5c
Igf1r
Hdac7
Foxf1
Flt3
Ercc3
Epha3
Abraxas1
Acvr1
Smarce1
Aplnr
Ltp1b
Crebbp
Npm1
Robo1
Egr1
Pik3cg
Phlpp1
Erbb4
Epha7
Cop1
Ccnb3
Chd4
Abcc3
Bcl11b
J
67NR
168fARN
WGD-
WGD+
Count
FSC
K
67NR
168fARN
Number of cells
p = 0.2818
p = 0.2291
Hours

Fig. S1

Figure S1. Characterization of the WGD models. Related to Figure 1.

(A) Box plots showing the estimated ploidy of tumors identified as WGD- or WGD+ in the indicated breast tumor subtypes and patient cohorts. Mann Whitney U test was used.

(B) Bar plots showing the percentage of tumors classified as WGD- or WGD+ with the indicated *TP53* mutation status in the TCGA and METABRIC cohorts. Fisher's exact test was used.

(C) Kaplan-Meier plots showing the breast cancer-specific survival of patients in the METABRIC cohort with the indicated tumor subsets classified by TP53 and WGD status. Log rank test was used.

(D) Box plots illustrating the expression of *ERVW1* and *SLC1A5* in the METABRIC cohort subdivided based on *TP53* mutation and WGD status. Mann Whitney U test was used for each comparison.

(E) Flow cytometry of Hoechst-stained cells analyzing DNA content of 67NR and 168FARN WGD- and WGD+ cells.

(F) Representative karyotypes of 67NR and 168FARN WGD- and WGD+ cells.

(G) Venn diagram showing the overlap of sequence variants between WGD- and WGD+ cells in the TA3, 67NR and 168fARN models.

(H) Heatmap illustrating variants numbers of OncoKB annotated oncogene and tumor suppressor genes detected in TA3, 67NR and 168fARN models (in more than 3 samples).

(I) Immunoblot showing p53 and p21 expression in WGD- and WGD+ cells in the indicated cell line models and treatment groups. Cells were transfected with either siRNA against scramble or *Trp53* for 48 hours and stimulated with 50nM or 500nM doxorubicin for 12 hours. Tubulin was used as loading control.

(J) Flow cytometry for forward scatter of 67NR and 168FARN WGD- and WGD+ cells.

(K) Plot depicting the viable cell numbers of WGD- and WGD+ 168fARN and 67NR cell cultures at the indicated time points after plating. Data are represented as mean ± SD, n =3. Comparison of logistic growth curve. Error bars represent SD. Extra sum-of-squares F test.

Box plots in panels A and D represent the median (center line) and interquartile range (box, 25th-75th percentiles). Whiskers extend to 1.5× the interquartile range.

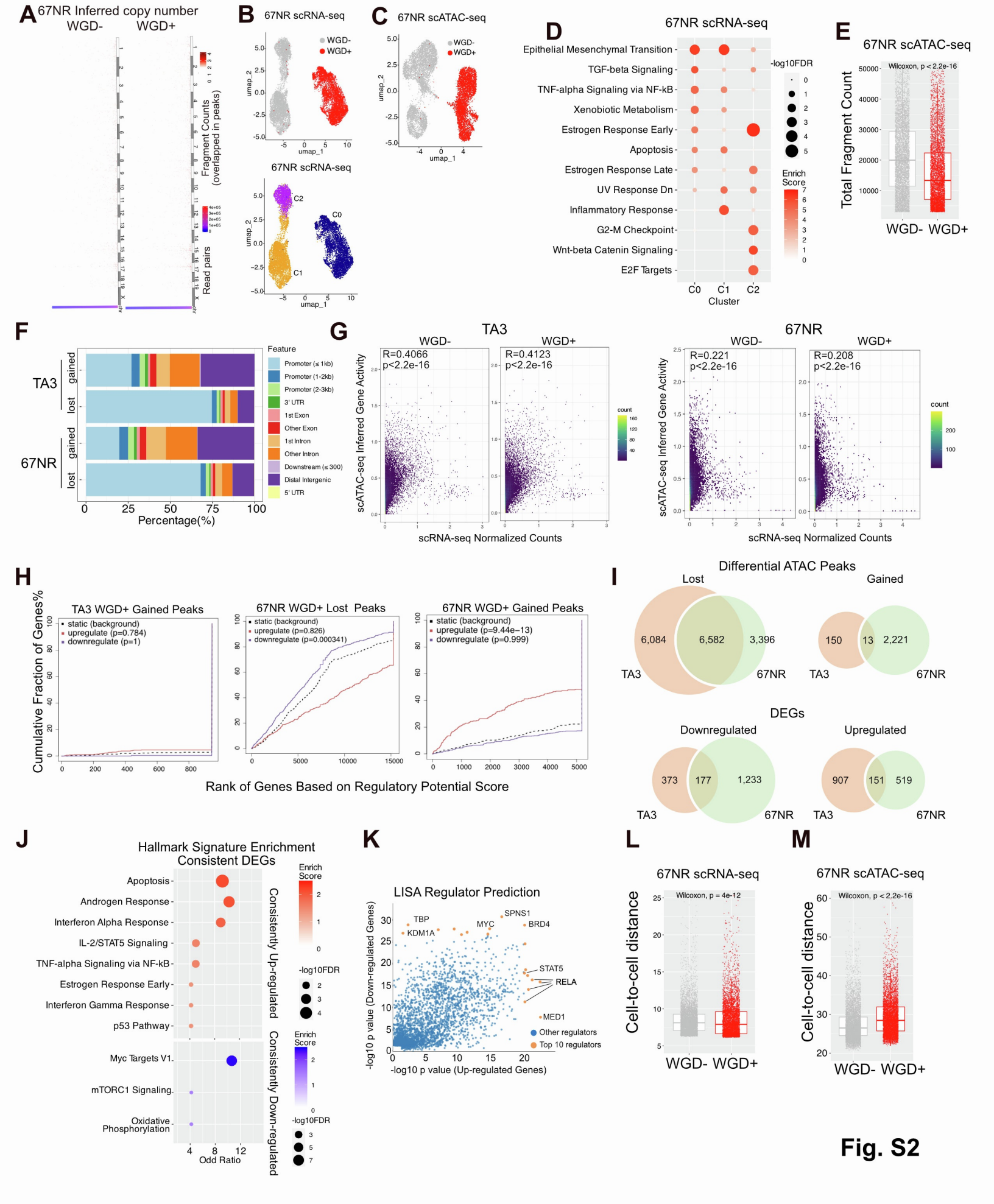
A
67NR Inferred copy number
WGD-
WGD+
Fragment Counts (overlapped in peaks)
Read pairs
B
67NR scRNA-seq
WGD-
WGD+
umap_1
umap_2
67NR scRNA-seq
C2
C0
C1
C
67NR scATAC-seq
D
67NR scRNA-seq
Epithelial Mesenchymal Transition
TGF-beta Signaling
TNF-alpha Signaling via NF-kB
Xenobiotic Metabolism
Estrogen Response Early
Apoptosis
Estrogen Response Late
UV Response Dn
Inflammatory Response
G2-M Checkpoint
Wnt-beta Catenin Signaling
E2F Targets
C0
C1
C2
Cluster
-log10FDR
Enrich Score
E
67NR scATAC-seq
Wilcoxon, p < 2.2e-16
Total Fragment Count
WGD-
WGD+
F
TA3
67NR
gained
lost
Feature
Promoter (≤ 1kb)
Promoter (1-2kb)
Promoter (2-3kb)
3' UTR
1st Exon
Other Exon
1st Intron
Other Intron
Downstream (≤ 300)
Distal Intergenic
5' UTR
Percentage(%)
G
TA3
67NR
WGD-
WGD+
R=0.4066
p<2.2e-16
R=0.4123
p<2.2e-16
R=0.221
p<2.2e-16
R=0.208
p<2.2e-16
scATAC-seq Inferred Gene Activity
scRNA-seq Normalized Counts
count
H
TA3 WGD+ Gained Peaks
67NR WGD+ Lost Peaks
67NR WGD+ Gained Peaks
static (background)
upregulate (p=0.784)
downregulate (p=1)
upregulate (p=0.826)
downregulate (p=0.000341)
upregulate (p=9.44e−13)
downregulate (p=0.999)
Cumulative Fraction of Genes%
Rank of Genes Based on Regulatory Potential Score
I
Differential ATAC Peaks
Lost
Gained
6,084
6,582
3,396
150
13
2,221
TA3
67NR
DEGs
Downregulated
Upregulated
373
177
1,233
907
151
519
J
Hallmark Signature Enrichment
Consistent DEGs
Apoptosis
Androgen Response
Interferon Alpha Response
IL-2/STAT5 Signaling
TNF-alpha Signaling via NF-kB
Estrogen Response Early
Interferon Gamma Response
p53 Pathway
Myc Targets V1
mTORC1 Signaling
Oxidative Phosphorylation
Consistently Up-regulated
Consistently Down-regulated
Enrich Score
-log10FDR
Odd Ratio
K
LISA Regulator Prediction
TBP
KDM1A
MYC
SPNS1
BRD4
STAT5
RELA
MED1
Other regulators
Top 10 regulators
-log10 p value (Down-regulated Genes)
-log10 p value (Up-regulated Genes)
L
67NR scRNA-seq
Wilcoxon, p = 4e-12
Cell-to-cell distance
WGD-
WGD+
M
67NR scATAC-seq
Wilcoxon, p < 2.2e-16
Cell-to-cell distance
WGD-
WGD+

Fig. S2

Figure S2. scRNA-seq and scATAC-seq data. Related to Figure 1.

(A) Heatmap showing the copy number estimation by counts of detected overlapped fragments in ATAC peaks using scATAC-seq data from 67NR WGD+ and WGD- cells.

(B) UMAP of scRNA-seq of 67NR WGD- and WGD+ cells colored by genotype (Top) and cell clusters (Bottom).

(C) UMAP of scATAC-seq of 67NR WGD- and WGD+ cells colored by genotype.

(D) Dot plot showing the enrichment of hallmark pathways in the marker genes of three subclusters in the 67NR model scRNA-seq data.

(E) Box plot depicting total DNA fragment counts in 67NR scATAC-seq data.

(F) Stacked bar plot showing the distribution of genomic features of differential ATAC peaks between WGD+ and WGD- cells in the TA3 and 67NR models.

(G) Scatter plot depicting the Pearson correlation of each gene's normalized expression from scRNA-seq and referred activity score from scATAC-seq in the indicated WGD model.

(H) Line plot showing the BETA association of differential ATAC-seq peaks between WGD+ and WGD- cells to DEGs in the TA3 and 67NR models. One-sided Kolmogorov–Smirnov test.

(I) Venn diagrams showing the overlap of differential ATAC peaks and differentially expressed genes (WGD+ vs. WGD- cells) between TA3 and 67NR cell models. One-sided Kolmogorov–Smirnov test.

(J) Dot plot showing the enrichment of hallmark pathways in the consistently differentially expressed genes (WGD+ vs. WGD- cells) between the two models.

(K) Scatter plot depicting correlation of the predicted regulators from consistently up and down-regulated DEGs.

(L) Box plot showing the transcriptomic cell-to-cell Euclidean distance from PCA dimension reduction of scRNA-seq data. Mann Whitney U test was used.

(M) Box plot showing the epigenetic cell-to-cell Euclidean distance from lsi dimension reduction of scATAC-seq data. Mann Whitney U test was used.

Box plots in panels E, L, and M represent the median (center line) and interquartile range (box, 25th-75th percentiles). Whiskers extend to 1.5× the interquartile range.

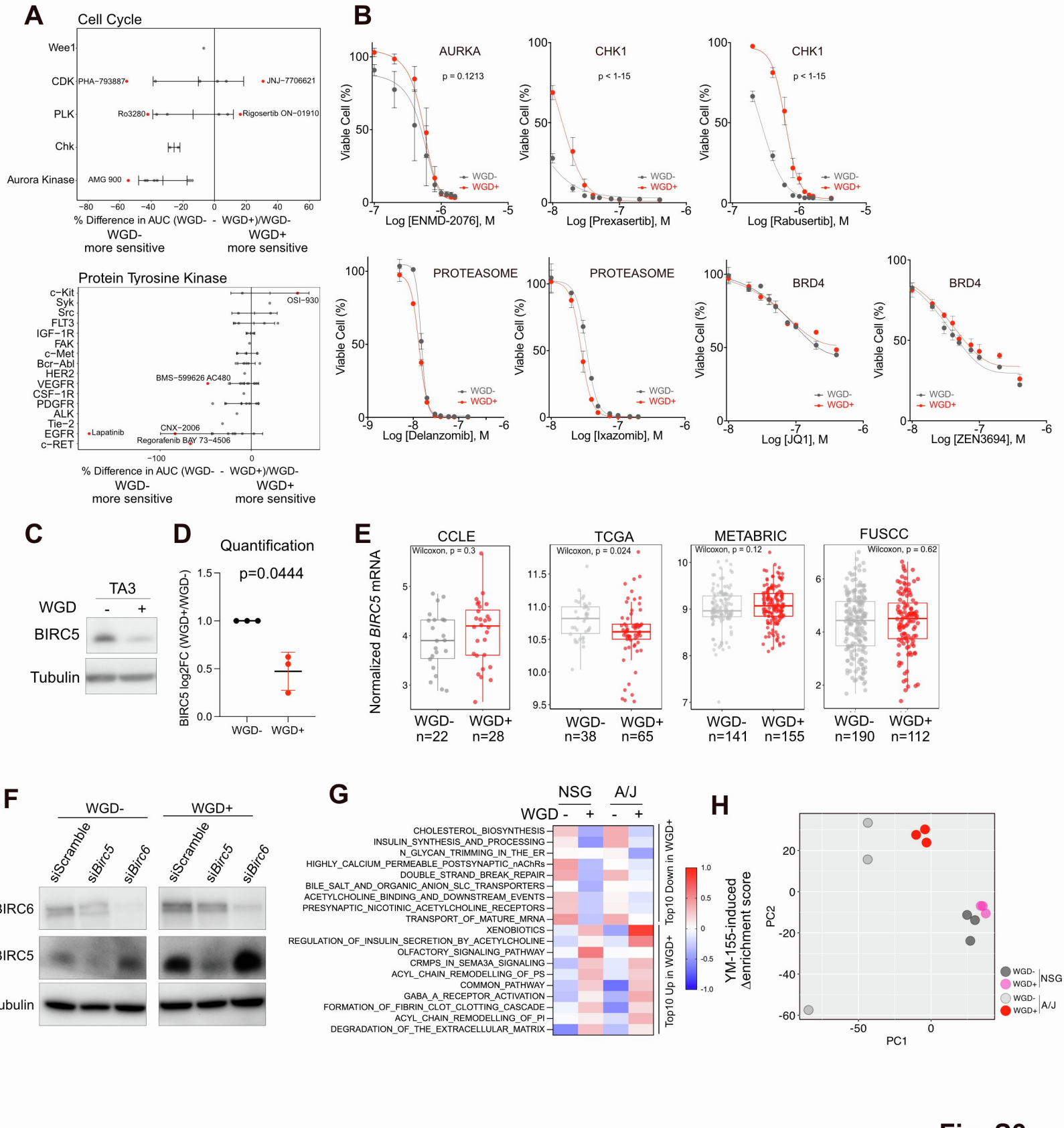
A
Cell Cycle
Wee1
CDK
PHA−793887
JNJ−7706621
PLK
Ro3280
Rigosertib ON−01910
Chk
Aurora Kinase
AMG 900
% Difference in AUC (WGD- - WGD+)/WGD-
WGD- more sensitive
WGD+ more sensitive
Protein Tyrosine Kinase
c−Kit
Syk
Src
FLT3
IGF−1R
FAK
c−Met
Bcr−Abl
HER2
VEGFR
CSF−1R
PDGFR
ALK
Tie−2
EGFR
c−RET
OSI−930
BMS−599626 AC480
Lapatinib
CNX−2006
Regorafenib BAY 73−4506
B
AURKA
p = 0.1213
CHK1
p < 1-15
CHK1
p < 1-15
Viable Cell (%)
WGD-
WGD+
Log [ENMD-2076], M
Log [Prexasertib], M
Log [Rabusertib], M
PROTEASOME
PROTEASOME
BRD4
BRD4
Log [Delanzomib], M
Log [Ixazomib], M
Log [JQ1], M
Log [ZEN3694], M
C
TA3
WGD
BIRC5
Tubulin
D
Quantification
p=0.0444
BIRC5 log2FC (WGD+/WGD-)
WGD-
WGD+
E
CCLE
TCGA
METABRIC
FUSCC
Normalized BIRC5 mRNA
Wilcoxon, p = 0.3
Wilcoxon, p = 0.024
Wilcoxon, p = 0.12
Wilcoxon, p = 0.62
WGD- n=22
WGD+ n=28
WGD- n=38
WGD+ n=65
WGD- n=141
WGD+ n=155
WGD- n=190
WGD+ n=112
F
WGD-
WGD+
siScramble
siBirc5
siBirc6
BIRC6
BIRC5
Tubulin
G
NSG
A/J
WGD
CHOLESTEROL_BIOSYNTHESIS
INSULIN_SYNTHESIS_AND_PROCESSING
N_GLYCAN_TRIMMING_IN_THE_ER
HIGHLY_CALCIUM_PERMEABLE_POSTSYNAPTIC_nAChRs
DOUBLE_STRAND_BREAK_REPAIR
BILE_SALT_AND_ORGANIC_ANION_SLC_TRANSPORTERS
ACETYLCHOLINE_BINDING_AND_DOWNSTREAM_EVENTS
PRESYNAPTIC_NICOTINIC_ACETYLCHOLINE_RECEPTORS
TRANSPORT_OF_MATURE_MRNA
XENOBIOTICS
REGULATION_OF_INSULIN_SECRETION_BY_ACETYLCHOLINE
OLFACTORY_SIGNALING_PATHWAY
CRMPS_IN_SEMA3A_SIGNALING
ACYL_CHAIN_REMODELLING_OF_PS
COMMON_PATHWAY
GABA_A_RECEPTOR_ACTIVATION
FORMATION_OF_FIBRIN_CLOT_CLOTTING_CASCADE
ACYL_CHAIN_REMODELLING_OF_PI
DEGRADATION_OF_THE_EXTRACELLULAR_MATRIX
Top10 Down in WGD+
Top10 Up in WGD+
YM-155-induced Δenrichment score
H
PC1
PC2
WGD-
WGD+
NSG
A/J

Fig. S3

Figure S3. Results and validation of the SMI screen. Related to Figure 2.

(A) Differences in sensitivities of drugs targeting different protein tyrosine kinases and proteins involved in cell cycle regulation, grouped by target, in WGD- and WGD+ cells.

(B) Dose response curves of the indicated compounds tested at various concentrations in WGD- and WGD+ cells. Data are represented as mean ± SEM, n =2-3 per condition. Extra sum-of-squares F test.

(C) Immunoblot analysis of BIRC5 protein levels in the TA3 WGD- and WGD+ cell models. Tubulin was used as loading control.

(D) Dot plot showing the log2 fold change of BIRC5 protein levels in WGD+ normalized to WGD- cells merged from three independent immunoblot experiments. Students' t test was used.

(E) Box plot showing *BIRC5* gene expression from deconvoluted tumor components between WGD- and WGD+ from TCGA and METABRIC TNBC samples and from bulk RNA-seq data of FUSCC and CCLE breast cancer cell lines. Mann Whitney U test was used. Box plots represent the median (center line) and interquartile range (box, 25th-75th percentiles). Whiskers extend to 1.5× the interquartile range.

(F) Immunoblot analysis of BIRC5 and BIRC6 protein levels in WGD- and WGD+ TA3 cells in the presence or absence of *Birc5* or *Birc6* siRNA knockdown. Tubulin was used as loading control.

(G) Heatmap illustrating YM-155 induced changes in gene set enrichment in tumors in the indicated groups. Top 10 pathways with most pronounced differences between WGD+ versus WGD- tumors are shown.

(H) Principal component analysis (PCA) plot showing the transcriptomic distribution of WGD- and WGD+ tumors from A/J and NSG mice. n=3 per group.

Error bars represent SEM (B) and SD (D).

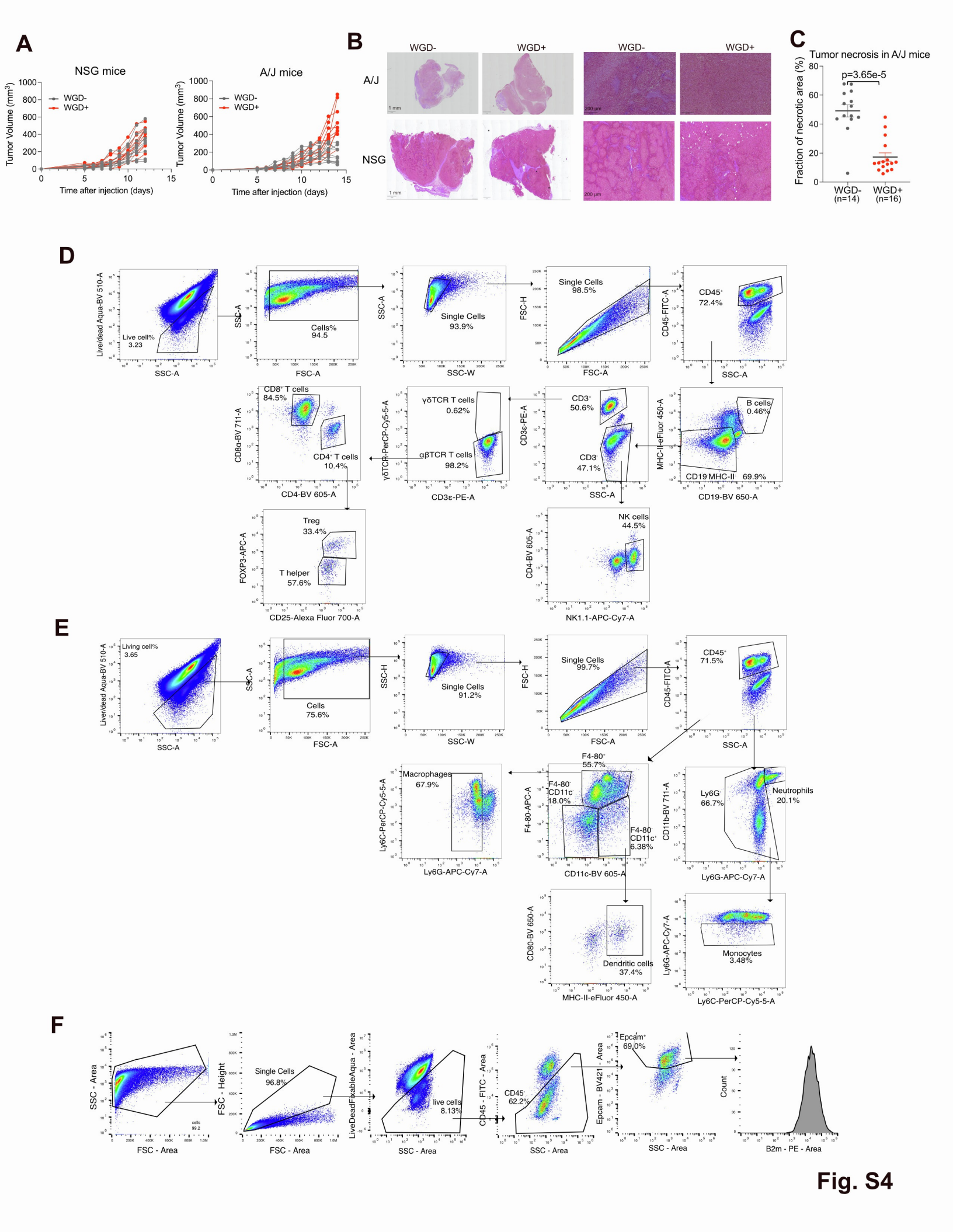
A
NSG mice
A/J mice
Tumor Volume (mm3)
Time after injection (days)
WGD-
WGD+
B
WGD-
WGD+
A/J
NSG
C
Tumor necrosis in A/J mice
Fraction of necrotic area (%)
p=3.65e-5
WGD- (n=14)
WGD+ (n=16)
D
Live/dead Aqua-BV 510-A
Live cell% 3.23
SSC-A
FSC-A
Cells% 94.5
SSC-W
Single Cells 93.9%
FSC-H
Single Cells 98.5%
CD45-FITC-A
CD45+ 72.4%
CD8+ T cells 84.5%
CD8α-BV 711-A
CD4+ T cells 10.4%
CD4-BV 605-A
γδTCR T cells 0.62%
αβTCR T cells 98.2%
γδTCR-PerCP-Cy5-5-A
CD3ε-PE-A
CD3+ 50.6%
CD3 47.1%
B cells 0.46%
MHC-II-eFluor 450-A
CD19+MHC-II+ 69.9%
CD19-BV 650-A
Treg 33.4%
T helper 57.6%
FOXP3-APC-A
CD25-Alexa Fluor 700-A
NK cells 44.5%
NK1.1-APC-Cy7-A
E
Living cell% 3.65
Cells 75.6%
Single Cells 91.2%
Single Cells 99.7%
CD45+ 71.5%
Macrophages 67.9%
Ly6C-PerCP-Cy5-5-A
Ly6G-APC-Cy7-A
F4-80+ 55.7%
F4-80- CD11c- 18.0%
F4-80- CD11c+ 6.38%
F4-80-APC-A
CD11c-BV 605-A
Ly6G- 66.7%
Neutrophils 20.1%
CD11b-BV 711-A
CD80-BV 650-A
Dendritic cells 37.4%
MHC-II-eFluor 450-A
Monocytes 3.48%
F
SSC - Area
FSC - Area
Single Cells 96.8%
FSC - Height
LiveDeadFixableAqua - Area
live cells 8.13%
SSC - Height
CD45 - FITC - Area
CD45- 62.2%
Epcam - BV421 - Area
Epcam+ 69.0%
Count
B2m - PE - Area

Fig. S4

Figure S4. Histology and FACS gating strategy. Related to Figure 3 and STAR Methods.

(A) Plots depicting the growth of each individual tumor (n=10/group) derived from 100,000 TA3 WGD- or WGD+ cells in immunodeficient NSG and in immunocompetent A/J mice.

(B) Representative hematoxylin-eosin-stained sections of WGD- and WGD+ tumors from A/J and NSG mice. Scale bars are 1mm and 200 μm.

(C) Dot plot representing the quantification of necrotic areas in WGD- and WGD+ tumors in A/J mice at day 14. Mann-Whiteny U test was used. Error bars represent SEM.

(D,E,F) Scatter plots indicating the gating strategy used for polychromatic FACS to quantify the relative abundance of major cell types in lymphoid (C) and myeloid (D) populations as well as quantifying antigen presentation in $EpCAM^{+}CD45^{-}$ cells (E). SSC, side scatter. FSC, forward scatter.

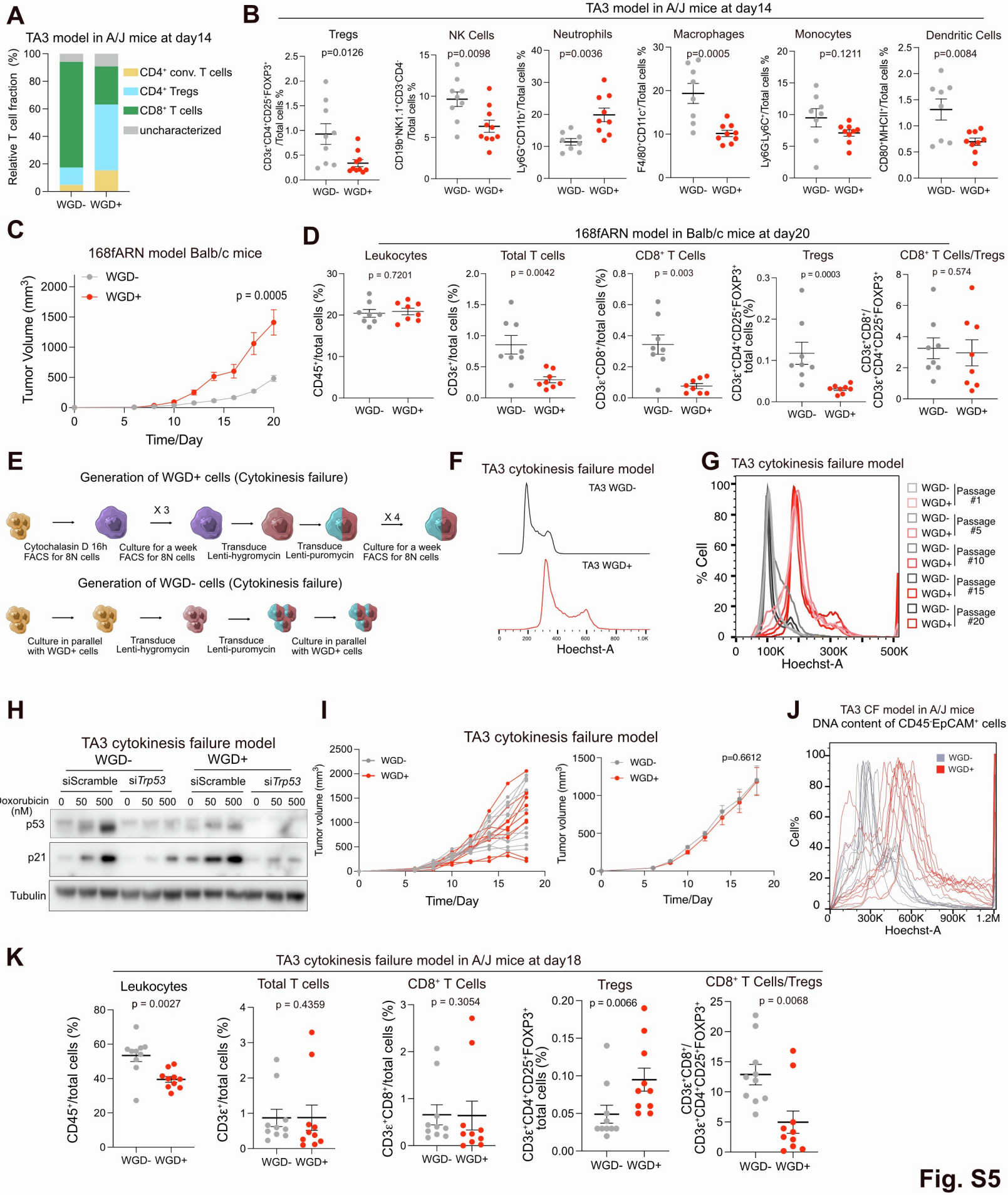
A
TA3 model in A/J mice at day14
Relative T cell fraction (%)
CD4+ conv. T cells
CD4+ Tregs
CD8+ T cells
uncharacterized
WGD- WGD+
B
TA3 model in A/J mice at day14
Tregs
p=0.0126
NK Cells
p=0.0098
Neutrophils
p=0.0036
Macrophages
p=0.0005
Monocytes
p=0.1211
Dendritic Cells
p=0.0084
C
168fARN model Balb/c mice
WGD-
WGD+
p = 0.0005
Tumor Volume (mm3)
Time/Day
D
168fARN model in Balb/c mice at day20
Leukocytes
p = 0.7201
Total T cells
p = 0.0042
CD8+ T Cells
p = 0.003
Tregs
p = 0.0003
CD8+ T Cells/Tregs
p = 0.574
E
Generation of WGD+ cells (Cytokinesis failure)
Cytochalasin D 16h
FACS for 8N cells
X 3
Culture for a week
FACS for 8N cells
Transduce
Lenti-hygromycin
Transduce
Lenti-puromycin
X 4
Culture for a week
FACS for 8N cells
Generation of WGD- cells (Cytokinesis failure)
Culture in parallel
with WGD+ cells
Transduce
Lenti-hygromycin
Transduce
Lenti-puromycin
Culture in parallel
with WGD+ cells
F
TA3 cytokinesis failure model
TA3 WGD-
TA3 WGD+
Hoechst-A
G
TA3 cytokinesis failure model
% Cell
Hoechst-A
Passage #1
Passage #5
Passage #10
Passage #15
Passage #20
H
TA3 cytokinesis failure model
WGD-
WGD+
siScramble
siTrp53
Doxorubicin (nM)
p53
p21
Tubulin
I
TA3 cytokinesis failure model
Tumor volume (mm3)
Time/Day
p=0.6612
J
TA3 CF model in A/J mice
DNA content of CD45-EpCAM+ cells
Cell%
Hoechst-A
K
TA3 cytokinesis failure model in A/J mice at day18
Leukocytes
p = 0.0027
Total T cells
p = 0.4359
CD8+ T Cells
p = 0.3054
Tregs
p = 0.0066
CD8+ T Cells/Tregs
p = 0.0068

Fig. S5

Figure S5. Characterization of other WGD- and WGD+ models. Related to Figure 3.

(A) Stacked bar plot showing the percentages of the indicated T cells populations quantified by flow cytometry normalized to total T cell population in TA3 WGD- and WGD+ tumors in A/J mice at day 14.

(B) Scatter dot plot showing the relative fraction of the indicated immune cell types quantified by flow cytometry in TA3 WGD- and WGD+ tumors in A/J mice at day 14. Data are represented as mean ± SEM, n =9-10 per condition. Mann Whitney U test was used.

(C) Plot depicting the volume of tumors derived from 200,000 168fARN WGD- or WGD+ cells in immunocompetent Balb/c mice. Data are represented as mean ± SEM, n = 8 per condition, two-Way ANOVA analysis- Šídák's multiple comparisons test.

(D) Scatter dot plot showing the relative fraction of the indicated immune cell types quantified by flow cytometry in 168fARN WGD- and WGD+ tumors in Balb/c mice at day 20. Data are represented as mean ± SEM, n =8 per condition. Mann Whitney U test was used.

(E) Schematic outline of creating the cytokinesis failure WGD model.

(F) Flow cytometry of TA3 cytokinesis failure WGD- and WGD+ cells stained with Hoechst33342 to assess DNA content.

(G) Flow cytometry plot of TA3 cytokinesis failure WGD- and WGD+ cells stained with Hoechst33342 collected at five different passages during prolonged culture to assess DNA content.

(H) Immunoblot for p53 and p21 in TA3 cytokinesis failure WGD- and WGD+ cells transfected with either siRNA against scramble or *Trp53* for 48 hours and stimulated with 50nM or 500nM doxorubicin for 12 hours. Tubulin was used as loading control.

(I) Plots depicting average (I) or individual (J) growth of tumors derived from 100,000 TA3 cytokinesis failure WGD- or WGD+ cells in immunocompetent A/J mice. Data are represented as mean ± SEM, n = 8 per condition, two-Way ANOVA analysis- Šídák's multiple comparisons test.

(J) Flow cytometry of $EpCAM^{+}CD45^{-}$ cells from TA3 cytokinesis failure model WGD- and WGD+ tumors stained with Hoechst33342 to assess DNA content.

(K) Scatter dot plot showing the relative fraction of the indicated immune cell types quantified by flow cytometry in TA3 cytokinesis failure model WGD- and WGD+ tumors in A/J mice at day 18. Data are represented as mean ± SEM, n =10 per condition. Mann Whitney U test was used. Error bars represent SEM (B,C,D,I, K).

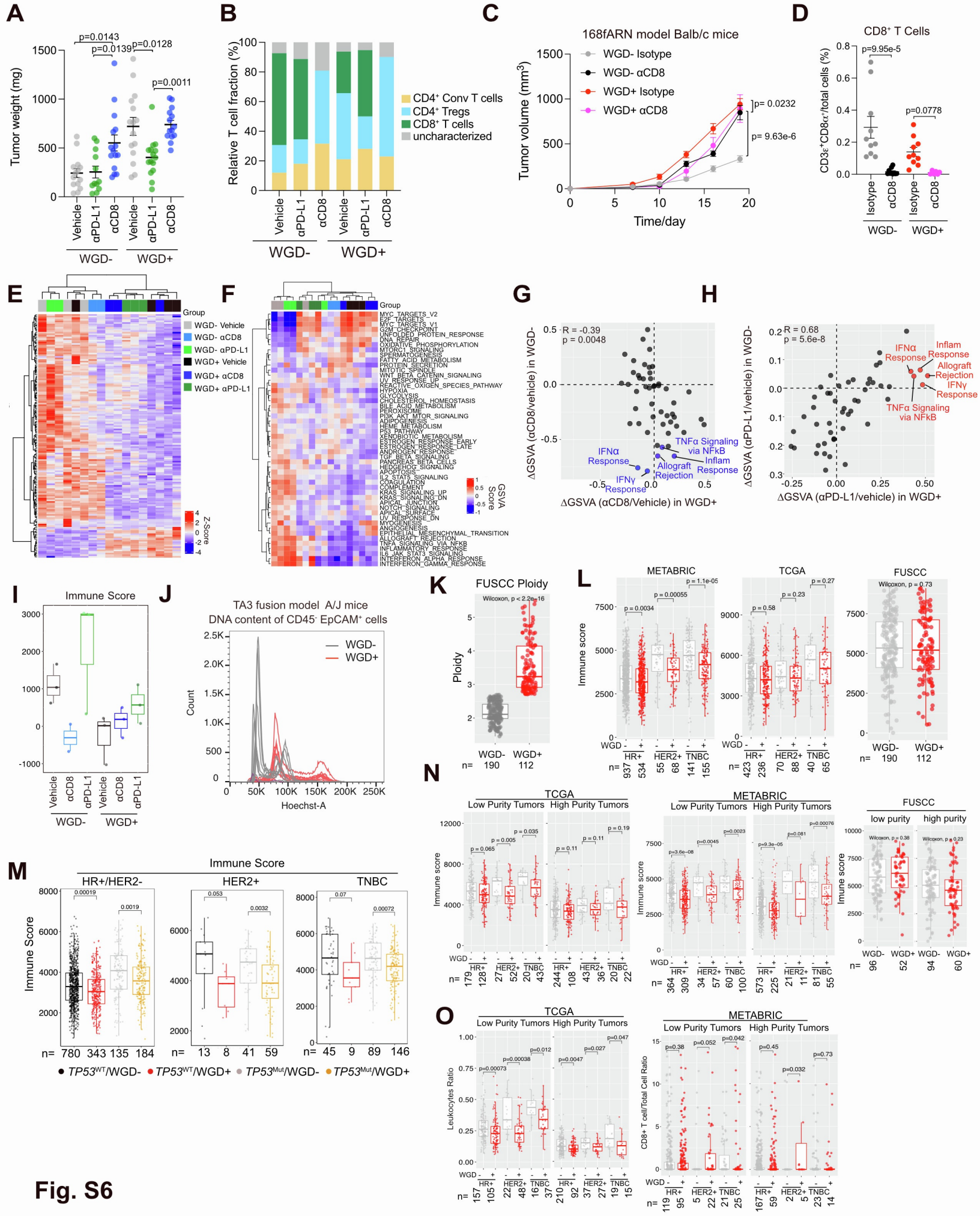
A
Tumor weight (mg)
p=0.0143
p=0.0139
p=0.0128
p=0.0011
Vehicle
αPD-L1
αCD8
WGD-
WGD+
B
Relative T cell fraction (%)
CD4⁺ Conv T cells
CD4⁺ Tregs
CD8⁺ T cells
uncharacterized
C
168fARN model Balb/c mice
WGD- Isotype
WGD- αCD8
WGD+ Isotype
WGD+ αCD8
Tumor volume (mm³)
Time/day
p= 0.0232
p= 9.63e-6
D
CD8⁺ T Cells
p=9.95e-5
p=0.0778
CD3ε⁺CD8α⁺/total cells (%)
Isotype
αCD8
E
Group
WGD- Vehicle
WGD- αCD8
WGD- αPD-L1
WGD+ Vehicle
WGD+ αCD8
WGD+ αPD-L1
Z-Score
F
GSVA Score
MYC_TARGETS_V2
E2F_TARGETS
MYC_TARGETS_V1
G2M_CHECKPOINT
UNFOLDED_PROTEIN_RESPONSE
DNA_REPAIR
OXIDATIVE_PHOSPHORYLATION
MTORC1_SIGNALING
SPERMATOGENESIS
FATTY_ACID_METABOLISM
PROTEIN_SECRETION
MITOTIC_SPINDLE
WNT_BETA_CATENIN_SIGNALING
UV_RESPONSE_UP
REACTIVE_OXIGEN_SPECIES_PATHWAY
HYPOXIA
GLYCOLYSIS
CHOLESTEROL_HOMEOSTASIS
BILE_ACID_METABOLISM
PEROXISOME
PI3K_AKT_MTOR_SIGNALING
ADIPOGENESIS
HEME_METABOLISM
P53_PATHWAY
XENOBIOTIC_METABOLISM
ESTROGEN_RESPONSE_EARLY
ESTROGEN_RESPONSE_LATE
ANDROGEN_RESPONSE
TGF_BETA_SIGNALING
PANCREAS_BETA_CELLS
HEDGEHOG_SIGNALING
APOPTOSIS
IL2_STAT5_SIGNALING
COAGULATION
COMPLEMENT
KRAS_SIGNALING_UP
KRAS_SIGNALING_DN
APICAL_JUNCTION
NOTCH_SIGNALING
APICAL_SURFACE
UV_RESPONSE_DN
MYOGENESIS
ANGIOGENESIS
EPITHELIAL_MESENCHYMAL_TRANSITION
ALLOGRAFT_REJECTION
TNFA_SIGNALING_VIA_NFKB
INFLAMMATORY_RESPONSE
IL6_JAK_STAT3_SIGNALING
INTERFERON_ALPHA_RESPONSE
INTERFERON_GAMMA_RESPONSE
G
R = -0.39
p = 0.0048
ΔGSVA (αCD8/vehicle) in WGD-
ΔGSVA (αCD8/Vehicle) in WGD+
IFNα Response
TNFα Signaling via NFkB
Inflam Response
Allograft Rejection
IFNγ Response
H
R = 0.68
p = 5.6e-8
ΔGSVA (αPD-L1/vehicle) in WGD-
ΔGSVA (αPD-L1/vehicle) in WGD+
IFNα Response
Inflam Response
Allograft Rejection
IFNγ Response
TNFα Signaling via NFkB
I
Immune Score
Vehicle
αCD8
αPD-L1
WGD-
WGD+
J
TA3 fusion model A/J mice
DNA content of CD45⁻ EpCAM⁺ cells
WGD-
WGD+
Count
Hoechst-A
K
FUSCC Ploidy
Wilcoxon, p < 2.2e-16
Ploidy
n= 190 112
L
METABRIC
TCGA
FUSCC
Immune score
Wilcoxon, p = 0.73
HR+
HER2+
TNBC
N
TCGA
METABRIC
FUSCC
Low Purity Tumors
High Purity Tumors
low purity
high purity
Immune score
M
Immune Score
HR+/HER2-
HER2+
TNBC
n= 780 343 135 184
n= 13 8 41 59
n= 45 9 89 146
TP53WT/WGD-
TP53WT/WGD+
TP53Mut/WGD-
TP53Mut/WGD+
O
TCGA
METABRIC
Low Purity Tumors
High Purity Tumors
Leukocytes Ratio
CD8+ T cell/Total Cell Ratio

Fig. S6

Figure S6. Characterization of the immune environment of WGD- and WGD+ tumors. Related to Figure 3.

(A) Scatter dot plots showing the weight of TA3 WGD- and WGD+ tumors from the indicated treatment group collected at endpoint (day 12). Data are represented as mean ± SEM, n =16 per condition. Kruskal-Wallis test.

(B) Stacked bar plot showing the percentages of $CD8^+$ T cells, $CD4^+$ Tregs, $CD4^+$ conventional T cells, and uncharacterized T cells normalized to total T cell population in each indicated group.

(C) Plots depicting tumor volume of 168fARN WGD- or WGD+ tumors growing in Balb/c mice treated with isotype control or anti-CD8 antibodies starting on day two after tumor cell injection into the mammary fat pads. Data are represented as mean ± SEM, n = 8-10 tumors per condition from 5 mice per group, p-values calculated with Two-Way ANOVA-Tukey's multiple comparisons test.

(D) Scatter dot plot showing the relative fraction of $CD8^+$ T cells quantified by flow cytometry in 168fARN WGD- and WGD+ tumors treated with isotype control or anti-CD8 antibodies. Data are represented as mean ± SEM n =10 all conditions except n=6 for WGD+ aCD8 group. Kruskal-Wallis test.

(E) Heatmap depicting the unsupervised clustering of RNA-seq data on tumor samples from the indicated treatment groups based on differentially expressed genes identified between WGD- and WGD+ tumors in A/J mice in Figure 2L.

(F) Heatmap depicting the unsupervised clustering of enrichment score of 50 hallmark pathways on tumor samples from the indicated treatment groups.

(G,H) Scatter pots showing the Pearson correlation of Hallmark pathway signature enrichment alterations induced by αCD8 (H) and aPDL-1 (I) between WGD- and WGD+ tumors.

(I) Box plot showing immune scores inferred from RNA-seq using ESTIMATE in tumors from the indicated treatment groups.

(J) Flow cytometry of $EpCAM^+CD45^-$ cells from TA3 WGD- and WGD+ tumors stained with Hoechst33258 to assess DNA content from the experiment of Fig. 3H.

(K) Box plots depicting the ploidy prediction and antigen presentation signatures in FUSCC TNBC samples divided WGD status. Mann Whitney U test was used for each comparison.

(L,N) Box plots illustrating the immune scores calculated by ESTIMATE in METABRIC, TCGA and FUSCC cohorts between WGD- and WGD+ samples with (N) or without (L) separation by median of tumor purities (i.e., tumor cell content) of each cohort. Mann Whitney U test was used for each comparison.

(M) Box plots illustrating the immune scores calculated by ESTIMATE in METABRIC TNBC sample divided by *TP53* and WGD status. Mann Whitney U test was used for each comparison.

(O) Box plots showing leukocyte counts in the TCGA cohort (Left) and $CD8^+$T cell to total T cell ratio from imaging mass cytometry quantification in the METABRIC cohort (Right). Samples were subdivided based on tumor purity. Low and high purity tumors were segregated by the median purity of all tumors. Mann Whitney U test was used for each comparison.

Box plots in panels I and K-O represent the median (center line) and interquartile range (box, 25th-75th percentiles). Whiskers extend to 1.5× the interquartile range. Error bars represent SEM (A,C,D).

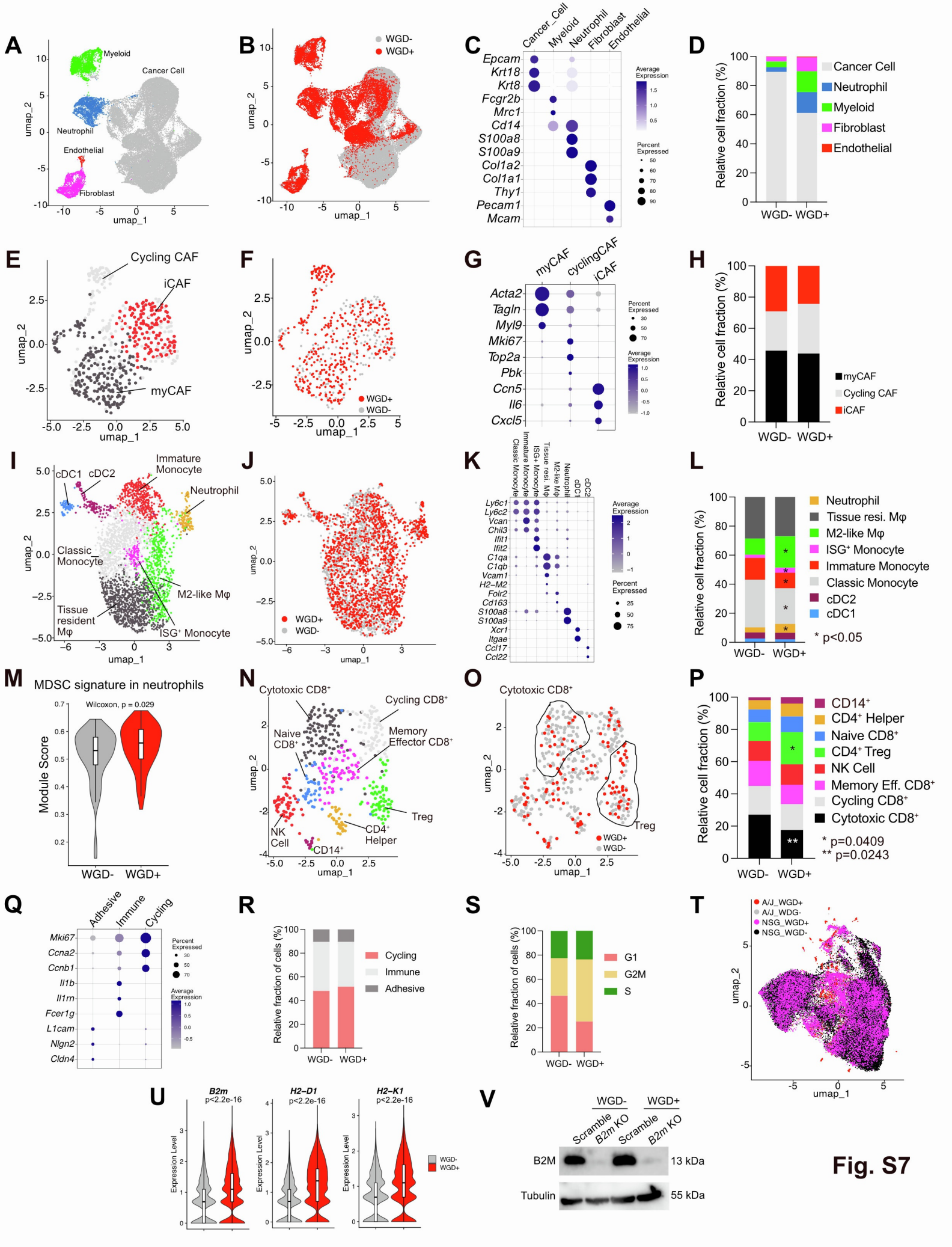
A
Myeloid
Cancer Cell
Neutrophil
Endothelial
Fibroblast
umap_1
umap_2
B
WGD-
WGD+
C
Cancer_Cell
Myeloid
Neutrophil
Fibroblast
Endothelial
Epcam
Krt18
Krt8
Fcgr2b
Mrc1
Cd14
S100a8
S100a9
Col1a2
Col1a1
Thy1
Pecam1
Mcam
Average Expression
Percent Expressed
D
Relative cell fraction (%)
Cancer Cell
Neutrophil
Myeloid
Fibroblast
Endothelial
WGD- WGD+
E
Cycling CAF
iCAF
myCAF
F
WGD+
WGD-
G
myCAF
cyclingCAF
iCAF
Acta2
Tagln
Myl9
Mki67
Top2a
Pbk
Ccn5
Il6
Cxcl5
H
myCAF
Cycling CAF
iCAF
I
cDC1
cDC2
Immature Monocyte
Neutrophil
Classic Monocyte
M2-like Mφ
Tissue resident Mφ
ISG⁺ Monocyte
J
K
Classic Monocyte
Immature Monocyte
ISG+ Monocyte
Tissue resi. Mφ
M2-like Mφ
Neutrophil
cDC1
cDC2
Ly6c1
Ly6c2
Vcan
Chil3
Ifit1
Ifit2
C1qa
C1qb
Vcam1
H2–M2
Folr2
Cd163
S100a8
S100a9
Xcr1
Itgae
Ccl17
Ccl22
L
Neutrophil
Tissue resi. Mφ
M2-like Mφ
ISG⁺ Monocyte
Immature Monocyte
Classic Monocyte
cDC2
cDC1
* p<0.05
M
MDSC signature in neutrophils
Wilcoxon, p = 0.029
Module Score
N
Cytotoxic CD8⁺
Cycling CD8⁺
Naive CD8⁺
Memory Effector CD8⁺
Treg
NK Cell
CD4⁺ Helper
CD14⁺
O
Cytotoxic CD8⁺
Treg
P
CD14⁺
CD4⁺ Helper
Naive CD8⁺
CD4⁺ Treg
NK Cell
Memory Eff. CD8⁺
Cycling CD8⁺
Cytotoxic CD8⁺
* p=0.0409
** p=0.0243
Q
Adhesive
Immune
Cycling
Mki67
Ccna2
Ccnb1
Il1b
Il1rn
Fcer1g
L1cam
Nlgn2
Cldn4
R
Relative fraction of cells (%)
Cycling
Immune
Adhesive
S
G1
G2M
S
T
A/J_WGD+
A/J_WDG-
NSG_WGD+
NSG_WGD-
U
B2m
p<2.2e-16
H2–D1
p<2.2e-16
H2–K1
p<2.2e-16
Expression Level
V
WGD-
WGD+
Scramble
B2m KO
B2M
13 kDa
Tubulin
55 kDa

Fig. S7

Figure S7. scRNA-seq analysis of WGD- and WGD+ tumors. Related to Figure 4.

(A,B) UMAP of TA3 WGD- and WGD+ tumor scRNA-seq data colored by cell cluster (A) and genotype (B) in NSG mice at day 12.

(C) Dot plot illustrating the marker genes enrichment in the indicated cell subtypes in panel A.

(D) Stacked bar plot showing the percentage of each cell subtypes normalized to total cells in WGD- and WGD+ tumors TA3 model in NSG mice at day 12.

(E,F) UMAP of fibroblast cell subclustering of WGD- and WGD+ tumors from A/J mice colored by cell subtype (E) and genotype (F).

(G) Dot plot illustrating the marker genes enrichment in the indicated cell subtypes in E.

(H) Stacked bar plot showing the percentage of each fibroblast subtypes normalized to total cells in WGD- and WGD+ tumors.

(I,J) UMAP of myeloid cell subclustering of WGD- and WGD+ tumors from A/J mice colored by cell subtype (I) and genotype (J).

(K) Dot plot illustrating the marker genes enrichment in the indicated cell subtypes in panel I.

(L), Stacked bar plot showing the percentage of each myeloid cell types normalized to total cells in WGD- and WGD+ tumors. Asterisks mark significant differences, p-values are indicated, Fisher's exact test.

(M) Violin plot showing MDSC signature module score enrichment in neutrophil populations. Mann Whiteny U test.

(N, O) UMAP of lymphocyte subclustering in WGD- and WGD+ tumor scRNA-seq data colored by cell subtypes (N) and genotype (O).

(P) Stacked bar plot showing the percentage of each lymphocyte subtypes normalized to total lymphocyte in WGD- and WGD+ tumors. Asterisks mark significant differences, p-values are indicated. Fisher's exact test.

(Q) Dot plot illustrating the marker genes enrichment in the indicated cancer cell subclusters in Figure 4H.

(R,S) Stacked bar plots showing the distribution of cluster subtypes (R) and inferred cell cycle phase (S) of cancer cells in WGD- and WGD+ tumors.

(T) UMAP plots showing the clustering of cancer cells of WGD- and WGD+ tumors merged from A/J and NSG mice.

(U) Violin plot showing the expression of the indicated MHC-I genes in TA3 WGD- and WGD+ cells in vitro. Mann Whiteny U test was used.

(V) Immunoblot for B2M in TA3 WGD- and WGD+ cells expressing a scramble or a *B2m* sgRNA. Tubulin was used as loading control.

Box plots in panels M and U represent the median (center line) and interquartile range (box, 25th-75th percentiles). Whiskers extend to 1.5× the interquartile range.

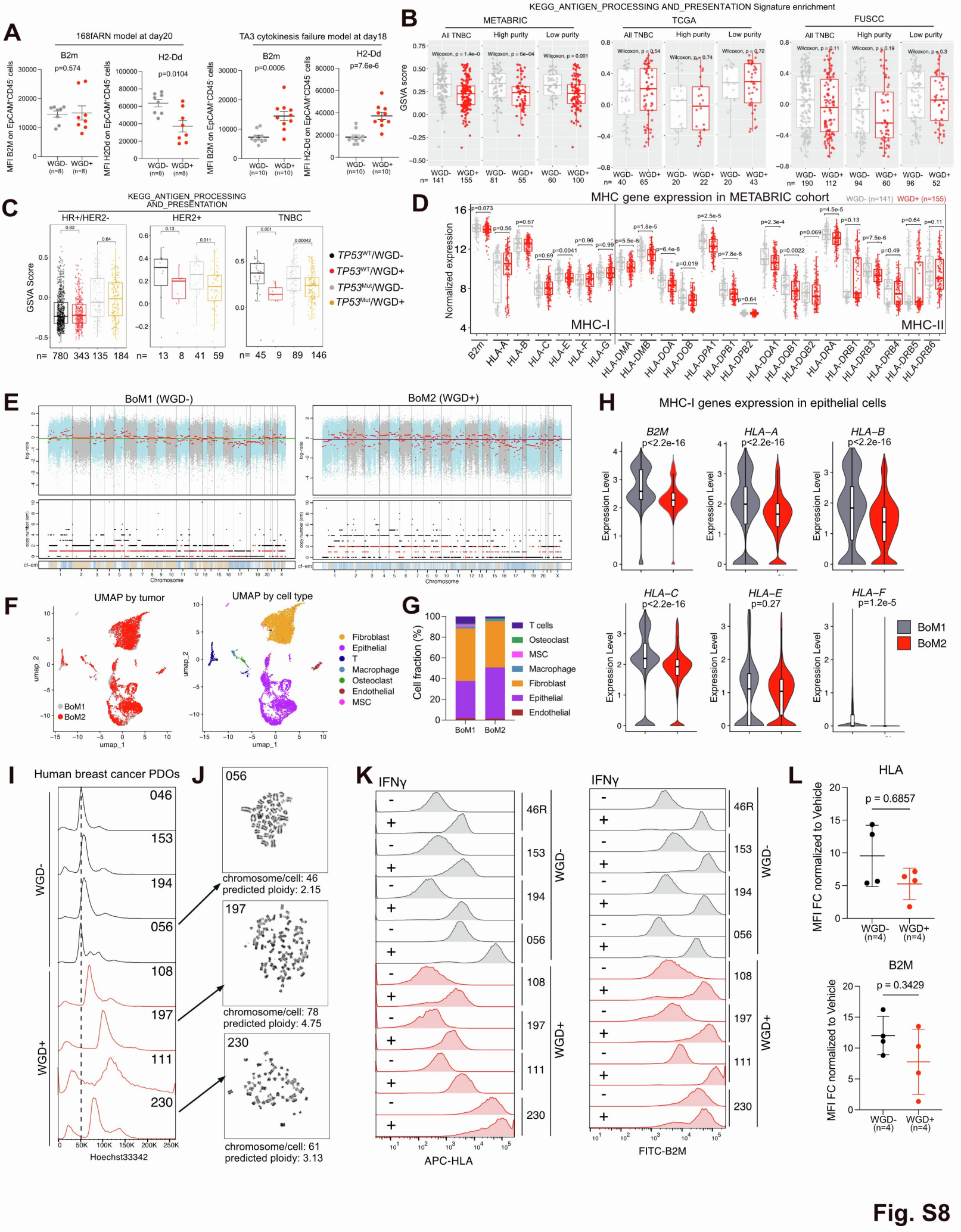
A
168fARN model at day20
TA3 cytokinesis failure model at day18
B2m
H2-Dd
p=0.574
p=0.0104
p=0.0005
p=7.6e-6
MFI B2M on EpCAM+CD45- cells
MFI H2Dd on EpCAM+CD45- cells
MFI H2-Dd on EpCAM+CD45- cells
WGD- (n=8)
WGD+ (n=8)
WGD- (n=10)
WGD+ (n=10)
B
KEGG_ANTIGEN_PROCESSING AND_PRESENTATION Signature enrichment
METABRIC
TCGA
FUSCC
All TNBC
High purity
Low purity
GSVA score
n= 141 155 81 55 60 100
n= 40 65 20 22 20 43
n= 190 112 94 60 96 52
C
KEGG_ANTIGEN_PROCESSING AND_PRESENTATION
HR+/HER2-
HER2+
TNBC
GSVA Score
n= 780 343 135 184
n= 13 8 41 59
n= 45 9 89 146
TP53WT/WGD-
TP53WT/WGD+
TP53Mut/WGD-
TP53Mut/WGD+
D
MHC gene expression in METABRIC cohort
WGD- (n=141)
WGD+ (n=155)
Normalized expression
MHC-I
MHC-II
B2m
HLA-A
HLA-B
HLA-C
HLA-E
HLA-F
HLA-G
HLA-DMA
HLA-DMB
HLA-DOA
HLA-DOB
HLA-DPA1
HLA-DPB1
HLA-DPB2
HLA-DQA1
HLA-DQB1
HLA-DQB2
HLA-DRA
HLA-DRB1
HLA-DRB3
HLA-DRB4
HLA-DRB5
HLA-DRB6
E
BoM1 (WGD-)
BoM2 (WGD+)
log2-ratio
copy number (em)
cf-em
Chromosome
F
UMAP by tumor
UMAP by cell type
BoM1
BoM2
Fibroblast
Epithelial
T
Macrophage
Osteoclast
Endothelial
MSC
umap_1
umap_2
G
Cell fraction (%)
T cells
Osteoclast
MSC
Macrophage
Fibroblast
Epithelial
Endothelial
H
MHC-I genes expression in epithelial cells
B2M
HLA–A
HLA–B
HLA–C
HLA–E
HLA–F
p<2.2e-16
p=0.27
p=1.2e-5
Expression Level
I
Human breast cancer PDOs
WGD-
WGD+
046
153
194
056
108
197
111
230
Hoechst33342
J
chromosome/cell: 46
predicted ploidy: 2.15
chromosome/cell: 78
predicted ploidy: 4.75
chromosome/cell: 61
predicted ploidy: 3.13
K
IFNγ
46R
APC-HLA
FITC-B2M
L
HLA
B2M
p = 0.6857
p = 0.3429
MFI FC normalized to Vehicle
WGD- (n=4)
WGD+ (n=4)

Fig. S8

Figure S8. Clinical sample validation. Related to Figure 4.

(A) Scatter plot showing B2m and H2-Dd expression in $EpCAM^{+}/CD45^{-}$ cells in the indicated models and time points.

(B) Box plots depict the antigen presentation enrichment score calculated by GSVA in METABRIC, TCGA and FUSCC cohorts between WGD- and WGD+ TNBC samples with or without separation by median of tumor purities of each cohort.

(C) Box plots illustrating the antigen presentation pathway enrichment score in METABRIC TNBC sample divided by *TP53* mutation and WGD status.

(D) Box plots showing the expression of the indicated MHC-I genes in WGD- and WGD+ TNBC in the METABRIC cohort.

(E) FACET copy number calling from two bone metastasis samples from the same patient.

(F) UMAP showing clustering of all cells from two bone metastasis samples from the same patient by cell type (right) and sample (left).

(G) Stacked bar plot showing the percentage of each cell type normalized to total cells in WGD- and WGD+ bone metastasis samples.

(H) Violin plot showing expression of MHC-I genes in cancer cell populations from WGD- and WGD+ bone metastasis samples.

(I) Flow cytometry of four WGD- and four WGD+ breast cancer PDOs stained with Hoechst33342 to assess DNA content.

(J) Representative images of metaphase karyotypes from three indicated PDOs. Quantified chromosome number and predicted ploidy are shown.

(K) Flow cytometry for B2M and HLA in four WGD- and four WGD+ breast cancer PDOs with or without IFNγ stimulation for 72 hrs.

(L) Dot plot showing IFNγ-induced fold change of B2M and HLA between WGD- and WGD+ organoids. Mann Whiteny U test was used.

Box plots in panels B-D and H represent the median (center line) and interquartile range (box, 25th-75th percentiles). Whiskers extend to 1.5× the interquartile range. Mann Whitney U test (A-D, H). Error bars represent SEM (A) or SD (L).

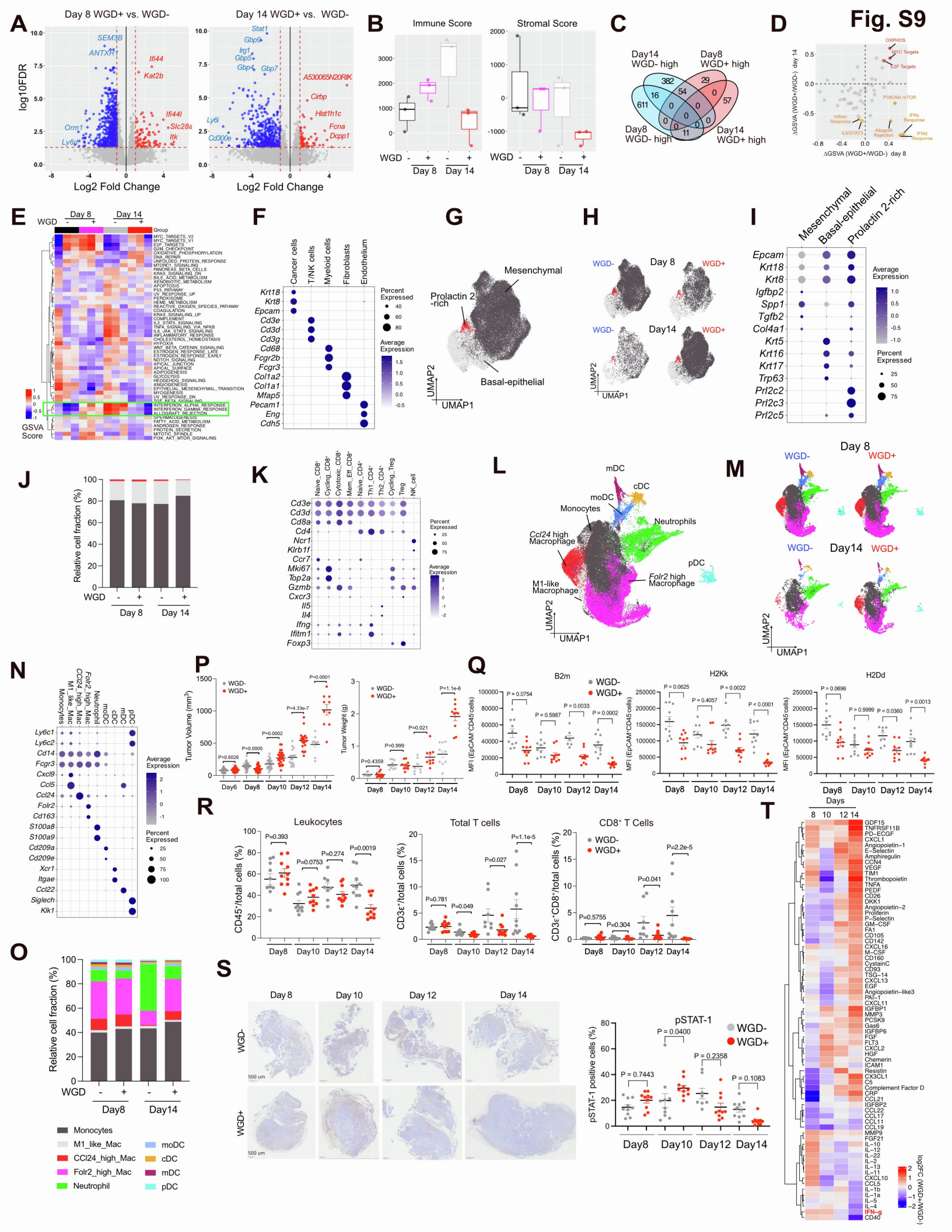
Fig. S9
A
Day 8 WGD+ vs. WGD-
Day 14 WGD+ vs. WGD-
log10FDR
Log2 Fold Change
SEM3B
ANTXR1
Ifi44
Kat2b
Ifi44l
Slc28a
Itk
Orm1
Ly6c
Stat1
Gbp9
Irg1
Gbp5
Gbp4
Gbp7
A530065N20RIK
Cirbp
Hist1h1c
Fcna
Dcpp1
Ly6i
Cd300e
B
Immune Score
Stromal Score
WGD
Day 8
Day 14
C
Day14 WGD- high
Day8 WGD+ high
Day8 WGD- high
Day14 WGD+ high
D
OXPHOS
MYC Targets
E2F Targets
PI3K/Akt mTOR
Inflam Response
IFNγ Response
IL6/STAT3
Allograft Rejection
IFNα Response
ΔGSVA (WGD+/WGD-) day 14
ΔGSVA (WGD+/WGD-) day 8
E
GSVA Score
INTERFERON_ALPHA_RESPONSE
INTERFERON_GAMMA_RESPONSE
ALLOGRAFT_REJECTION
F
Cancer cells
T/NK cells
Myeloid cells
Fibroblasts
Endothelium
Krt18
Krt8
Epcam
Cd3e
Cd3d
Cd3g
Cd68
Fcgr2b
Fcgr3
Col1a2
Col1a1
Mfap5
Pecam1
Eng
Cdh5
Percent Expressed
Average Expression
G
Mesenchymal
Prolactin 2 -rich
Basal-epithelial
UMAP1
UMAP2
H
WGD-
WGD+
Day 8
Day14
I
Mesenchymal
Basal-epithelial
Prolactin 2-rich
Epcam
Krt18
Krt8
Igfbp2
Spp1
Tgfb2
Col4a1
Krt5
Krt16
Krt17
Trp63
Prl2c2
Prl2c3
Prl2c5
Average Expression
Percent Expressed
J
Relative cell fraction (%)
WGD
Day 8
Day 14
K
Naive_CD8+
Cycling_CD8+
Cytotoxic_CD8+
Mem_Eff_CD8+
Naive_CD4+
Th1_CD4+
Th2_CD4+
Cycling_Treg
Treg
NK_cell
Cd3e
Cd3d
Cd8a
Cd4
Ncr1
Klrb1f
Ccr7
Mki67
Top2a
Gzmb
Cxcr3
Il5
Il4
Ifng
Ifitm1
Foxp3
L
mDC
cDC
moDC
Monocytes
Neutrophils
Ccl24 high Macrophage
pDC
Folr2 high Macrophage
M1-like Macrophage
UMAP1
UMAP2
M
Day 8
Day14
WGD-
WGD+
N
Monocytes
M1_like_Mac
Ccl24_high_Mac
Folr2_high_Mac
Neutrophil
moDC
cDC
mDC
pDC
Ly6c1
Ly6c2
Cd14
Fcgr3
Cxcl9
Ccl5
Ccl24
Folr2
Cd163
S100a8
S100a9
Cd209a
Cd209e
Xcr1
Itgae
Ccl22
Siglech
Klk1
Average Expression
Percent Expressed
P
Tumor Volume (mm³)
Tumor Weight (g)
Day6
Day8
Day10
Day12
Day14
Q
B2m
H2Kk
H2Dd
MFI (EpCAM+CD45-cells)
R
Leukocytes
Total T cells
CD8+ T Cells
CD45+/total cells (%)
CD3ε+/total cells (%)
CD3ε+CD8+/total cells (%)
S
Day 8
Day 10
Day 12
Day 14
500 um
pSTAT-1
pSTAT-1 positive cells (%)
T
Days
GDF15
TNFRSF11B
PD-ECGF
CXCL1
Angiopoietin-1
E-Selectin
Amphiregulin
CCN4
VEGF
TIM1
Thrombopoietin
TNFA
PEDF
CD26
DKK1
Angiopoietin-2
Proliferin
P-Selectin
GM-CSF
FA1
CD105
CD142
CXCL16
M-CSF
CD160
CystainC
CD93
TSG-14
CXCL13
EGF
Angiopoietin-like3
PAI-1
CXCL11
IGFBP1
MMP3
PCSK9
Gas6
IGFBP6
FGF
FLT3
CXCL2
HGF
Chemerin
ICAM1
Resistin
CX3CL1
C5
Complement Factor D
CRP
CCL21
IGFBP2
COL22
CCL17
CCL11
CCL19
MMP9
FGF21
IL-10
IL-12
IL-22
IL-2
IL-13
IL-11
CXCL10
CCL5
IL-1b
IL-1a
IL-5
IL-4
IFN-g
CD40
log2FC (WGD+/WGD-)

Figure S9. Time course experiment. Related to Figure 5.

(A) Volcano plots showing comparison of RNA-seq data from bulk WGD- and WGD+ tumors collected at day 8 and day 14. Significant DEGs (FDR<0.05, |log2FC|>1) are marked by blue (low in WGD+) and red (high in WGD+) colors. Top DEGs are indicated.

(B) Box plot showing immune and stromal scores inferred from RNA-seq data using ESTIMATE in the indicated tumor groups (n=3 tumors/condition).

(C) Venn diagram showing the overlap among four set of DEGs with indicated groups.

(D) Scatter plot showing the Pearson correlation of Hallmark pathway signature enrichment differences between WGD- and WGD+ tumors at day 8 and day 14.

(E) Heatmap depicting the unsupervised clustering of samples based on the enrichment score of 50 hallmark pathways.

(F) Dot plot illustrating the marker genes enrichment in the indicated cell subtypes in Figure 5D.

(G,H,L,M) UMAP of cancer cell (G) and myeloid cells (L) subclustering of WGD- and WGD+ tumors from A/J mice at day 8 and day 14 colored by cell type (G,L) and split by group (H,M).

(I,N) Dot plot illustrating the marker genes enrichment in the indicated cell subtypes in panels G and L, respectively.

(J,O) Stacked bar plots showing the percentage of each cancer cell (J) and myeloid cell (O) subtypes normalized to total cells in the indicated groups.

(K) Dot plot illustrating the marker genes enrichment in the indicated lymphocyte subtypes in Figure 5I.

(P) Scatter plots showing individual tumor volume (left) and weight (right) of TA3 WGD- and WGD+ tumors in A/J mice collected at the indicated time points. Kruskal-Wallis test, n = 8 or 10 per group.

(Q,R) Plots showing the expression of the indicated MHC-I proteins detected by flow cytometry on $EpCAM^{+}CD45^{-}$ cells (Q) and the frequencies of the indicated immune cell populations (R). Data are represented as mean ± SEM, n = 8 or 10 per group. Kruskal-Wallis test.

(S) Representative images and quantification of pSTAT-1 immunohistochemistry staining on TA3 WGD- and WGD+ tumors. Kruskal-Wallis test, n = 8 or 10 per group. Scale bar, 500 μm.

(T) Heatmap depicting the log2 fold change of each indicated cytokine in WGD+ tumors normalized to WGD- tumors at the indicated time points.

Box plots in B represent the median (center line) and interquartile range (box, 25th-75th percentiles). Whiskers extend to 1.5× the interquartile range.

Error bars represent SEM (P-S).

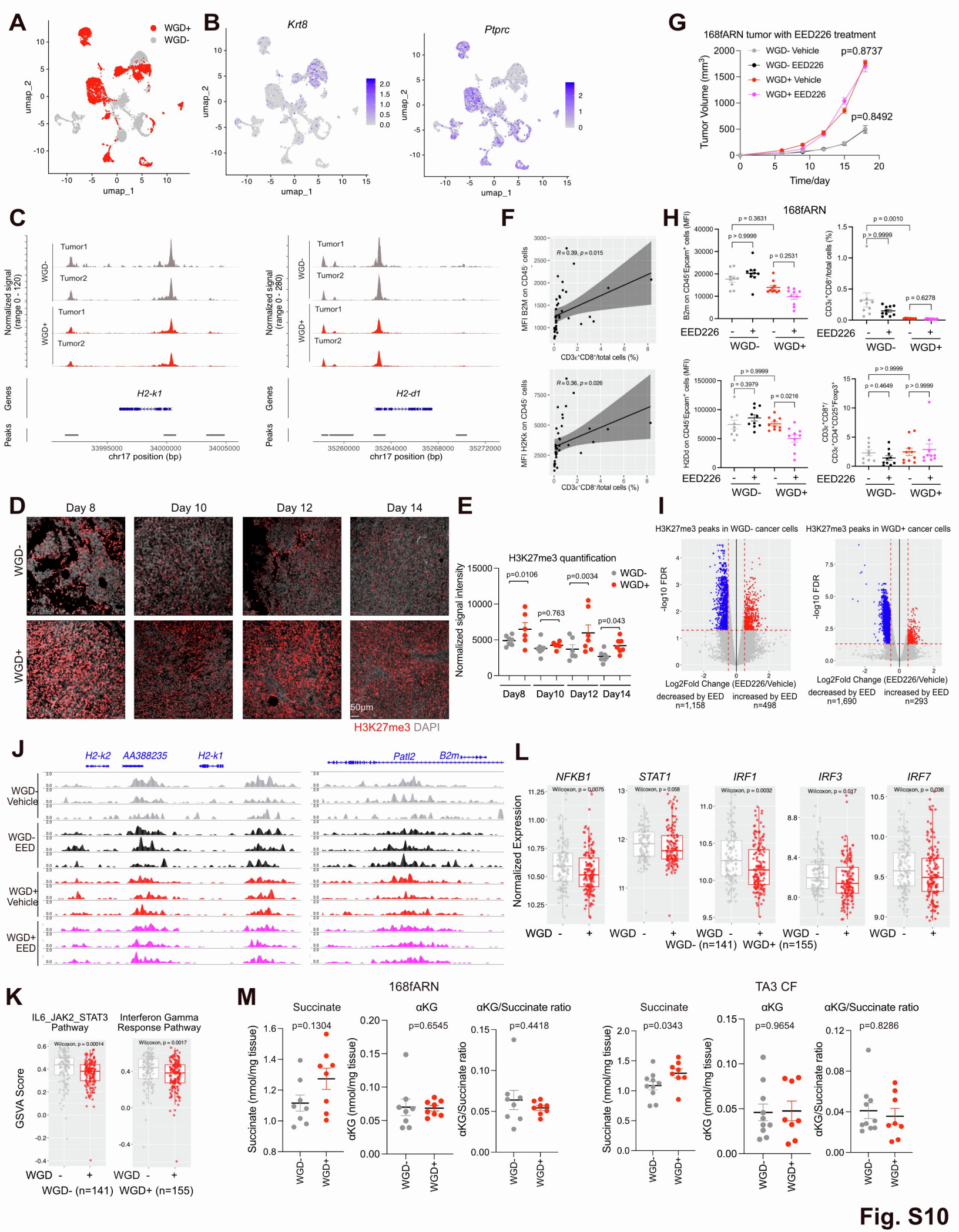
A
WGD+
WGD-
umap_1
umap_2
B
Krt8
Ptprc
G
168fARN tumor with EED226 treatment
WGD- Vehicle
WGD- EED226
WGD+ Vehicle
WGD+ EED226
p=0.8737
p=0.8492
Tumor Volume (mm3)
Time/day
C
Normalized signal (range 0 - 120)
Normalized signal (range 0 - 280)
Tumor1
Tumor2
Genes
Peaks
H2-k1
H2-d1
chr17 position (bp)
F
MFI B2M on CD45- cells
MFI H2Kk on CD45- cells
R = 0.39, p = 0.015
R = 0.36, p = 0.026
CD3ε+CD8+/total cells (%)
H
168fARN
B2m on CD45-Epcam+ cells (MFI)
H2Dd on CD45-Epcam+ cells (MFI)
CD3ε+CD8+/total cells (%)
CD3ε+CD8+/CD3ε+CD4+CD25+Foxp3+
EED226
WGD-
WGD+
D
Day 8
Day 10
Day 12
Day 14
WGD-
WGD+
50μm
H3K27me3 DAPI
E
H3K27me3 quantification
Normalized signal intensity
p=0.0106
p=0.763
p=0.0034
p=0.043
Day8
Day10
Day12
Day14
I
H3K27me3 peaks in WGD- cancer cells
H3K27me3 peaks in WGD+ cancer cells
-log10 FDR
Log2Fold Change (EED226/Vehicle)
decreased by EED n=1,158
increased by EED n=498
decreased by EED n=1,690
increased by EED n=293
J
H2-k2
AA388235
H2-k1
Patl2
B2m
WGD- Vehicle
WGD- EED
WGD+ Vehicle
WGD+ EED
L
NFKB1
STAT1
IRF1
IRF3
IRF7
Normalized Expression
WGD- (n=141)
WGD+ (n=155)
K
IL6_JAK2_STAT3 Pathway
Interferon Gamma Response Pathway
GSVA Score
M
168fARN
TA3 CF
Succinate
αKG
αKG/Succinate ratio
Succinate (nmol/mg tissue)
αKG (nmol/mg tissue)
p=0.1304
p=0.6545
p=0.4418
p=0.0343
p=0.9654
p=0.8286

Fig. S10

Figure S10. Epigenetic patterns and MHC-I expression. Related to Figures 6 and 7.

(A) UMAP of scATAC-seq of WGD- and WGD+ tumors in A/J mice at day 14 colored by genotypes.

(B) UMAP showing the inferred gene activity scores of *Krt8* and *Ptprc*.

(C) Genomic track view of average ATAC-seq signal in WGD- and WGD+ TA3 cancer cells based on scATAC-seq at *H2-d1* and *H2-k1* genomic loci in each individual tumor. Signal intensity was adjusted using the same scale for each group.

(D,E) Representative images (D) and quantification (E) of H3K27me3 immunofluorescence staining on TA3 WGD- and WGD+ tumors from experiment depicted in Figure S9P-T. Kruskal-Wallis test, n = 8 or 10 per group. Scale bar, 50 μm

(F) Scatter plot showing the Pearson correlation of $CD8^+$ T cell fraction with B2M or H2-Kk expression on $CD45^-$ cells from each tumor in Fig. 7A-E.

(G) Line plot showing tumor volume of 168fARN WGD- or WGD+ cells in Balb/c mice treated with vehicle or EED226. n = 10 tumors per condition from 5 mice per group. Two-ways ANOVA analysis was used in each pair of comparison.

(H) Graphs depicting B2m and H-2Kk mean expression on $CD45^-Epcam^+$ cells and frequency of $CD3^+CD8^+$ cells quantified by flow cytometry. Kruskal-Wallis test, n = 10 per condition.

(I) Volcano plot showing differential H3K27me3 peaks (FDR<0.05, |log2FC|>0.5) induced by EED226 treatment derived from CUT&RUN in WGD- (top) and WGD+ (bottom) sorted $EpCAM^+$ cancer cells.

(J) Genomic track view of H3K27me3 signal at *H2-K1* and *B2m* genomic loci.

(K,L) Box plots showing IL6_JAK2_STAT3 and interferon gamma response pathway enrichment scores (K) and interferon response regulator gene expression (L) in deconvoluted tumor components between WGD- and WGD+ TNBC tumors in the METABRIC cohort. Mann Whitney U test was used.

(M) Dot plots showing succinate and alpha ketoglutarate (αKG) levels, and their ratio measured from tumor lysate of 168fARN or TA3 cytokinesis failure WGD- and WGD+ tumors collected at day 20 and 18 respectively. Mann-Witney U test, n=8 or 10 per group.

Box plots in panels L and K represent the median (center line) and interquartile range (box, 25th-75th percentiles). Whiskers extend to 1.5× the interquartile range. Error bars represent SEM (G,H,E,M).